Fall 1-31-1997

Potential effects of pneumatic fracturing on existing structures and utilities

Michael C. Canino
New Jersey Institute of Technology

ABSTRACT

POTENTIAL EFFECTS OF PNEUMATIC FRACTURING ON EXISTING STRUCTURES AND UTILITIES

by
Michael C. Canino

This thesis develops a mathematical design model for predicting ground deformations resulting from pneumatic fracturing. Pneumatic fracturing is a patented process developed for the purpose of enhancing the *in situ* treatment and removal of hazardous contaminants from geologic formations. During pneumatic injections, measurable ground deformations are experienced both during and after the process. Safe application of pneumatic fracturing to contaminated plumes occurring beneath existing structures and utilities requires that the elastic deformation behavior of the geologic formation and overlying structures be quantified.

Data from five pneumatic fracturing sites were regressed to establish the characteristic polynomial describing the curvature of ground deformation. A model was then developed using theories of elastic plate bending and ground deformations by igneous laccolith intrusions. The deformed geologic formation is modeled as a circular plate subjected to a linear tapering pressure distribution. Comparison of the model results with actual field data displayed reasonable agreement.

An instrumented field test was performed beneath an actual contaminated industrial facility to obtain data on the dynamic response of the structure. Based on the field test results, as well as experience from over 40 additional pneumatic fracturing sites, a systematic design guideline was developed. The guideline classifies structures as either flexible or rigid, and then categorizes them into one of three characteristic design cases.

POTENTIAL EFFECTS OF PNEUMATIC FRACTURING ON EXISTING STRUCTURES AND UTILITIES

by
Michael C. Canino

A Thesis
Submitted to the Faculty of
New Jersey Institute of Technology
in Partial Fulfillment of the Requirements for the Degree of
Master of Science in Civil Engineering

Department of Civil and Environmental Engineering

January 1997

APPROVAL PAGE

POTENTIAL EFFECTS OF PNEUMATIC FRACTURING ON EXISTING STRUCTURES AND UTILITIES

Michael C. Canino

Dr. John R. Schuring, Thesis Advisor — Date
Professor of Civil and Environmental Engineering, NJIT

Edward G. Dauenheimer, Committee Member — Date
Professor of Civil and Environmental Engineering, NJIT

Dr. Dorairaja Raghu, Committee Member — Date
Professor of Civil and Environmental Engineering, NJIT

BIOGRAPHICAL SKETCH

Author: Michael C. Canino

Degree: Master of Science in Civil Engineering

Undergraduate and Graduate Education:

- Master of Science in Civil Engineering
  New Jersey Institute of Technology
  Newark, New Jersey, 1997

- Bachelor of Science in Civil Engineering
  Drexel University
  Philadelphia, PA 1992

- Bachelor of Science in Architectural Engineering
  Drexel University
  Philadelphia, PA 1992

Major: Civil Engineering

Publications:

Schuring, J.R., Canino, M.C., Boland, T.M., and Nelson, I., 1996. "Final Report, Site-45D, Investigation of the Effects of Pneumatic Fracturing on Structures and Utilities," prepared for the Hazardous Substance Management Research Center at the New Jersey Institute of Technology, Newark, NJ. A National Science Foundation Industry/University Cooperative Research Center.

This thesis is dedicated to my parents,
John and Elizabeth Canino, and to my love Andréa,
for their love, support, and encouragement.

ACKNOWLEDGMENT

I wish to express my most sincere appreciation to my advisor, Dr. John R. Schuring, Jr. Throughout the writing of this thesis he has provided me with inspiration, encouragement, guidance, and most of all, his friendship. His guidance and persistence in reviewing this thesis throughout its development have significantly increased the quality of my technical writing, analytical, and organizational skills.

I would like to thank Professor Edward G. Dauenheimer and Dr. Dorairaja Raghu for serving as my committee and providing useful suggestions for the thesis development.

I would like to thank Tom Boland, Joe DiBernardo, James Cerkanowicz and Suresh Puppala, and Ivan Nelson for their contributions in conducting the field test, surveying the test structure, reducing ground deformation data, and performing a computer frame analysis, respectively. Their efforts have helped significantly in the overall development of this thesis. I also wish to acknowledge other pneumatic fracturing friends and colleagues, Hugo Fernandez, Heather Hall, Deborah Schnell, and Brian Sielski.

I would like to acknowledge Tom Imholte for his initial Masters Project Report which provided a review and compilation of ground deformation data resulting from pneumatic fracturing, it was a great starting point for the development of this thesis.

In addition, I wish to thank the Hazardous Substance Management Research Center, Accutech Remedial Systems, Inc., and the Civil and Environmental Engineering Department of the New Jersey Institute of Technology which made this research possible.

Finally, I wish to thank my love Andréa, my family, and my close friends who supported me throughout the writing of this thesis.

TABLE OF CONTENTS

TABLE OF CONTENTS
(Continued)

TABLE OF CONTENTS
(Continued)

Chapter **Page**

LIST OF TABLES

LIST OF TABLES

Table **Page**

LIST OF FIGURES

LIST OF FIGURES
(Continued)

LIST OF FIGURES
(Continued)

LIST OF FIGURES
(Continued)

LIST OF SYMBOLS

A	=	area (L^2)
A	=	constant for Equation 3.5
A_c	=	ground deformation model equation coefficient
$A_{c(cal.)}$	=	calculated ground deformation model equation coefficient
A_L	=	base area of a laccolith (L^2)
A_x	=	cross-sectional steel area (L^2)
B	=	elastic modulus (= $E/(1-\nu^2)$) (F/L^2)
B	=	constant for Equation 3.5
B_F	=	base width of a foundation (L)
B_C	=	width of a utility conduit (L)
B_c	=	ground deformation model equation coefficient
B_T	=	width of a tunnel opening (L)
B_w	=	width of a wall (L)
a	=	short axis of an ellipse (L)
a	=	depth exponent to account for non-linearity with depth
b	=	long axis of an ellipse (L)
b_d	=	bearing distance (L)
b_f	=	actual fracture aperture (L)
C	=	circumference (L)
C_c	=	ground deformation model equation coefficient
CF	=	calibrated conversion factor for a LVDT

LIST OF SYMBOLS
(Continued)

c	=	cohesion of the overburden material (F/L^2)
D	=	flexural rigidity ($F \cdot L$)
D_c	=	ground deformation model equation coefficient
D_e	=	effective flexural rigidity of multiple layers of overburden ($F \cdot L$)
d	=	diameter of a laccolith (L)
E	=	modulus of elasticity (F/L^2)
E_i	=	modulus of elasticity of an individual layer of overburden (F/L^2)
$E_{L\text{-}C}$	=	modulus of elasticity for a circular shaped surface subjected to a linear-tapering pressure distribution (F/L^2)
E_G	=	modulus of elasticity of a geologic formation (F/L^2)
E_S	=	modulus of elasticity of a structure (F/L^2)
$E_{U\text{-}A}$	=	modulus of elasticity for an anticlinal shaped surface subjected to a uniform pressure distribution (F/L^2)
e_1, e_2	=	end eccentricities
F_c	=	ground deformation model equation coefficient
F_f	=	faulting force (F)
F_m	=	force due to the self-weight of the magma (F)
F_o	=	force due to the overburden above a forming laccolith (F)
F_{rem}	=	uplift force remaining to overcome the resisting force due to cohesion (F)
F_{up}	=	uplift force of magma forming a laccolith (F)
F_w	=	width of a laccolith feeder (L)

LIST OF SYMBOLS
(Continued)

G	=	modulus of rigidity (= $E/[2\cdot(1+\nu)]$) (F/L^2)
H_B	=	building height (L)
H_L	=	height of a laccolith (L)
H_w	=	wall height (L)
h_C	=	overburden thickness (L)
h_L	=	projected laccolith height (= laccolith thickness) (L)
I	=	moment of inertia (L^4)
I_z	=	moment of inertia in the z-direction (L^4)
k	=	constant for Equation 3.7
L	=	lateral extent of a laccolith (L)
L_I	=	distance between adjacent columns that settle different amounts, or between any two points that settle differently (L)
L_w	=	wall length (L)
L_B	=	span length of a beam (L)
M_{max}	=	maximum bending moment ($F\cdot L$)
M_s	=	measured voltage increase in steps for a LVDT (volts)
n	=	number of free sliding layers of overburden
P	=	assumed original design load (F)
P_{total}	=	total assumed original design load (F)
P_V	=	vertical load (F)
P_x	=	fracture maintenance pressure at a distance x from the injection point ($P_x = p_d\cdot[1-(|x|/R)]$) ($F/L^2$)

LIST OF SYMBOLS
(Continued)

=	magma pressure applied to the base of a laccolith (F/L^2)
=	magmatic driving pressure in excess of the gravitational load (F/L^2)
=	total injected magma pressure at the laccolith feeder (F/L^2)
=	load intensity (F/L^2)
=	fracture radius of influence (L)
=	resultant force (F)
=	radius (of a cylinder) (L)
=	initial, unstrained strain gage resistance (ohms)
=	strain gage resistance (ohms)
=	radius of a laccolith in plan (L)
=	resultant force (F)
=	lead wire resistance (ohms)
=	distance between two reference points for determining the relative deflection, Δ (L)
=	scale factor for a tiltmeter
=	step factor for a LVDT
=	total overburden thickness above laccolith intrusion (L)
=	effective thickness of multiple layers of overburden (L)
=	thickness of a single layer of overburden (L)
=	magma thickness above the laccolith base (L)
=	thickness of an individual layer of geologic overburden (L)

LIST OF SYMBOLS
(Continued)

V	=	resultant vertical force (F)
V_d	=	voltage difference measurement for a LVDT (volts)
V_I	=	input voltage (volts)
V_m	=	measured output voltage from a tiltmeter (volts)
V_O	=	output voltage (volts)
V_r	=	difference of the V_O/V_I ratios from the unstrained to strained states
w	=	displacement magnitude (L)
w_{act}	=	actual heave magnitude (L)
w_{max}	=	maximum displacement magnitude (L)
w_{mod}	=	heave calculated from the average equation (L)
X-	=	axis direction used for measurement of the tilt angle for a tiltmeter
x, y, z	=	the principle axis or the Cartesian coordinate system (L)
Y-	=	axis direction used for measurement of the tilt angle for a tiltmeter
z	=	thickness of the geologic overburden in the vertical direction (L)
α	=	angular strain, which is the change in θ
β	=	relative rotation or angular distortion, which is the angle between the overall tilt of a structure and the inclination of a specific portion of it
Δ	=	relative deflection, or settlement of a point relative to a straight line connecting two reference points at a distance, S, apart. Positive Δ indicates a situation known as sagging, and negative Δ indicates a situation known as hogging
Δ/L_I	=	deflection ratio, also known as sagging ratio or the hogging ratio

LIST OF SYMBOLS
(Continued)

ΔR_E	=	change in electronic resistance of a strain gage (ohms/ohms)
δ	=	total settlement, or absolute vertical movement of a particular foundation (L)
δ_{lim}	=	limiting values of settlement (L)
δ_{max}	=	maximum settlement (L)
δp	=	differential settlement (L)
δp_{30}	=	differential settlement when the bearing distance has decreased to 30% of its full value (L)
δ/L_l	=	angular distortion (L/L)
$\delta p/L_l$	=	Δ/L_l (L/L)
$\delta s/L_l$	=	difference of settlement (L/L)
ε	=	strain (L/L)
ε_s	=	elastic strain shortening (L/L)
ε_x, ε_y, ε_z	=	strain in respect to the principle axis (L/L)
$\gamma_{overburden}$	=	unit weight of the overburden material (F/L^3)
γ_{magma}	=	unit weight of the magma forming a laccolith (F/L^3)
γ_w	=	specific weight of water (F/L^3)
$\mu\varepsilon$	=	micro-strain ($10^{-6} \cdot$ L/L)
ν	=	Poisson's ratio
ν_i	=	Poisson's ratio for a specific layer "i"
ν_G	=	Poisson's ratio for a geologic formation
ν_S	=	Poisson's ratio for a structure

LIST OF SYMBOLS
(Continued)

π	=	Pi constant = 3.14159
θ	=	rotation, or the angle between the horizontal and any two foundations (or two points on a single foundation)
σ	=	stress (F/L^2)
σ_a	=	axial stress (F/L^2)
σ_b	=	stress due to bending (F/L^2)
σ_{beam}	=	estimated original design stress at a beam center (F/L^2)
σ_{total}	=	estimated original design stress at a strain gage location (F/L^2)
σ_x, σ_y, σ_z,	=	stress in respect to the principle axis (F/L^2)
σ'_h	=	horizontal effective stress (F/L^2)
σ'_v	=	vertical effective stress (F/L^2)
ω	=	tilt, or the rotation of the entire superstructure
∞	=	infinity

CHAPTER 1

GENERAL INTRODUCTION

1.1 Background

Over the last six or seven decades, improper disposal practices by the petroleum and chemical industries have led to serious damage to our subsurface environment. During the past 20 years, however, public awareness of these problems has increased significantly resulting in a national focus towards environmental protection. This focus has led many federal and state agencies to implement numerous regulations to improve waste practices, and to remediate sites which contain contaminated soil and groundwater.

The principal legislative action was the Resource Conservation and Recovery Act (RCRA) which became a law in 1976 and has since been updated seven times. In addition to RCRA, the Comprehensive Environmental Response, Compensation, and Liability Act (CERCLA) of 1980 was passed as a direct means of response and funding for solutions to problems at uncontrolled hazardous waste sites. Currently the U.S. Environmental Protection Agency (EPA) is investigating over 14,000 hazardous waste sites under CERCLA. Approximately 1,300 of these sites are on CERCLA's National Priority List (NPL) since they pose the greatest risk to human health and the environment.

As a result of limitations of the early remediation technologies to meet clean-up levels, as well as the excessive costs to the industry and the public, CERCLA was amended in 1986 by the Superfund Amendments and Reauthorization Act (SARA). This amendment redirected CERCLA funds for the development of new and innovative remediation technologies. SARA's main objectives were to accelerate site clean-up and reduce overall costs.

The innovative remediation technologies that have benefited most from the SARA Amendment are those which remove or treat the contaminants in place, which are termed "*in situ*" technologies. The basic advantages of the *in situ* technologies are: (1) they cause the least amount of site disturbance; and (2) they are usually the most economic alternative. Many contaminated sites contain numerous structures and utilities which are still in operation, so *in situ* remediation approaches which can be applied beneath active structures and utilities are highly desirable. These approaches avoid facility down-time and relocation, both of which are extremely costly to the site operation.

The effectiveness of *in situ* technologies at a particular site depends to a large extent on the nature of the contaminants and its geologic characteristics. The geologic factor which most often controls success or failure is hydraulic conductivity. Most available *in situ* technologies are limited to geologic formations with hydraulic conductivities greater than 10^{-4}cm/sec (Schuring, 1994).

To overcome the current hydraulic conductivity limitation, a research effort was started in 1987 at the Hazardous Substance Management Research Center (HSMRC) at the New Jersey Institute of Technology (NJIT) in Newark, New Jersey. This research effort has resulted in the development of a patented process called "pneumatic fracturing." The pneumatic fracturing process injects high pressure gas through a borehole into the vicinity of the contamination to increase the hydraulic conductivity of the geologic formation. This process results in the creation of a radial fracture network, thereby increasing the access to the contaminants which in turn increases the removal or treatment rates. To date, pneumatic fracturing has been successfully applied at over 40

contaminated sites to enhance the removal or treatment rates where difficult geologic conditions were encountered.

An important side effect of pneumatic fracturing is the ground deformation which occurs in the vicinity of the injection point. Ground deformations can exceed one inch and have the potential to damage overlying structures and utilities. Since a majority of industrial sites contain numerous surface structures, a thorough understanding of the interaction between the deforming geologic formation and these structures is essential if the technology is to mature and further gain commercial acceptance.

1.2 Objectives and Scope

The overall objective of this thesis is to develop a systematic design model for predicting geologic ground deformations resulting from pneumatic fracturing, and determining the potential effects on overlying structures and utilities. Experience from more than 40 pneumatically fractured sites shows that there is measurable ground surface deformations both during, and sometimes after, the fracturing event. In geotechnical and structural engineering, it is acknowledged that all structures and utilities can tolerate a certain amount of differential movement. The key then, is to control the pneumatic injections so that the differential movements remain below the tolerable level.

The specific objectives and scope of this research are as follows:

1. A thorough review of allowable differential movements for various classes of structures and utilities is undertaken. This allows establishment of tolerable differential movement criteria for structures and utilities typically found at contaminated facilities.

2. A mathematical model describing ground surface deformations of geologic strata is developed based on elastic plate bending theory and intrusive laccolith formation models. The model is calibrated using measured surface deformations from past pneumatic fracturing sites. In addition, the effect of superimposing various types of structures over the fractured geologic formation is investigated.

3. A field test is undertaken at an industrial building to measure the actual dynamic strain response of the structure to pneumatic injections. A structural stress-strain analysis is then performed to compare the stresses induced by the fracture injections with the original design stresses of the building.

4. Based on results of the model study and field test, three characteristic design cases for fracturing beneath structures are identified and developed. Guidelines for safely conducting pneumatic fracturing operations beneath or adjacent to structures and utilities are proposed.

The thesis begins with a review of the history and general methodology of pneumatic fracturing (Chapter 2). Next, elastic solutions for ground deformation will be examined as preparation for development of the pneumatic fracturing design model. In addition, differential movement criteria for structures and utilities found at industrial facilities is reviewed (Chapter 3). An analytical design model is then presented for predicting ground deformations to avoid damage beneath structures and utilities (Chapter 4). In addition, Chapter 4 will present comparative plots of observed surface deformation in the field with

that predicted by the analytical design model. The results of an actual field test of pneumatic fracturing conducted beneath an industrial structure are then reported in Chapter 5. This is followed by examination of three characteristic design cases for conducting pneumatic fracturing operations beneath structures (Chapter 6). The thesis concludes with a summary of key findings and recommendations for future research in this area (Chapter 7).

CHAPTER 2

PNEUMATIC FRACTURING BACKGROUND

The pneumatic fracturing process was originally developed to extend the applicability of available *in situ* remediation technologies to geologic formations with low hydraulic conductivities. Research on the process development began in late 1987 and eventually led to a patent by the Hazardous Substance Management Research Center (HSMRC) at the New Jersey Institute of Technology (NJIT) in July 1991 (US Patent No. 5,032,042). In addition to improving the effectiveness of *in situ* technologies, the pneumatic fracturing process has been expanded to deliver liquid, powder, microbiological, and granular supplements into geologic formations to help overcome the transport limitations that many *in situ* remediation technologies experience.

Since the original idea was conceived, the scope of the research has comprised numerous laboratory and field studies, as well as theoretical and computer model studies. As a result of the research efforts, pneumatic fracturing has proven to be a versatile process, and has progressed from the laboratory research stage to full commercial availability in the industrial sector.

A brief description of the pneumatic fracturing process is now provided (2.1), followed by a chronological history of the contributing research efforts (2.2).

2.1 Pneumatic Fracturing Process Description

The process methodology can best be described as it relates to the mechanics of pneumatic fracturing in soil and rock formations. This problem was studied in detail by King (1993)

who incorporated the knowledge gained from the previous five years of laboratory and field studies into a theoretical model. The basic mechanics concepts will now be presented briefly, and the reader is referred to King (1993) for a more comprehensive coverage of the subject.

The objective of a pneumatic injection is to create a radial fracture network emanating from the injection point at a discrete depth interval. This is depicted schematically in Figure 2.1. As illustrated, the process is performed in a conventional borehole. There are four primary components of the field apparatus necessary to perform an injection including: (1) a high flow (HQ) injector; (2) two inflatable packers; (3) a compressed gas source; and (4) a regulation system which is composed of precision switches, valves, and regulators. In addition, supplements can be introduced into the injected gas stream depending on the specific *in situ* technology which is being enhanced.

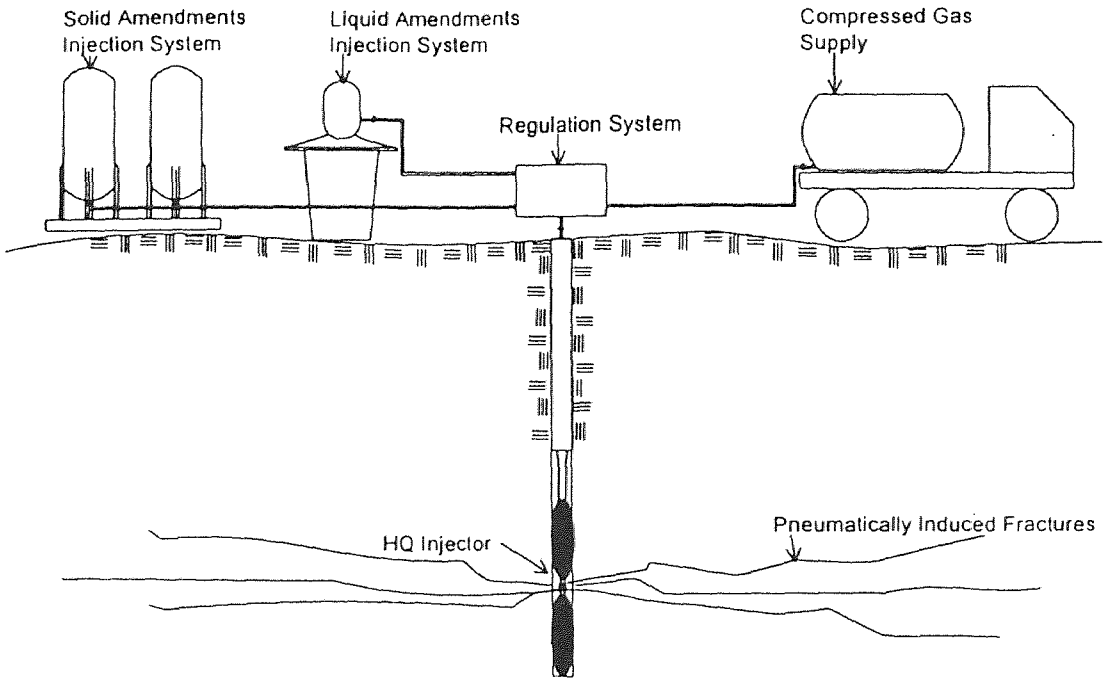

Figure 2.1 Pneumatic Fracturing Concept in Fine-Grained Formations (Puppala, 1996).

Pneumatic injections are accomplished using a four step cyclic procedure. First, the HQ injector is lowered into the borehole to a predetermined depth. Second, the flexible packers are inflated on either side of the HQ injector to seal off a discrete two foot interval. Third, pressure is applied from the compressed gas source into the discrete interval for a period of about 15 to 30 seconds to create the fracture network. Finally, the HQ injector is repositioned to the next depth interval and the procedure is repeated.

The success of an individual fracture injection is highly dependent on two parameters (Schuring, 1994). First, the compressed gas must be injected at a pressure which exceeds the combined forces of the natural cohesion of the formation, plus the *in situ* geologic stress occurring at the fracture depth. Second, the flow rate of the injected gas must exceed the natural geologic hydraulic conductivity so that sufficient back-pressure can be developed in the borehole to propagate the fracture into the formation. These parameters are predetermined based on the site geology and the fracture depth.

A general range for the critical input parameters to successfully propagate a fracture network in fine-grained formations are: (1) injection pressures of 300 to 500 lb/in^2; and (2) flow rates of 1,000 to 2,000 ft^3/min (Hall, 1995). During the pneumatic fracturing process, a fracture will propagate radially until the fluid loss rate equals the injection flow rate. This typically result in a radial fracture extent of 10 to 25 ft in fine-grained formations. The primary source of fluid loss is gas leak-off into the formation. Pressure losses also occur due to leak-off and friction losses. These factors are of particular interest in this study as they will have a profound influence on the pressure distribution applied at the discrete fracture interval, and consequently, the magnitude of the resulting ground surface deformation.

After a fracture network has successfully been created within a contaminant plume, another *in situ* remediation technology is typically applied. The pneumatically induced fracture network usually results in increased treatment rates and removal efficiencies. The primary reason for the enhancements is the induced fracture network allows more convective flow in the formation, thereby shortening the diffusive flow paths. The degree of enhancement will depend on the particular integrated *in situ* remediation technology, as well as the site specific contaminants, geologic conditions, and hydrogeologic conditions.

2.2 Studies Involving Pneumatic Fracturing

After the initial pneumatic fracturing process was conceived in late 1987, laboratory studies were initiated in 1988 to investigate basic process feasibility. Laboratory studies were conducted by Papanicolaou (1989) and Shah (1991) who initiated fractures by injecting compressed air into Plexiglas tanks containing soil mixtures with known contaminant concentrations. The removal efficiencies of the tanks containing fractured soil were then compared with unfractured soil tanks using a vapor extraction system. Results of the studies consistently showed that the contaminant removal rate from the fractured soil tanks was 170% to 360% greater than in the unfractured soil tanks.

The success of these initial studies led to a laboratory study investigating fluid flow characteristics and mass transport rates through discrete fractures of known dimensions by Ng (1991). The results confirmed that increased mass flow rates were developed as a result of the pneumatic fracturing process.

While the initial laboratory studies were being conducted, the pneumatic fracturing process began to move to full scale field tests in 1989. During the initial and then

subsequent early field demonstrations, the process was successfully applied at both "clean" and contaminated sites (Schuring et al., 1991; Schuring and Chan, 1992). Field observations and data from these early field demonstrations provided the necessary insight for improving the pneumatic fracturing process in the field. In addition, the success of these early field and laboratory studies provided the necessary basis for serious evaluation of the technology by the United States Environmental Protection Agency (USEPA).

The first major milestone in advancing the technology to gain commercial acceptance was the successful evaluation of the process in August 1992 by the USEPA. The evaluation was conducted under the Superfund Innovative Technology Evaluation (SITE) program at an industrial site contaminated with volatile organics in the vadose zone. Application of the pneumatic fracturing process led to increases in contaminant removal by more than 600% (EPA, 1993).

King (1993) completed a study that incorporated the knowledge gained from the previous five years of laboratory and field studies into a theoretical model. This study was the first to thoroughly describe and document the pneumatic fracturing process in soil and rock formations. In addition, theoretical models for predicting both fracture initiation and maintenance pressures were presented.

Successful laboratory studies, field studies, and theoretical modeling led to the second major milestone in advancing the pneumatic fracturing process: licensing Accutech Remedial Systems (ARS) of Keyport, New Jersey, as the first commercial vendor in 1993. Since that time, Accutech has applied the pneumatic fracturing technology at a number of industrial and governmental sites. A summary of the sites pneumatically fractured to date by both the NJIT and ARS are shown in Table 2.1.

Table 2.1 Summary of Sites Pneumatically Fractured to Date.

Research/Technology Transfer/Development Sites
Frelinghuysen Township, NJ
Richmond, VA
Hillsborough, NJ (USEPA SITE Demonstration)
Oklahoma City, OK
East Orange, NJ
Richland, WA
Flemington, NJ
Portsmouth, OH
Marcus Hook, PA (USEPA SITE Emerging Technology)
Industrial Pilot Sites
Roseland, NJ
East Newark, NJ
Santa Clara, CA
East Brunswick, NJ
Buffalo, NY
Huntsville, AL
Shreveport, LA
Highland Park, NJ
Coffeeville, KS
Kansas City, KS
Fort Wayne, IN
Production Sites
Hillsborough, NJ
Toronto, Canada
Tinker Air Force Base, OK
Oklahoma City, OK
Highland Park, NJ
Milwaukee, WI
Lancaster, PA
Kansas City, KS

After development of the basic pneumatic fracturing process was achieved, studies were expanded to integrate the process with *in situ* bioremediation. Fitzgerald (1993) was the first to perform a study on enhancing *in situ* bioremediation using pneumatic fracturing. A second study was conducted by Rahman (1994) in which nutrient pellets were injected using pneumatic fracturing to help enhance bioremediation activity. Rahman's study also investigated the use of pneumatic fracturing to inject surfactants into contaminated soils to increase desorption rates.

Studies were also conducted to integrate pneumatic fracturing with the innovative remediation technology of *in situ* vitrification. In this application pneumatic fracturing was used to inject highly conductive graphite/glass frit starter path material into a coarse-grained geologic formation to enable "bottom-up" melting (NJIT and ARS, 1994; McGonigal, 1995).

Theoretical model studies were continued as Nautiyal (1994) developed a model describing the flow of compressible fluids in discrete fractures. Ding (1995) developed a contaminant transport model using a dual porosity approach. Hall (1995) investigated the influence of volume changes on fracture behavior and longevity in geologic formations with low hydraulic conductivities.

Recent laboratory studies have included an investigation of integrating the pneumatic fracturing process with air sparging to enhance removal of volatile organic compounds in the saturated zone.

In August 1995, a field test was conducted to investigate the effects of the pneumatic fracturing process on an overlying structure (Schuring, et.al., 1996). This field test is reported in the present thesis and forms the basis for a model for describing ground

deformations resulting from pneumatic fracturing. In addition, design guidelines for fracturing beneath structures and utilities are presented.

Several other studies related to the pneumatic fracturing process are currently underway. Puppala (in progress) is developing a model to predict the propagation behavior of pneumatic fractures, as well as the transport of liquid and granular supplements within the fractures. A laboratory study which integrates the pneumatic fracturing process with ultrasound to enhance contaminant desorption is being conducted by Fernandez (in progress), and is scheduled for a field pilot test for sometime in 1997. A field pilot test involving injection of zero-valent iron to create a reactive cell in a contaminated ground water plume is also planned for 1997 (Schuring, Schnell, and Boland, in progress). Hall (in progress) is investigating the interrelationship between fracture geometry and volume changes for soils containing clay minerals, under a variety of boundary conditions.

In addition, Sielski (in progress) is continuing work started by Thoraval to compile a data base and to assemble the various analytical solutions into a comprehensive computer model. The model will be capable of screening potential sites, predicting conductivity enhancements, and establishing preliminary design parameters for pneumatic fracturing applications.

CHAPTER 3

LITERATURE REVIEW

3.1 Elastic Plate Bending Theory

A promising approach for analyzing the upward heaving of geologic strata due to pneumatic fracturing is to treat them as elastically deformed plates. This is accomplished through the Theory of Elasticity which expresses the state of strain, or relative displacement, within a solid elastic material to a series of mathematical equations. This section provides a brief summary of the development of general elastic theory, followed by a discussion of plate bending theory.

Love (1944) provides an excellent review of elasticity theory development, and the following discussion is drawn largely from this work. In 1638, Galileo was the first to consider the inherent character of the resistance of solids to rupture. He performed experiments to determine the resistance of a cantilever beam to rupture under an applied weight and concluded that the beam responded by deforming along an axis perpendicular to its length, and in the plane of the wall. Although Galileo failed to recognize the beam as an elastic body, this initial investigation established the direction which later investigators subsequently followed.

The next great landmark discovery in the development of the mathematical theory of elasticity was by Hooke in 1660. His contribution was "Hooke's Law" which defines the linear proportional relationship between stress, σ, and strain, ε, for any elastic material. The modern expression of Hooke's Law is as follows:

$$E = \sigma/\varepsilon \tag{3.1}$$

where E is the modulus of elasticity which can be established experimentally for any elastic material. Although Hooke identified the stress-strain relationship, it was not until a later date that the modulus of elasticity was investigated in any real detail. With Hooke's Law, the necessary experimental foundation for the elastic theory was established, and the determination of elastic strain was reduced to mathematical calculations.

In 1680, Mariotte applied the elastic theory to Galileo's problem of the flexure of a cantilever beam. He discovered that the resistance of a beam to flexure arises from the extension and contraction of its parts, and made the assumption that half of the beam was extended and the other half contracted. After Mariotte, numerous mathematicians attempted to calculate solutions for Galileo's problem and related theories of plates, bars, and columns. For example, in 1705, James Bernoulli investigated the elastic line which led to the notion that a flexural couple was proportional to the curvature for a bent rod. From this notion, he deduced that the work done in bending a rod is proportional to the square of the curvature. In 1740, Euler was able to obtain the differential equation of the curve described by Bernoulli.

In 1776, Coulomb studied the theory of flexure for beams of finite section. His work established a method for calculating the true position of the neutral axis, as well as the moment of the elastic forces. Coulomb was also the first to consider torsion in 1787, and later related shear strain to rupture.

In 1807, Thomas Young defined his modulus of elasticity (Young's Modulus) based on extensive experimentation and Hooke's Law. Young recognized shear as a form of elastic strain, although his work fell short of introducing the concept of the modulus of rigidity to express the shear resistance. The next major advance in the theory of elasticity

was by Navier in 1820 who formulated the general equations of displacement of an individual molecule using the Newtonian conception of the constitution of bodies. This led to an expression for the work done in a small relative displacement using the summation of moments of the forces exerted by all the other molecules on an individual molecule.

Around the same time, Cauchy (in 1822), using another approach, showed how the differential coefficients of the three components of displacement could be used to estimate the extension of every linear element of an elastic material in terms of what we now call the *principal axis of strain*. It is noted that when the initial stress state was assumed to be zero, the equations Cauchy developed were identical to those established by Navier.

In 1828, Poisson confirmed the validity of these equations in a manner very similar to Cauchy's approach. Aside from this, Poisson's most notable work was his development of the relationship between axial and lateral strain. This relationship is termed *Poisson's ratio* and is denoted by the Greek letter ν. It is expressed as follows:

$$\nu = |\ (\text{lateral strain/axial strain})\ | = -\ (\varepsilon_y/\varepsilon_x) = -\ (\varepsilon_z/\varepsilon_x) \qquad (3.2)$$

If Hooke's law is incorporated into Equation 3.2, the following expression is obtained:

$$\varepsilon_y = \varepsilon_z = -(\nu \cdot \sigma_x/E) \qquad (3.3)$$

for an axial load applied in the direction parallel to the x-axis, where the x, y, and z subscripts are in reference to the principal axis of strain developed by Cauchy.

In 1839, Stokes identified the conceptual relationship for the property which provides shear resistance, termed the modulus of rigidity, G. The modulus of rigidity and the modulus of elasticity, constitute the two fundamental kinds of elastic resistance in isotropic bodies. He proposed the following definition for the modulus of rigidity:

$$G = E/[2\cdot(1+\nu)] \tag{3.4}$$

The work up to this point established the real foundation for the Theory of Elasticity. Other investigators such as Lord Kelvin, Saint-Venant, and Michell provided further contributions in the years to follow. At the same time as the theory of elasticity was being refined, several investigators began to develop solutions for elastic plate bending.

Timoshenko (1953) and Love (1944) provide excellent reviews of plate bending theory development, and the following discussion is drawn largely from these works. Around 1767, Euler was the first to attack the problem of the deflection of elastic surfaces by regarding the elastic surface as two systems of stretched strings perpendicular to one another resulting in the differential equation for a bending elastic surface as follows:

$$\partial^2 w/\partial t^2 = A\cdot(\partial^2 w/\partial x^2) + B\cdot(\partial^2 w/\partial y^2) \tag{3.5}$$

where w is the deflection in the z-direction, t is the material thickness, and A and B are constants. Between 1786-1789 Jacques Bernoulli applied the same notion as Euler to the analysis of plates and obtained the following differential equation:

$$D\cdot(\partial^4 w/\partial x^4 + \partial^4 w/\partial y^4) = q \qquad (3.6)$$

where D is the flexural rigidity of the plate and q is the intensity of the lateral load. Bernoulli pointed out that this equation was only an approximation and was published only as a first attempt at solving the plate bending problem. Around 1813, Sophie Germain attempted to define the curvature of a deflected plate surface but made a mistake in her calculation. Lagrange, who was judging her work, noticed her error and was able to develop the equation as follows:

$$k\cdot(\partial^4 w/\partial x^4 + 2\cdot\partial^4 w/\partial x^2\partial y^2 + \partial^4 w/\partial y^4) + \partial^2 w/\partial t^2 = 0 \qquad (3.7)$$

where k is a constant. Poisson (1814) attempted to further improve the theory of plates by giving physical meaning to Equation 3.7. He assumed that a plate consisted of particles which had molecular forces acting on them proportional to the changes in molecular distance from one another. He found the constant k from Equation 3.7 to be proportional to the plate thickness squared and not cubed as it should be.

Finally, in 1820 Navier was credited with providing the first satisfactory theory for plate bending. Similar to Poisson, Navier assumed that the plate consisted of molecules distributed throughout the thickness of the plate and that their displacements during bending were parallel to the middle plane of the plate and proportional to the distance from that plane. From this he found the correct differential equation for any lateral loading as follows:

$$D\cdot(\partial^4 w/\partial x^4 + 2\cdot\partial^4 w/\partial x^2\partial y^2 + \partial^4 w/\partial y^4) = q \qquad (3.8)$$

where q is the load intensity and D is the flexural rigidity of the plate when Poisson's ratio is equal to 0.25. In 1822, Cauchy derived a differential equation which was similar to Navier's using a different approach. For the state of initial zero stress, Cauchy's equation is identical to the one found by Navier. Also, Kirchhoff (1850) derived the same differential equation for plate bending by yet a third method of analysis. Kirchoff's two assumptions were: (1) that each line which is initially perpendicular to the middle plane of the plate remains straight during bending and normal to the middle surface of the deflected plate; and (2) that elements of the middle plane of the plate do not undergo stretching during small deflections of plates under lateral load.

By manipulating the boundary conditions of Equation 3.8, the vertical displacement of a plate can be determined for a variety of loading and support conditions. Selected solutions that are relevant to the present study are presented in the next section.

3.2 Deformation Response to Igneous Laccolith Intrusions

Geologists have studied deformations of geologic strata resulting from igneous intrusions in some detail for laccoliths, sills, and dikes. Of particular interest to the present study are laccoliths, since the hypothesized mechanisms of their formation are similar to pneumatically-formed fractures.

A laccolith is defined by The American Geological Institute (1984) as *"a concordant igneous intrusion that has domed the overlying rocks and has a known or assumed flat floor and a postulated dikelike feeder beneath its thickest point. It is roughly circular in plan, less than five miles in diameter, and from a few feet to several hundred feet in thickness."* Simply stated, a laccolith is a dome-shaped igneous intrusion

paralleling the bedding plane of the country rock which causes bending or arching of the overlying strata. Comparatively, the observed plan shape of laccolith intrusions and ground surface deformations resulting from pneumatic fracturing are remarkably similar.

Gilbert (1877) was the first known geologist to recognize and study laccoliths (or "laccolite" as he called it) in his classic report on the Henry Mountains Region of Utah. When Gilbert entered the Henry Mountains for his study, he realized that these geologic formations were quite unique, so he carefully studied the form of these intrusions and attempted to understand the mechanisms of formation. His interpretations were based on analogies with available solutions to contemporary mechanics problems. Based on numerous field observations, Gilbert established his concept of the ideal forms of laccoliths as illustrated in Figure 3.1. The plan shape was a short oval (or an ellipse) where the ratio of the two axes did not exceed two to three. The measured laccolith heights did not exceed one-third of the diameters ($1H_L$:3L), and were frequently much less with the average ratio being $1H_L$:7L. The laccoliths were generally assumed to have a flat base, except where the intrusion followed the curvature of a pre-existing inferior arch in the bedding.

With the characteristic shape of a laccolith in mind, Gilbert hypothesized on the formation mechanism. The sequence begins as the intruding magma forces itself upward through the strata until it reaches a level of neutral geostatic stress (which Gilbert called hydrostatic equilibrium), i.e., the vertical and horizontal effective stresses are equal ($\sigma'_h/\sigma'_v=1$). At this point the intrusion expands as a thin sheet horizontally along a bedding plane. The horizontal extent of the intruding magma increases until it reaches a pressure large enough to overcome the resistance offered by the rigidity of the

overburden, at which point the fluid laccolith begins to dome upwardly since this is now the direction of least resistance. Gilbert assumed the laccolith was fed with magma from a central location by a dikelike feeder, although he was not physically able to observe one. In support of his hypothesized mechanism, Gilbert observed that the local regional structure did not exhibit any folded strata, and that the only possible explanation of the observed doming was the upward vertical pressure exerted by intruding fluid laccoliths.

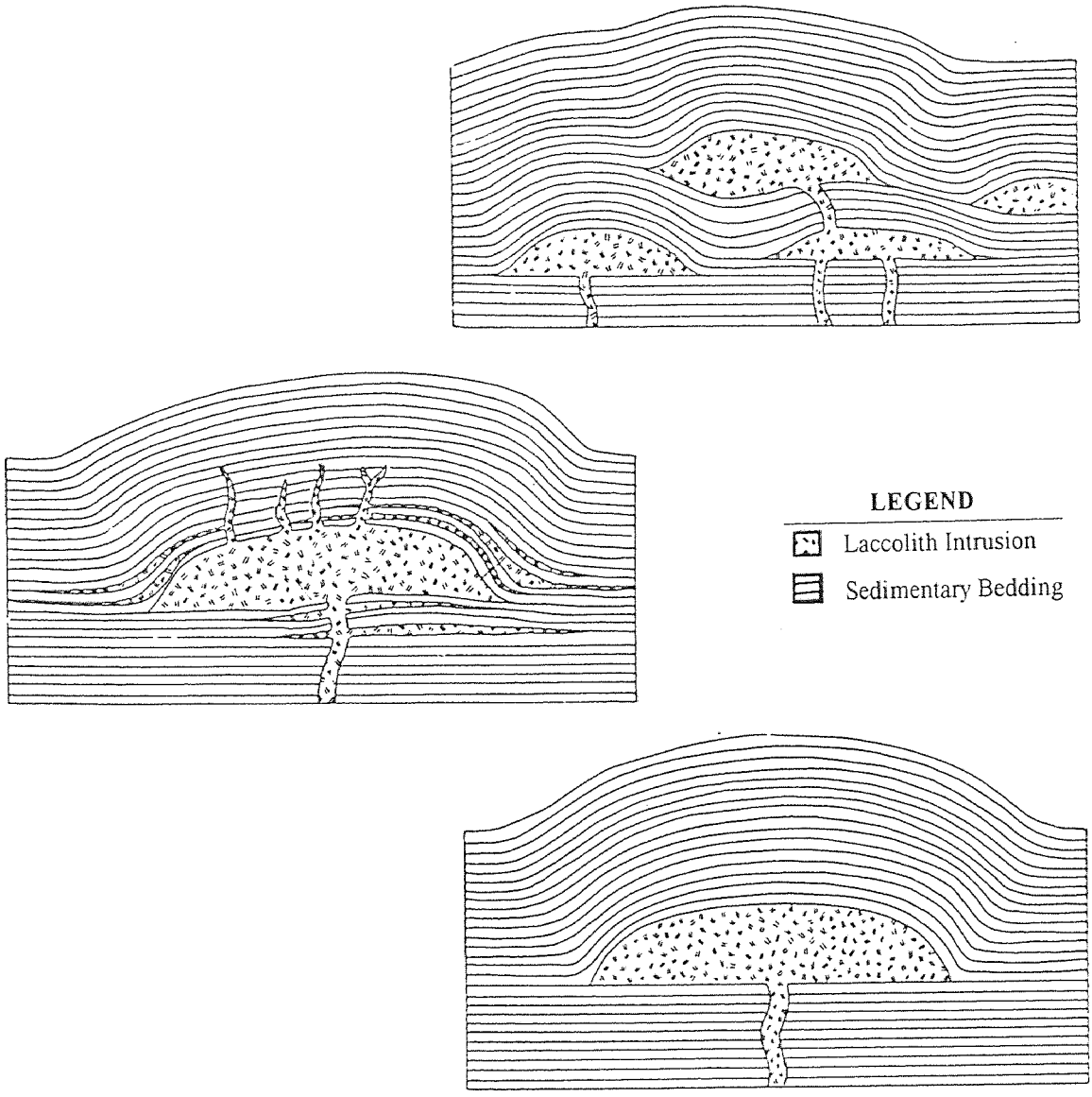

Figure 3.1 Gilbert's Concept of the Ideal Forms of Laccoliths (after Gilbert, 1877).

Using this mechanism of formation, Gilbert developed a mathematical expression to describe the dimensions of a laccolith. First, the basic assumptions of his conceptual model are presented followed by the derivation of the mathematical expression. Afterwards Gilbert's conclusions pertinent to this study are presented.

The conceptual model begins by assuming the uplift to be a monoclinal flexure encircling a point which was the structural equivalent of a fault. The analysis was further simplified by assuming that the faulted rock mass was a simple cylinder, of radius, R_C, and height, h_C, which projected above the ground surface an amount equal to the laccolith thickness. In order for a laccolith to grow, the uplift force, F_{up}, must overcome three components: the weight of the overburden, F_o; the faulting force due to cohesion around the cylinder's perimeter, F_f; and the fluid weight of the magma, F_m. The forces are shown schematically in Figure 3.2. Growth of the laccolith will eventually cease and maximum deformation will be attained when the uplift force equals the sum of the weights of overburden and magma, i.e., there is no force available to continue faulting. Gilbert called this the *limital thickness*.

Summing the forces in the vertical direction in Figure 3.2, we can see that the force due to the overburden, F_o, is a constant from which an equivalent portion of the uplift force can be used to cancel it out. Likewise, the force due to the self-weight of the magma, F_m, can also be canceled by a portion of the uplift force. With the components F_o and F_m removed, Gilbert derived mathematical expressions to explain the formative mechanism of a laccolith.

The remaining variables affecting the mechanism are the faulting force, F_f, and the portion of the uplift pressure remaining after F_o and F_m have been canceled out, which will

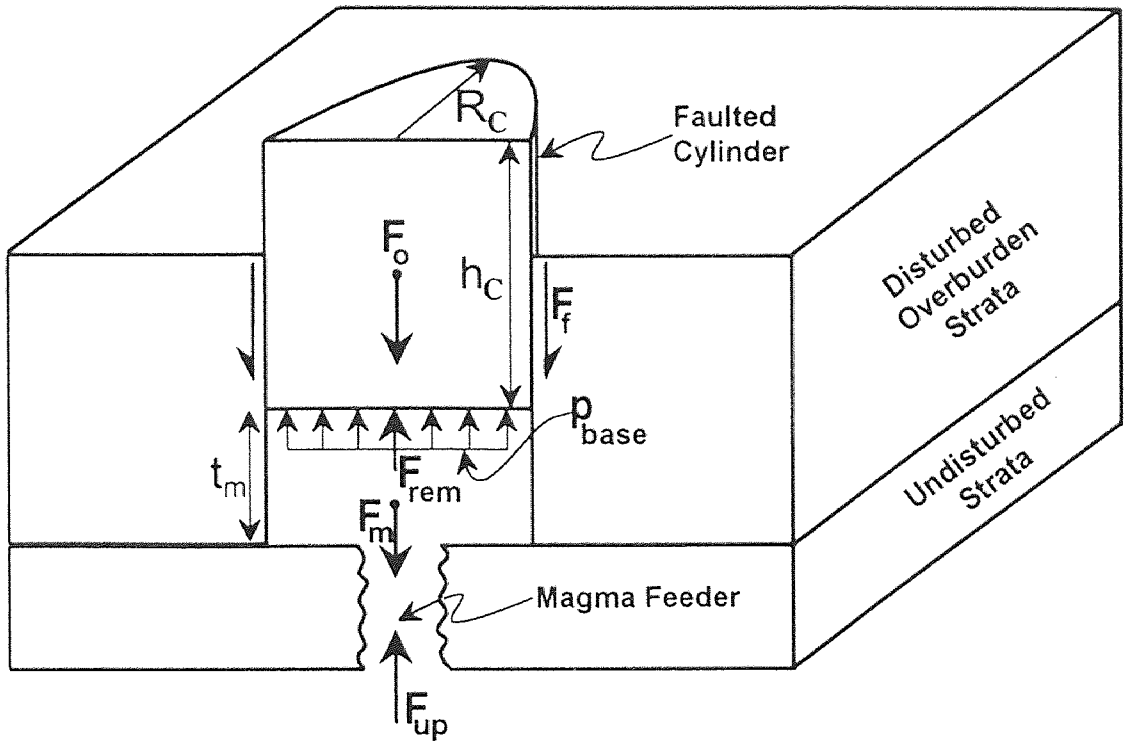

where: F_{up} = uplift force due to the magma intrusion, $F_{up} = F_o + F_f + F_m$

F_{rem}= uplift force remaining to overcome the resisting force due to cohesion, where $F_{rem} = F_{up} - F_o - F_m = p_{base} \cdot \pi \cdot R_C^2$, where p_{base} is the magma pressure applied to the base of the laccolith and R_C is radius of the laccolith in plan.

F_o = force due to the overburden, $F_o = \gamma_{overburden} \cdot \pi \cdot R_C^2 \cdot h_C$, where $\gamma_{overburden}$ is the unit weight of the overburden material, and h_C is the overburden thickness.

F_f = faulting force due to cohesion around the perimeter, $F_f = 2 \cdot \pi \cdot R_C \cdot c \cdot h_C$, where c is the cohesion of the overburden material.

F_m = force due to the magma weight, $F_m = \gamma_{magma} \cdot \pi \cdot R_C^2 \cdot t_m$, where t_m is the magma thickness above the laccolith base and γ_{magma} is the magma unit weight.

Figure 3.2 Gilbert's Hypothesized Mechanism of Laccolith Formation.

be referred to as F_{rem}. Gilbert proposed the following mathematical expression to relate the resisting force due to cohesion with the laccolith dimensions:

$$F_f = h_C \cdot C \cdot c \tag{3.9}$$

where F_f is the resisting faulting force due to cohesion; h_C is the height of the cylinder; C is the circumference of the cylinder; and c is the cohesion of the material.

The remaining uplift force, F_{rem}, from the magma is transmitted equally to all points on the base of the cylinder. It is described as the magma pressure at the base of the laccolith, p_{base}, times the area of the cylinder as follows:

$$F_{rem} = A_L \cdot p_{base} = (C^2/4 \cdot \pi) \cdot p_{base} \tag{3.10}$$

where F_{rem} is the portion of magma uplift force remaining to overcome the resisting cohesion force ($F_{rem} = F_{up} - F_o - F_m$); A_L is the base area of the laccolith which is equal to $C^2/4 \cdot \pi$; and p_{base} is the upward fluid pressure exerted to the laccolith base.

Gilbert noted that for a given cylinder height, it was possible to assign a cohesion value so large that the force F_f would be greater than the force F_{rem}, or so small that the force F_f would be less than the force F_{rem}. This suggested that there was a lower limit below which a laccolith could not be formed. This reinforced the hypothesis that when the dike-like intrusion reached a level of neutral geostatic stress, the magma would then expand along a bedding plane as a thin sheet until its horizontal extent became so large that it could then overcome the resistance from the rigidity of the overburden, and the

intrusion could begin to cause an uplift. At this point, the upward vertical direction offered the least resistance, and the forces F_{rem} and F_f can be assumed to be equal to one another. By equating Equations 3.9 and 3.10, the following relationship is developed:

$$C^2 \cdot (p_{base}/4 \cdot \pi) = h_C \cdot C \cdot c \tag{3.11}$$

which simplifies to:

$$C = h_C \cdot c/(p_{base}/4 \cdot \pi) \tag{3.12}$$

It is apparent from this expression that the diameter of a laccolith is proportional to the depth at which it intrudes beneath the ground surface.

At this stage, Gilbert accounted for the fact that the laccolith was formed by flexing and not faulting of the overlying strata. Therefore, the flexing force was not linearly proportional to the depth of cover, but rather it varied in a much more rapid manner. To account for this effect, Gilbert made some analogies with Rankine's work on elastic beams, but could not adapt an exact solution to the laccolith mechanism. The main problem was that the elasticity of the overlying strata were imperfect, so gross approximations were required to fit the model to his field observations.

To account for the obvious non-linearity with depth, Equation 3.9 was modified as follows:

$$F_f = h_C^a \cdot C \cdot c \tag{3.13}$$

where a is the depth exponent. Based on his observations, Gilbert estimated the value of exponent a to be between 2 and 3. The final expression for the laccolith circumference

was developed by incorporating this modification into Equation 3.12

$$C = h_C^{a} \cdot c/(p_{base}/4 \cdot \pi) \qquad (3.14)$$

Overall, Gilbert came to a number of conclusions on the mechanism of laccolith formation. Those most relevant to the current analysis of pneumatically fractured formations are:

(1) There is a *limital area* required for the formation of a laccolith. As the above equations illustrate, at a specific depth below the surface, intruding magma with a specific geostatic stress cannot form a laccolith unless the limital area is exceeded.

(2) At constant pressure, the limital area is a direct function of the depth below the surface of the intrusion. As the depth increases, so does the limital area.

Following Gilbert's initial comprehensive study and definition of the basic mechanism, studies of laccoliths continued through the 20th century. Those with relevance include **Davis (1925)** who analyzed the horizontal spread of igneous intrusions and established some general relationships for laccoliths and sills. He found sills to be 30 to 50 times as wide as their thickness, while laccoliths were typically 5 to 10 times as wide as their thickness. Davis stated that a laccolithic intrusion ceased to spread and began to swell when the lifting force, which increases with the square of the spreading radius, exceeded the resistance to flexure and rigidity of the overlying strata. His studies also identified intrusion rate as an important factor in the final geometry of the intrusion. Rapid intrusions lead to a flexure of the overlying strata and the formation of a laccolith, while slower intrusions were more likely to develop into wide-spreading thin sills.

Hunt (1953) revisited Gilbert's analysis of the Henry Mountains Region of Utah using more advanced measuring instruments. While not offering any new ideas on the formative mechanisms, his studies did provide a detailed table listing the dimensions of the Henry Mountains intrusions which are useful for evaluating and calibrating mathematical models. Hunt suggested that the varying diameters of the magma feeders of the laccoliths in the Henry Mountains were directly related to the magnitude of uplift for each laccolith dome. This is a logical hypothesis assuming that the remaining uplift force, F_{rem}, that Gilbert described is a direct result of the uplift force, F_{up}, caused by the intruding magma, which will increase in proportion to the volume of intruding magma.

Pollard and Johnson (Pollard, 1968; Johnson, 1970; and Pollard and Johnson, 1973) were the first modern geologists to significantly extend Gilbert's work through a rigorous study of mechanics. They applied elastic bending theory to laccoliths by modeling them as a stack of thin elastic plates. The laccolith geometries analyzed are illustrated in Figure 3.3 and range from elliptical to anticlinal in plan, with a circular shape as a special case of an ellipse. They also modeled different upward pressure distributions including uniform, linear tapering, and point loads (see Figure 3.4). Initially, they developed the model for bending of a single geologic layer, but afterwards expanded the model to incorporate multiple geologic layers with varying elastic properties.

The actual plan of a laccolith is described mathematically for the model by an elliptical boundary defined by $(x^2/a^2) + (y^2/b^2) = 1$, where "a" represents the short axis and "b" represents the long axis. As indicated in Figure 3.3, intrusions with plans ranging from circular (a=b) to anticlinal ($b=\infty$) can be studied by varying the lengths of the two axis of the elliptical plan. The forces resisting bending that must be overcome are: the

effective overburden pressure, internal forces due to flexural rigidity of each geologic layer, and frictional (or cohesive) forces between adjacent geologic layers (the last is considered to be negligible in their model).

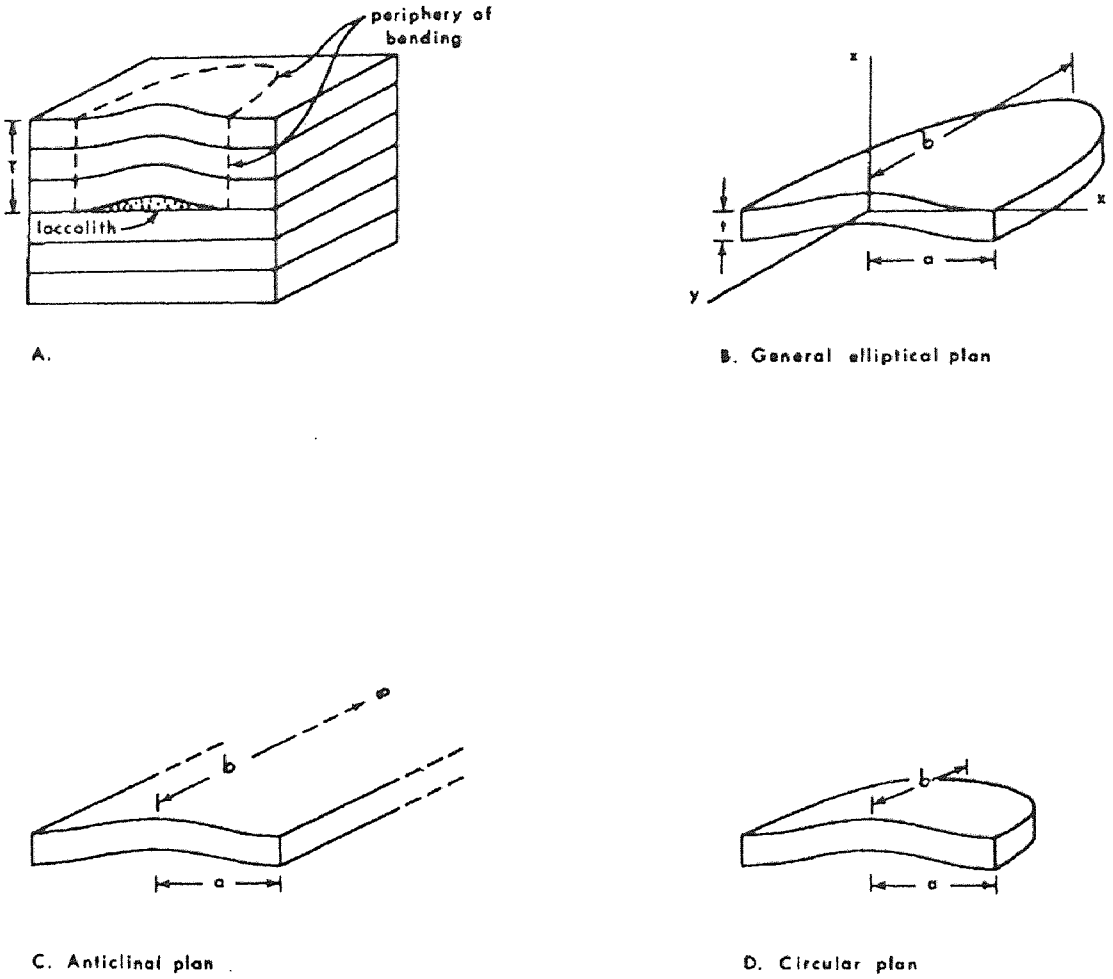

Figure 3.3 Idealization of Strata Overlying a Laccolith Intrusion:
(A) Magma intrudes between two sedimentary layers at a depth of T;
(B) A single layer is isolated with thickness, t, and an elliptical plan with long axis, b, and short axis, a;
(C) b = ∞ for an "anticlinal" plan; and
(D) b = a for a circular plan (after Pollard and Johnson, 1973).

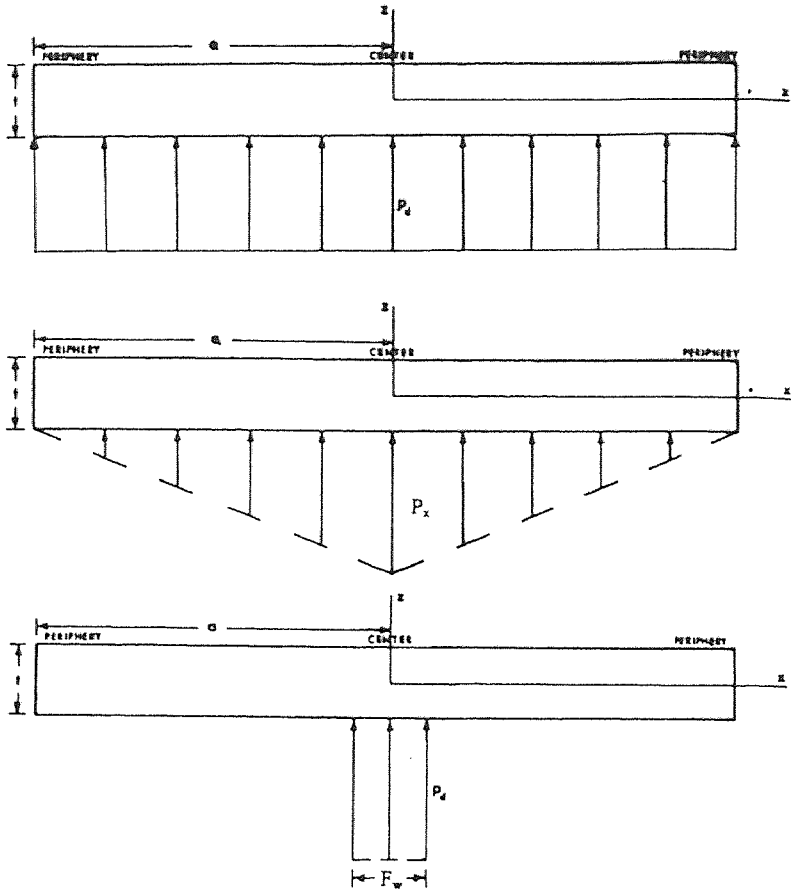

Figure 3.4 Schematics Representing the Various Pressure Distributions Studied in the Model. (A) Uniform Load, (B) Linear Tapering Load, and (C) Point Load; (modified after Pollard and Johnson, 1973).

The analysis begins with the standard differential equation of vertical displacement for plate bending determined by Navier (described previously as Equation 3.8):

$$(\partial^4 w/\partial x^4) + (2\partial^4 w/\partial x^2 \partial y^2) + (\partial^4 w/\partial y^4) = (p_d/D) \qquad (3.15)$$

where w is the displacement in the z-direction; x, y, z represent the Cartesian coordinate system; p_d is the driving pressure ($p_d = p_{inj} - t \cdot \gamma_{overburden}$), where p_{inj} is the total injected magma pressure and ($t \cdot \gamma_{overburden}$) is the lithostatic pressure due to the overburden weight; and D is the flexural rigidity of the bending material.

An important variable in this equation is the flexural rigidity of the deformed strata, D, which is defined as:

$$D = B \cdot t^3/12 \tag{3.16}$$

where B is the elastic modulus which is calculated as $B = E/(1-\nu^2)$ (E is the modulus of elasticity and ν is Poisson's ratio); and t is the thickness of a single layer of overburden.

Equation 3.15 can now be solved for various boundary conditions and pressure distributions. For a uniform pressure distribution, the general case of an elliptical boundary is presented. The elliptical area of the intrusion has a constant pressure applied which can be shown as:

$$p_d = \text{constant, for } (x^2/a^2 + y^2/b^2) \leq 1 \tag{3.17}$$

The boundary conditions can be inferred from Figure 3.3. As indicated, the displacement and slope are zero at the edges of the deformed region of the elliptical area which leads to the following expression for the displacement, *w*:

$$w = \partial w/\partial x = \partial w/\partial y = 0, \text{ for } (x^2/a^2 + y^2/b^2) = 1 \tag{3.18}$$

Using a solution presented by Love (1944), Pollard and Johnson obtained the expression for any specific displacement, *w*, for an elliptical laccolith subject to a uniform pressure distribution:

$$w = (p_d/8 \cdot D) \cdot (1 - x^2/a^2 - y^2/b^2)^2/(3/a^4 + 3/b^4 + 2/a^2 \cdot b^2) \tag{3.19}$$

Solving for the anticlinal case the equation reduces to the following:

$$w_{b=\infty} = (p_d/24 \cdot D) \cdot (a^4 - 2a^2 \cdot x^2 + x^4) \tag{3.20}$$

Similarly, for the circular case, the following is obtained:

$$w_{b=a} = (p_d/64 \cdot D) \cdot (a^4 - 2a^2 \cdot x^2 + x^4) \tag{3.21}$$

Pollard and Johnson concluded from their results that the surface deflection increases with the spreading radius of the laccolith raised to the fourth power ($w \propto a^4$), and the overburden resists bending with the thickness raised to the third power, ($D \propto t^3$). The driving pressure, p_d, is only raised to the first power and therefore has a minor effect on the displacement.

By calculating the upper and lower displacement limits for both plan shapes subject to uniform pressure distributions, all the intermediate values can be determined and are presented graphically in Figure 3.5.

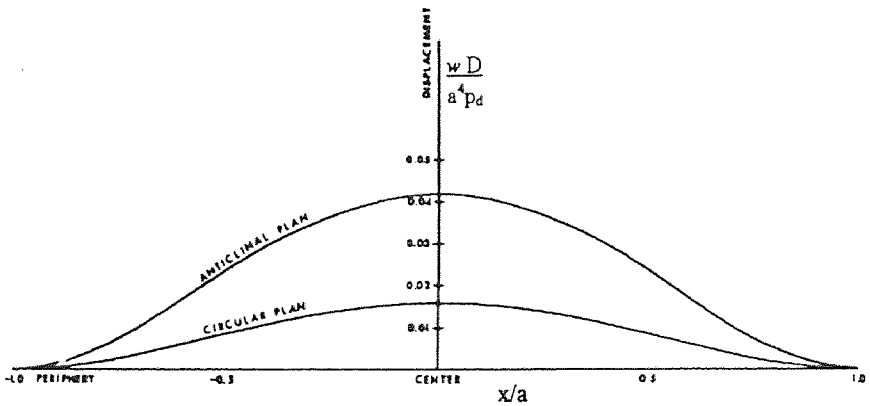

Figure 3.5 Cross-Sectional Forms of the Layers Overlying Laccolith Plans Ranging From a Circle to an Anticlinal Plan for a Uniformly Distributed Pressure.

It is also possible to develop a relationship for an anticlinal laccolith with a linear tapering pressure distribution (see Figure 3.4). For this case the driving pressure is no longer constant and becomes a function of the radial distance from the magma feeder:

$$P_x = p_d \cdot [1 - (|x|/a)] \tag{3.22}$$

where P_x is the driving pressure at a distance x from the feeder; and $|x|$ is the absolute value of the distance x from the laccolith center.

Pollard and Johnson solved this case for an anticlinal plate subjected to a linear tapering pressure distribution as follows:

$$w = [p_d \cdot (1 - (|x|/a))] \cdot [(1-\nu^2)] \cdot [10 \cdot x^4 - (2 \cdot |x|^5/a) - 15 \cdot a^2 \cdot x^2 + 7 \cdot a^4] / [20 \cdot E \cdot t^3] \tag{3.23}$$

While Pollard and Johnson did not solve this case for a circular plate subjected to a linear tapering pressure distribution, a solution was found from Timoshenko and Woinowsky-Krieger (1959):

$$w = [p_d \cdot (1 - (|x|/a))] \cdot [(1-\nu^2)] \cdot [(a^2 - x^2 - y^2)^2] / [16 \cdot E \cdot t^3] \tag{3.24}$$

Pollard and Johnson also considered the displacement resulting from an anticlinal laccolith subject to a point load pressure distribution shown as (C) in Figure 3.4. However, this is of little concern to the present study and will not be presented.

Next, the model authors proposed a method of relating multiple layers of overburden to the laccolith driven deformation. The model represents the multiple layers by summing individual layers of effective thickness which frictionlessly slide over one another on one extreme. This effective thickness is a single layer of representative thickness which is used to replace the same resistance to bending as a multilayer system with similar length and elastic modulus. The other extreme was modeled as multiple layers perfectly bonded together. In nature the actual action of the deforming overburden layers lies somewhere between these two extremes.

The total overburden is composed of *n* free-sliding layers of individual thickness, t_i, and elastic modulus, E_i. The effective flexural rigidity, D_e, for the multiple layers is found by summing the individual flexural rigidities as follows:

$$D_e = \sum [(E_i \cdot t_i^3)/(12 \cdot (1-\nu^2))], \text{ from } i=1 \text{ to } n \qquad (3.25)$$

If the layers have approximately the same elastic moduli, then this equation simplifies to:

$$D_e = (E \cdot T_e^3)/[12 \cdot (1-\nu^2)] \qquad (3.26)$$

where T_e is the effective thickness of the multiple layers of overburden, which is calculated by the following equation:

$$T_e^3 = \sum (t_i^3), \text{ from } i=1 \text{ to } n \qquad (3.27)$$

Simplifying further, if the individual layers have approximately the same thickness, then the total thickness of the stack, T, becomes equal to the number of layers, *n*, times the equivalent thickness. This provides an equation for the effective thickness as follows:

$$T_e = (T \cdot t^2)^{1/3} \tag{3.28}$$

which shows the effective thickness is considerably smaller than the actual thickness.

Price (1975) performed his own calculation for an anticlinal laccolith with a uniformly distributed load and found a relationship for the resulting maximum theoretical displacement, w_{max}:

$$w_{max} = (p_d \cdot a^4)/(2 \cdot E \cdot t^3) \tag{3.29}$$

where p_d is the magmatic pressure in excess of the gravitational load; a is one-half the lateral extent of the intrusion; E is the modulus of elasticity of the overburden layers; and t is the thickness of the overburden. An examination of Equation 3.29 reveals that it is nearly identical to Equation 3.20 (at x = 0) presented previously by Pollard and Johnson. The only difference between the two equations is that the term $(1-\nu^2)$ has been omitted from Equation 3.29.

Price evaluated the model of Pollard and Johnson, and concluded that their model provided a mechanics solution for the development of a sill rather than a laccolith. In addition, he determined that the remarkable degree of similarity between the curve from Pollard's and Johnson's theoretical model and the actual shape of laccolith roofs observed in the field were purely coincidental.

Turcotte and Schubert (1982) also examined the mechanics of laccolithic intrusion. Their analysis was restricted to an anticlinal laccolith where the magma flowed along a crack. Using analogies with plate bending theory, they assumed that the overburden thickness, t, was bent upward by the magmatic pressure, p_{inj}. Loading of the overburden layers is represented by p_d, which is the part of the upward pressure force, p_{inj}, in excess of the lithostatic pressure, $t \cdot \gamma_{overburden}$, represented by the following equation:

$$p_d = p_{inj} - t \cdot \gamma_{overburden} \tag{3.30}$$

It is noted that this is identical to the loading assumptions made by Pollard and Johnson.

Next, their analysis reduces the standard differential equation by examining the point of maximum displacement where the x term is zero. The resulting differential equation becomes:

$$d^4w/dx^4 = p_d/D \tag{3.31}$$

where D is the flexural rigidity of the overlying layers which is then calculated as follows:

$$D = (E \cdot t^3)/12 \cdot (1-\nu^2) \tag{3.32}$$

where t is the layer thickness, E is the modulus of elasticity, and ν is Poisson's ratio. If we apply the following boundary conditions: $w = dw/dx = 0$ at $x = \pm L/2$, where L is the lateral extent of the laccolith, the above equation will yield the following expression for displacement of an anticlinal laccolith subjected to a uniform pressure distribution:

$$w = [(p_d)\cdot(1-\nu^2)]\cdot[(x^4) - (L^2\cdot x^2/2) + (L^4/16)]/[2\cdot E\cdot t^3] \quad (3.33)$$

It is apparent that this result is essentially identical to that derived by Pollard and Johnson for the anticlinal plate subjected to a uniform pressure distribution, only the nomenclature varies slightly (i.e., $L = 2\cdot a$).

3.3 Criteria for Differential Movement

3.3.1 Criteria for Differential Movements of Foundations

It is difficult to determine the exact magnitude of differential foundation movement that will cause significant damage to structures. Such an analysis must consider soil heterogeneities, structural material uncertainties, settlement rates, contact pressures, footing stiffness and connection rigidity, and the nature of the actual loads transmitted to the foundation units (Holtz, 1991). The complexity and uncertainty of these parameters has discouraged investigators from developing an acceptable analytical solution for tolerable structural movements. Consequently, empirical methods have been established based on observations of actual building movements and resulting damages. These methods can be traced to a limited number of investigators who conducted thorough studies relating to differential movements. Some of the guidelines established by the earliest studies were subsequently reevaluated, combined, and modified by later investigators. A brief chronology of the classic studies of allowable structural movements and related interpretations are presented below.

Skempton and MacDonald (1956) were the first investigators to conduct a comprehensive study on building settlements. Their study was based on data from 98

buildings, 40 of which had experienced settlement damage. The work resulted in actual observed performance limitations and design guidelines for estimating settlement and deflection ratio damage limits for traditional frame buildings as presented in Table 3.1.

Table 3.1 Settlement Damage Limits and Design Recommendations for Frame Buildings (after Skempton and MacDonald, 1956).

Criterion	Isolated Foundations	Rafts (Mat Foundations)
Deflection Ratio (Angular Distortion)	1/300	1/300
Greatest Differential Settlement for Clays	1¾ (1½) in.	1¾ (1½) in.
Greatest Differential Settlement for Sands	1¼ (1) in.	1¼ (1) in.
Maximum Settlement for Clays	3 (2½) in.	3-5 (2½-4) in.
Maximum Settlement for Sands	2 (1½) in.	2-3 (1½-2½) in.

Note: Values Recommended for design are given in parentheses. 1 in. = 25.4 mm

Polshin and Tokar (1957) reported on over 25 years of observations of 100 structures in the Soviet Union and published values of maximum allowable differential movement in the 1955 USSR Building Code (Table 3.2). Their study also correlated threshold values of visible cracking with critical tensile strain in structures leading to estimates of 0.05-0.10% for brick, and 0.03-0.05% for concrete (Schuring, et. al., 1988).

Sowers (1962) developed limiting settlement values for various structure types based on total settlement, tilting, and differential movement (see Table 3.3). His work was based on a worldwide study of damage experienced by existing structures.

Bjerrum (1963) produced a chart of limiting deflection ratios which provided a graduated scale of damage limits. The scale covered a deflection ratio range of (1/750) for sensitive machinery to (1/150) for structural damage to buildings (see Figure 3.6).

Table 3.2 Allowable Settlement Criteria from the 1955 USSR Building Code (after Polshin and Tokar, 1957).

Type of Structure	Sand and Hard Clay	Plastic Clay
(a) β		
Civil- and Industrial-Building Column Foundations:		
For steel and reinforced concrete structures	0.002	0.002
For end rows of columns with brick cladding	0.007	0.001
For structures where auxiliary strain does not arise during nonuniform settlement of foundations	0.005	0.005
Tilt of smokestacks, towers, silos, etc.	0.004	0.004
Craneways	0.003	0.003
(b) Δ/L_l		
Plain brick walls:		
For multistory dwellings and civil buildings		
at $L_l/H_B \leq 3$	0.0003	0.0004
at $L_l/H_B \geq 5$	0.0005	0.0007
For one-story mills	0.0010	0.0010

Table 3.3 Limiting Settlements for Structures (after Sowers, 1962).

Type of Movement	Limiting Factor	Maximum Allowable Settlement or Differential Movement
Total Settlement	Drainage	6 to 12 in.
	Access	12 to 24 in.
	Probability of nonuniform settlement	
	Masonry-walled structures	1 to 2 in.
	Framed Structures	2 to 4 in.
	Smokestacks, silos, mats	3 to 12 in.
Tilting	Stability against overturning	Depends on height and weight
	Tilting of smokestacks, towers	$0.004 \cdot B_F$
	Rolling of trucks, etc.	$0.01 \cdot L_l$
	Stacking of goods	$0.01 \cdot L_l$
	Machine operation--cotton loom	$0.003 \cdot L_l$
	Machine operation--turbo generator	$0.0002 \cdot L_l$
	Crane rails	$0.003 \cdot L_l$
	Drainage of floors	$0.01 \cdot L_l$ to $0.02 \cdot L_l$
Differential movement	High continuous brick walls	$0.0005 \cdot L_l$ to $0.001 \cdot L_l$
	One-story brick mill building, wall cracking	$0.001 \cdot L_l$ to $0.02 \cdot L_l$
	Plaster cracking (gypsum)	$0.001 \cdot L_l$
	Reinforced-concrete building frame	$0.0025 \cdot L_l$ to $0.004 \cdot L_l$
	Reinforced-concrete building curtain walls	$0.003 \cdot L_l$
	Steel frame, continuous	$0.002 \cdot L_l$
	Simple steel frame	$0.005 \cdot L_l$

Note: B_F = base width.
L_l = distance between adjacent columns that settle different amounts, or between any two points that settle differently. Higher values of allowable settlement are for regular settlements and more tolerant structures. Lower values are for irregular settlements and critical structures.

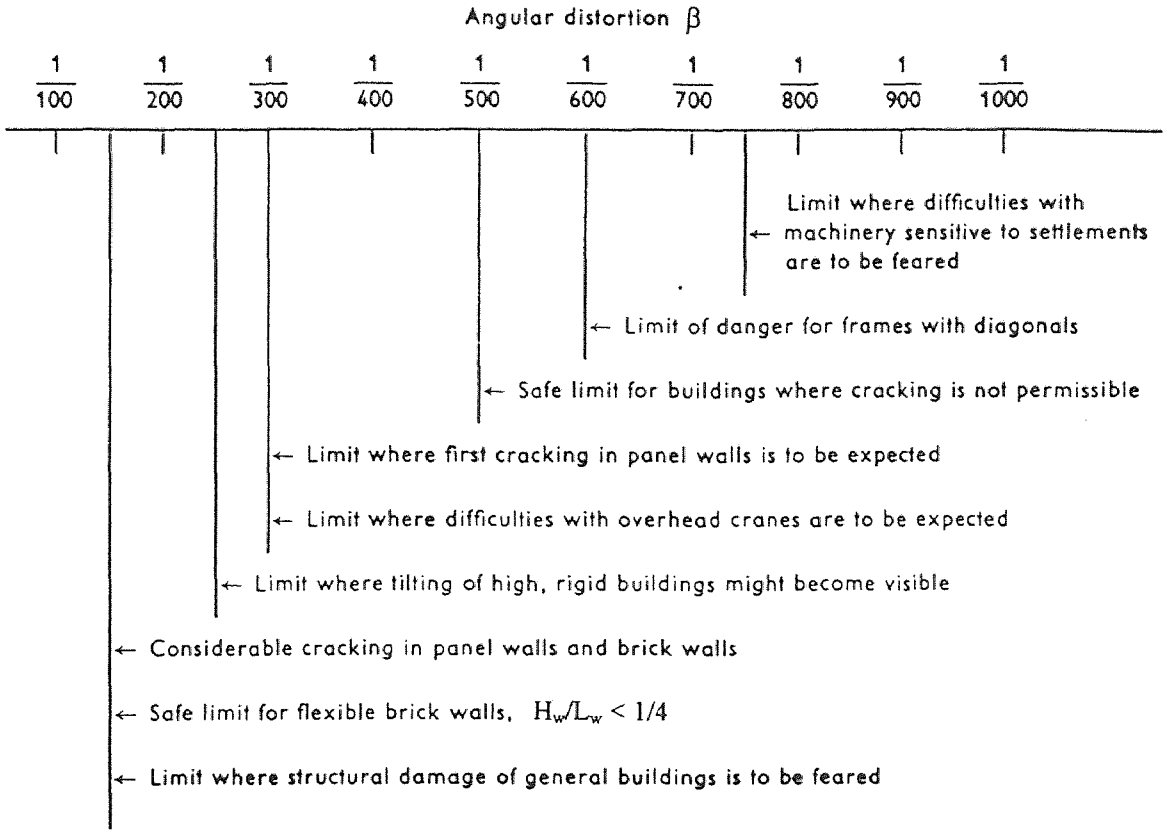

Figure 3.6 Limiting Deflection Ratios for Buildings (after Bjerrum, 1963).

Feld (1965) performed a review of numerous case histories on settling structures and cited the difficulty of establishing a general guideline for all structure types. He also emphasized that structures were often capable of adjusting to localized increased stresses resulting from differential movements, particularly resulting from slow movements.

D'Appolonia (1971) presented guidance for controlling differential movements of foundations due to adjacent construction operations. His study produced criteria for limiting architectural damage for various construction types as illustrated in Figure 3.7.

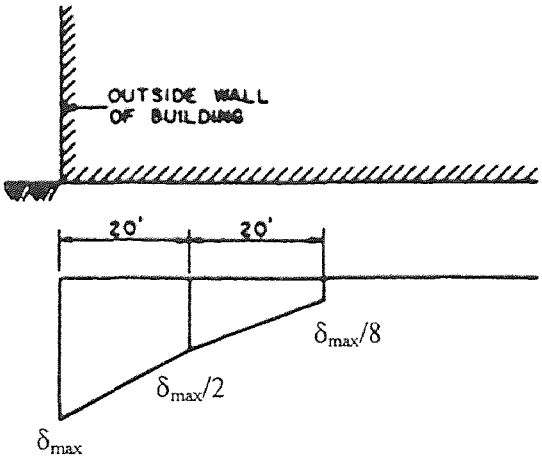

STRUCTURE	δ_{max}
BRICK	2 inches
CONCRETE OR CINDER BLOCK	3/4 inches
MONUMENTAL STONE	1 inch
STEEL OR CONCRETE FRAME	2 inches

Figure 3.7 Maximum Tolerable Settlement to Prevent Architectural Damage (after D'Appolonia, 1971).

Tschebotarioff (1973) attempted to relate the maximum allowable settlement of various superstructure types into the 1962 USSR Building Code. Allowable values ranged from 3.15 in. for flexible structures to 12.0 in. for rigid structures as shown in Table 3.4.

Table 3.4 Limit Values of Settlement, δ_{lim}, Permitted by the 1962 USSR Building Code for Different Building Types (modified after Tschebotarioff, 1973).

Type of Superstructure and Foundation	Limit Value, δ_{lim} (in.)
1. Buildings of large precast panels or blocks without structural frame	3.15 in. (8 cm)
2. Buildings with nonreinforced brick or large-block walls on strip or isolated spread footings for ratios of wall length , L_w, to its height, H_w:	
$L_w/H_w \geq 2.5$	3.15 in. (8 cm)
$L_w/H_w \leq 1.5$	4.00 in. (10 cm)
3. Buildings with brick or large-block walls strengthened by reinforced -concrete or armored brick belts (irrespective of the ratio L_w/H_w)	6.00 in. (15 cm)
4. Fully framed buildings	4.00 in. (10 cm)
5. Monolithic reinforced concrete foundations of blast furnaces, smokestacks, silos, water towers, etc.	12.00 in. (30 cm)
6. Foundations of one-story-high industrial building and similarly structured buildings with column spans of:	
19.7 ft (6 m)	3.15 in. (8 cm) [a]
39.4 ft (12 m)	4.72 in. (12 cm) [a]

[a] = total settlements.

Burland and Wroth (1974), in a state-of-the-art report, defined universal parameters for describing settlement and distortion of buildings. This greatly increased the understanding of the various early studies and allowed for direct comparison of their limiting movement. Their study was based on the concept that visible cracking starts when the critical tensile strain is reached. They developed a model in which a building may be represented by a simple rectangular beam. Results of the model analysis suggested that the deflection ratio be limited for certain structure types. Diagonal strain was found to be critical for both framed structures and reinforced load-bearing walls, while bending strain was found to be the critical factor for unreinforced masonry wall structures.

Their comparison of actual foundation performance for various structure types with the guidelines presented in the classic studies of Skempton and MacDonald (1956) and Polshin and Tokar (1957), provided some important insight. Skempton's and MacDonald's safe limit for angular distortion (relative rotation) of 1/500 was found to be satisfactory for framed buildings of both traditional and modern construction, but not for buildings with load-bearing walls. The safe limits of relative rotation and deflection ratio presented by Polshin and Tokar are much more satisfactory for buildings with load-bearing walls and precast reinforced concrete panels. One of their most significant findings is the inadequacy that both of these criteria provide for load-bearing walls undergoing "hogging." Hogging is defined as upward concave heaving as occurs on expansive clays or downward concave differential settlement which can result from adjacent excavations. Their observations showed that this type of movement caused cracking at values of Δ/L_l which were half that proposed by Polshin and Tokar.

Grant, Christian, and Vanmarcke (1974) reexamined the 1956 classic study of Skempton and MacDonald by investigating settlement for 95 buildings, 56 of which had damage. Their conclusions confirmed that beyond a deflection ratio of 1/300, structures generally experience some damage. Contrary to popular beliefs, they concluded that the rate of movement had very little effect on the degree of damage experienced by structures except for the extreme cases of fast or slow movement (Schuring, et. al., 1988).

Myslivec and Kysela (1978) incorporated allowable settlement criteria into the Czechoslovakia building code. The tolerable movement criteria were governed by the structure type, rigidity, and rate of movement as presented in Table 3.5.

Table 3.5 Ultimate Values of the Settlement of Foundations (according to CSN 73 1001) (modified after Myslivec and Kysela, 1978).

Type of Building	The Foundation Soil Consolidates			
	Very Quickly (for example, sands)		Slowly (for example, clays)	
	Difference of Settlement δ/L_1	Total Settlement δ (cm)	Difference of Settlement δ/L_1	Total Settlement δ (cm)
1. Buildings:	0.0005	6	0.0007	8
bricks and blocks	0.0007	6	0.001	8
bricks, block reinforced with concrete strips	0.001	8	0.0013	10
reinforced concrete skeleton	0.0007	6	0.001	8
2. Structures:				
statically determinate	0.003	10	0.003	10
statically indeterminate steel	0.0015	6	0.002	8
statically indeterminate reinforced concrete	0.001	4	0.0015	6
rigid and massive foundation				
to a height of 20 m	0.005	20	0.005	20
higher than 20 m (chimneys)	0.002	10	0.002	10
3. Crane tracks with bridge crane longitudinally and laterally	0.0015	--	0.0015	--

There are a few additional comprehensive references which contain useful summaries of the allowable movement of structures based on these earlier studies including: Wahls (1981), U.S. Navy (1982) (in NAVFAC), Meyerhof & Fellenius (1985) (in the Canadian Foundation Engineering Manual), Perloff (1975) and Holtz (1991) (in the 1st and 2nd editions, respectively, of the Foundation Engineering Handbook), U.S. Army Corps of Engineers (1994) (in Design Manual No. 9). These references have often formatted the criteria so that the values can easily be incorporated into the design process.

The acceptable limits in which a structure may distort when applied to differential movements based on geotechnical engineering literature has been presented. Various settlement and distortion parameters have been used by various researchers, but the present study will use the unifying parameters presented graphically by Burland and Wroth (1974) in Figure 3.8 and defined below as follows:

δ = total settlement, or the absolute vertical movement of a particular foundation.

δ_D = differential settlement, or difference in total movement between two foundations.

ω = tilt, or the rotation of the entire superstructure.

θ = rotation, or the angle between the horizontal and any two foundations (or two points in a single foundation).

β = relative rotation or angular distortion, which is the angle between the overall tilt of a structure and the inclination of a specific portion of it.

α = angular strain, which is the change in θ.

Δ = relative deflection, or settlement of a point relative to a straight line connecting two reference points at a distance, S, apart. Positive Δ indicates a situation known as sagging, and negative Δ indicates a situation known as hogging.

Δ/L_1 = deflection ratio, also known as the sagging ratio or the hogging ratio.

In most structures the tolerable limit is governed by aesthetic and serviceability requirements, and not structural requirements. Different structures often vary greatly in their ability and acceptability of tolerance to movements. In most cases of settlement damage, unsightly cracks, jamming doors and windows, and other similar problems will develop long before a structures integrity is at risk (Coduto, 1994). These variations depend on numerous factors, the most obvious are the following (Coduto, 1994): type of structure (wood, steel, masonry, etc.), use of the structure (museum versus an industrial building), presence of sensitive finishes (tiled floors versus asphalt paving), and the rigidity of the structure (which will determine how loads due to movements will be redistributed).

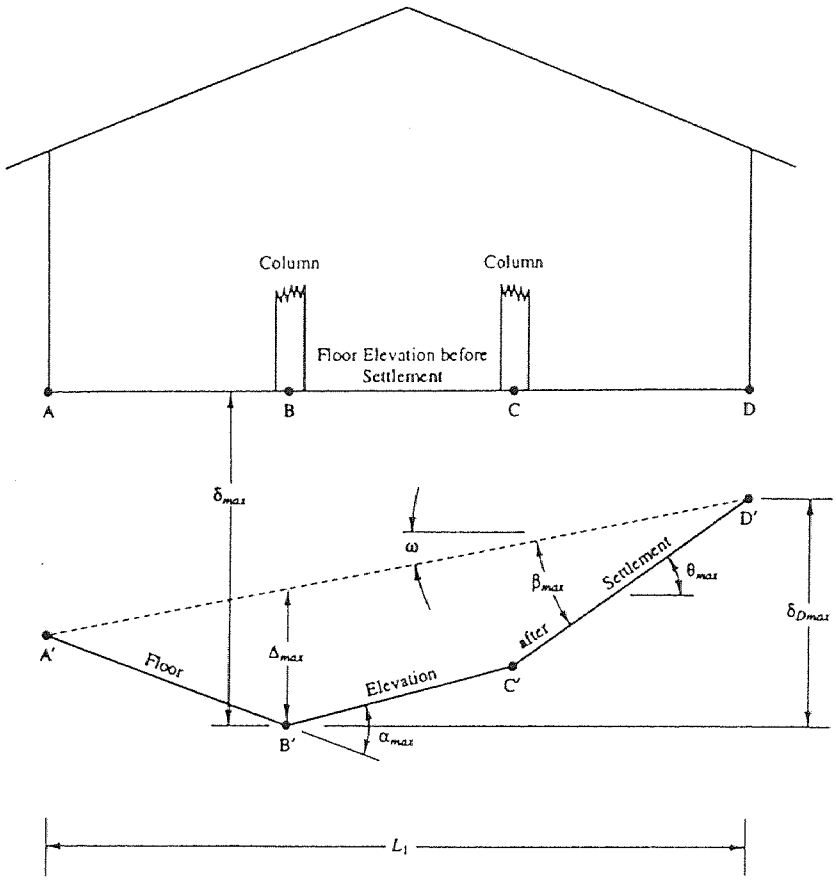

Figure 3.8 Parameters Describing the Movement of Building Foundations (after Burland and Wroth, 1974 and Coduto, 1994).

Although serious structural distress rarely results from foundation movements, it does occasionally occur and an understanding of the potential distress situations is warranted for this study. Schuring, Raghu, and Dauenheimer (1988) provide an excellent presentation of the most common distress situations which may affect the structural integrity of a building, and the following discussion is drawn largely from this work.

Their presentation discusses the three most common distress situations which may affect the structural integrity of a building. These situations are (1) the loss of beam bearing, (2) tilting and/or buckling of walls, and (3) development of secondary stresses in members. Although each distress situation will be unique in nature due to varying material and construction types, a generic examination is useful in understanding the factors relating to these differing situations resulting from differential building movements. For ease in understanding the behavior of structures resulting from differential movements, the analyses presented were restricted to two-dimensional movements.

Loss of Beam Bearing: The situation of a simple beam (assumed pinned at one end) which loses bearing due to differential movements between the supports were studied separately for the cases of vertical movement and horizontal movement. The case for vertical differential displacement is illustrated in Figure 3.9, where L_l is the span length, b_d is the bearing distance, and δp is the differential settlement. The study found that a differential settlement of 3 to 6 feet would be required for the beam to slip off the support, but points out that failure would likely occur prior to this due to local overstress and crushing of either the beam or the support. Therefore, the study investigated values for the differential settlement at which point one of the support's bearing distances has

decreased to 30% of its full value, designated as δp_{30}. A summary of the results for numerous assumed values is shown in Table 3.6.

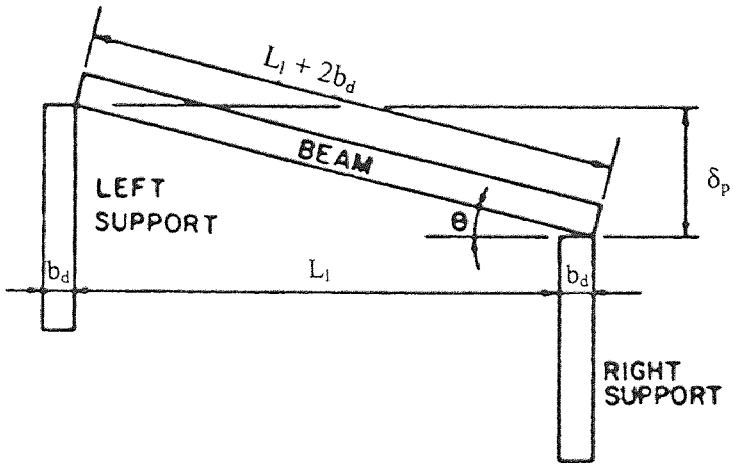

Figure 3.9 Beam Bearing Loss Analysis Parameters (after Schuring, et. al., 1988).

Table 3.6 Summary of Analysis of Beam Bearing Loss (after Schuring, et. al., 1988).

Summary of Analysis					
L_l m (ft)	b_d m (ft)	δp m (ft)	$\delta p/L_l$	θ (degrees)	δp_{30} m (ft)
4.6 (15)	0.1 (0.33)	0.94 (3.1)	0.21	12.0	0.79 (2.6)
4.6 (15)	0.15 (0.5)	1.2 (3.8)	0.26	14.8	0.98 (3.2)
7.6 (25)	0.15 (0.5)	1.5 (5.0)	0.20	11.5	1.3 (4.2)
10.7 (35)	0.15 (0.5)	1.8 (5.98)	0.17	9.7	1.5 (4.9)
NOTE: δp_{30} is the differential settlement corresponding to 30% bearing at the left support in Figure 3.9.					

From the surprisingly large values for differential settlement shown in Table 3.6, the authors concluded that a failure of this sort would be extremely unlikely. Comparing Bjerrum's 1/150 deflection ratio for the threshold of structural damage to this distress situation corresponds to a beam bearing of over 99%.

In contrast to the vertical movements, the case of beam bearing loss due to horizontal spreading of the beam supports is much more likely to occur. Horizontal movements equivalent to the bearing distance of one support will result in a failure and must therefore be carefully limited when large differential movements are taking place.

Tilting and Buckling of Walls: The analysis of tilting and buckling walls involve two main considerations, overturning stability and secondary stresses. The topic of secondary stresses will be considered separately in the next section.

The study utilizes the criterion used in standard design practice for eccentrically loaded footings which requires that the resultant vertical force is projected through the kern of the footing. With the force projected through the kern, the contact pressures between the footing and soil or rock remain entirely in compression. Figure 3.10 shows a schematic of an idealized tilted wall which rests on a spread footing which was used for the analysis for defining limits of tilt which would cause structural concern. In actuality, most walls have additional support provided from floors, roofs, and other walls within a structure, so the analysis provides values for the absolute worst case scenario. For the wall presented in Figure 3.10, the kern is defined as the middle third of the footing and the center of gravity is located at the mid-height of the wall. Table 3.7 presents the results of the analysis for determining the amount of wall tilt when the center of gravity begins to violate the kern criteria. Also presented in Table 3.7 is a stability condition where the center of gravity passes through the outside edge of the footing, termed *unstable equilibrium* in physics. Another topic analyzed was wall buckling due to lateral thrust, but this topic is not of any real concern to the current study, so any results or discussion has been omitted.

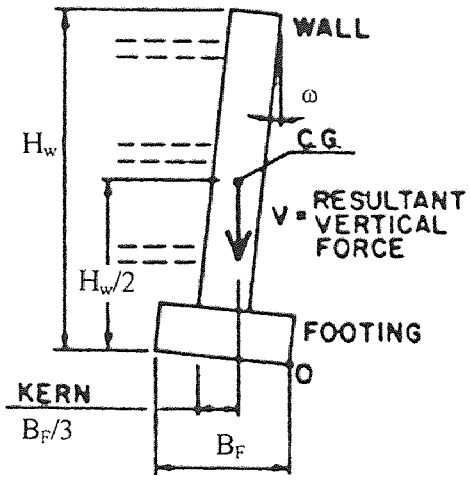

Figure 3.10 Schematic of Tilted Wall for Analysis (after Schuring, et. al., 1988).

Table 3.7 Summary of Analysis for Tilted Wall (after Schuring, et. al., 1988).

H_w m (ft)	B_F m (ft)	V Through Edge of Kern		V Through Point O	
		ω (degrees)	Tilt %	ω (degrees)	Tilt %
3 (10)	0.5 (1.5)	2.9	5	8.5	15
6.1 (20)	0.6 (2)	1.9	3.3	5.7	10
9.1 (30)	0.9 (3)	1.9	3.3	5.7	10
12.2 (40)	1.2 (4)	1.9	3.3	5.7	10
NOTE: V = Resultant vertical force and O is a point on the footing as illustrated in Figure 3.10.					

Conclusions drawn from the analysis found that a tilt of 3 to 5% would violate the kern criteria at which point the structural integrity of the building would be of concern. The unstable equilibrium analysis resulted in tilts of 10 to 15% at which point overturning stability became a concern and contact pressures at the outer edge of the footing approach infinity. Failure can potentially occur long before overturning stability reaches its limit due to secondary stresses which will be discussed later.

Secondary Stresses: Differential movements alter the stress regime assumed by the building designer due to secondary stresses introduced as members deform and loads are redistributed. These secondary stresses pose two critical problems: (1) the new stresses may exceed the original primary design stresses, and (2) the new stresses may occur in members which are incapable of resisting this new kind or magnitude of stress.

Eccentricities caused by tilting or bending of vertical load bearing members often induces secondary stresses. Adjusting the allowable stress to account for slenderness effects and load eccentricities is based on the assumption that lateral elastic buckling governs for the analysis. The vertical wall schematic the authors used for their analysis of secondary stresses due to load eccentricities and slenderness values is illustrated in Figure 3.11. By varying the parameters shown in Figure 3.11, Table 3.8 was developed which summarizes the percent of the original concentric load capacity of the wall for a practical range of slenderness values (H_w/B_w) and end eccentricities (e_1/e_2).

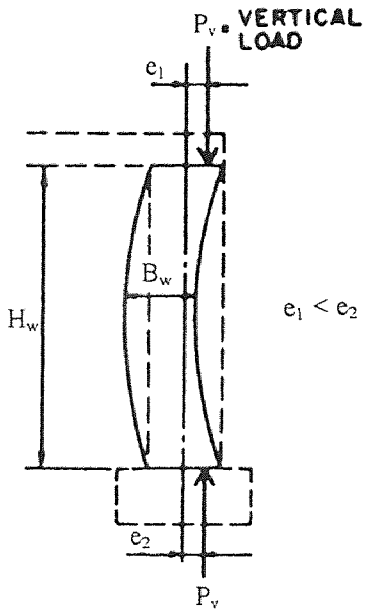

Figure 3.11 Schematic Used for Analysis of Secondary Effects in Walls (after Schuring, et. al., 1988).

Table 3.8 Summary of Analysis for Secondary Effects in Walls (after Schuring, et. al., 1988).

H_w/B_w	e_1/e_2	Percent of Original Concentric Load		
		e/B_w =0.0	e/B_w = 0.16	e/B_w = 0.33
5	0.0	100	72	47
5	1.0	100	66	33
10	0.0	93	67	44
10	1.0	93	61	31
20	0.0	67	44	22
20	1.0	40	26	13
30	0.0	40	29	19

Conclusions drawn from the study are that for large e/B_w ratios, the carrying capacity of the wall is reduced dramatically to only 13% of its concentric load capacity. Although the analysis was based on the assumption that elastic buckling governs, wall types that have negligible tensile strength and low compressive strengths may have failures due to local inelastic distress causing failure by crushing and cracking (e.g. unreinforced masonry).

3.3.2 Criteria for Differential Movement of Utilities

Establishment of allowable differential movement criteria for utility piping subjected to pneumatic injections is a difficult task. First, there are numerous piping materials with varying properties available on the market. Second, the nature of the products being carried by the piping greatly influences the risks of movement and rupture of the pipe. Finally, construction practices for installation of the piping are quite variable.

Utility piping materials can be divided into three major classifications: rigid, semi-rigid, and flexible pipes. Each of these can be further divided into generic material types including metals, plastics, ceramics, and composites. Table 3.9 gives classifications for the most common piping materials. Those which are commonly encountered at contaminated industrial sites are indicated by an asterisk (*).

The mechanical material characteristics, combined with the interaction with the geologic formation, govern the ability of a pipe to resist differential movements, and consequently, the manner in which the pipe will fail. The mechanical characteristics include: the modulus of elasticity, toughness, tensile strength, compressive strength, density, ductility, and hardness. The influence of these properties on the different material types is briefly summarized in Table 3.10. No single property controls the behavior of a pipe material. Rather, it is the combination of these characteristics that determine how a pipe will respond to movement.

Table 3.9 Different Classes and Divisions of Piping Materials.

Material Type	Pipe Classification		
	Rigid	***Semi-Rigid***	***Flexible***
Metals	cast iron*	steel*	copper
Plastics	---------	nylon polyethylene	PVC* rubber
Ceramics	concrete* clay* glass	brick	---------
Composites	---------	---------	fiberglass*
Notes: * = pipes most commonly encountered at contaminated industrial sites.			

Table 3.10 Pipe Materials Characteristics (modified after Newey and Weaver, 1990).

Material Characteristic	*Plastic Pipes*	*Metal Pipes*	*Ceramic Pipes*	*Composite Pipes (particularly fiberglass)*
Modulus of Elasticity, E	either low or very high	high	high	moderate to high
Toughness	some good and some poor	good	poor	low to moderate
Tensile Strength	some fair and some poor	high	low	moderate
Compressive Strength	fair	fairly high	high	low
Density	low	high	medium	low
Ductility	some good and some have none	good	none	low
Hardness (or wear resistance)	some low and some moderate	moderate	high	low to moderate

A practical way of evaluating different pipe materials (or classifications) is to use the concept of deflection limit. The deflection limit is simply the maximum amount of axial deflection per unit length that a pipe material can tolerate before permanent deformation takes place. For example, the most commonly used semi-rigid material is steel pipe, which is generally designed with a maximum deflection limit of 7.5%. This value already contains a factor of safety of four (American Institute of Steel Construction, 1984). For design and evaluation of pneumatic fracturing, the other semi-rigid materials can be expected to have similar deflection limits. Similarly, flexible pipes such as some plastic and fiberglass pipes are designed for a maximum deflection limit of 5% or greater, which also contains a factor of safety of about four. Rigid materials such as cast iron, concrete, and clay pipes can generally tolerate only small deflections (i.e., <0.5%) before cracking or brittle failure (American Concrete Pipe Association, 1980). Consequently, for these pipes, the nature of the product being carried becomes the limiting factor.

The nature of the product being carried within the pipe is probably the most important factor in determining allowable movement criteria for utility pipes. The consequences of failure for certain utilities can be extremely costly, and may even be life-threatening to workers associated with the fracturing. It is therefore mandatory that every possible precaution be exercised when fracturing is conducted in the vicinity of critical utilities. Utility services such as natural gas, chemical lines, and fuel supplies offer the greatest potential danger if failure occurs. Electrical conduits also pose a potential hazard, primarily related to cutting or drilling through of the utility itself. Other utility lines such as storm drains, water lines, and sewer lines pose less of a risk if damaged.

CHAPTER 4

ANALYTICAL DESIGN MODEL

The analytical design model for predicting ground surface deformations due to pneumatic fracturing was developed in three sequential steps. First, the characteristic mathematical form of the ground deformation was regressed from actual field data from various pneumatic fracturing sites (Section 4.1). In the second step, this mathematical form was related to the elastic plate bending and laccolith formation models previously described in Chapter 3 to develop a model equation for predicting surface deformations (Section 4.2). The third step involved the superposition of a structure over the deforming geologic formation (Section 4.3). These steps are discussed in the following sections.

4.1 Defining the Characteristic Ground Deformation Curve

In order to establish the characteristic mathematical form of the deformed ground surface resulting from pneumatic fracturing, data from all previous project sites were reviewed. An initial review and compilation of the ground deformation data was conducted by Imholte (1995) as a Masters Project Report. The report also explores two existing models for predicting ground deformations in geologic formations. This report served as a starting point for the more comprehensive investigation presented in this chapter.

In general, evaluation of ground deformation data revealed that the plan shape of the ground deformation was nearly circular, and was symmetrical around the point of injection. Deviations from this shape could usually be attributed to either geologic heterogeneities of the formation or underground obstructions. Since a basic and necessary

assumption of the model is that the formation is homogeneous and isotropic, it was necessary to screen the available data. The following data screening criteria were applied:

- Only sites with sufficient geologic reconnaissance data available were considered.
- A sufficient number of ground deformation monitoring points were necessary to develop a reliable depiction of the deformed surface. This eliminated some of the early research data.
- Sites with overlying fill materials were not used for the initial model development.
- Injections which overlapped existing fractures from adjacent wells were not used since the geologic formation had been previously disturbed.
- Injections with abnormal equipment operation were not considered.
- Maximum surface deformations at the injection point had to be at least an 1/8-inch to be considered. Smaller surface deformation magnitudes were usually associated with deep injections and failed to provide reliable development of the ground surface deformation curve.

It is noted that much of the omitted data were still useful for later model validation since they provided valuable insight into more complex formation responses (e.g., surface fill).

Following the initial screening, the acceptable surface deformation data were plotted using Microsoft Excel in the sample format shown in Figure 4.1. A regression analysis was then performed to develop the best fit mathematical equation for the deformed ground surface. Various types of trendlines were considered including: linear, second-order, third-order, fourth-order, fifth-order, and sixth-order polynomials. This

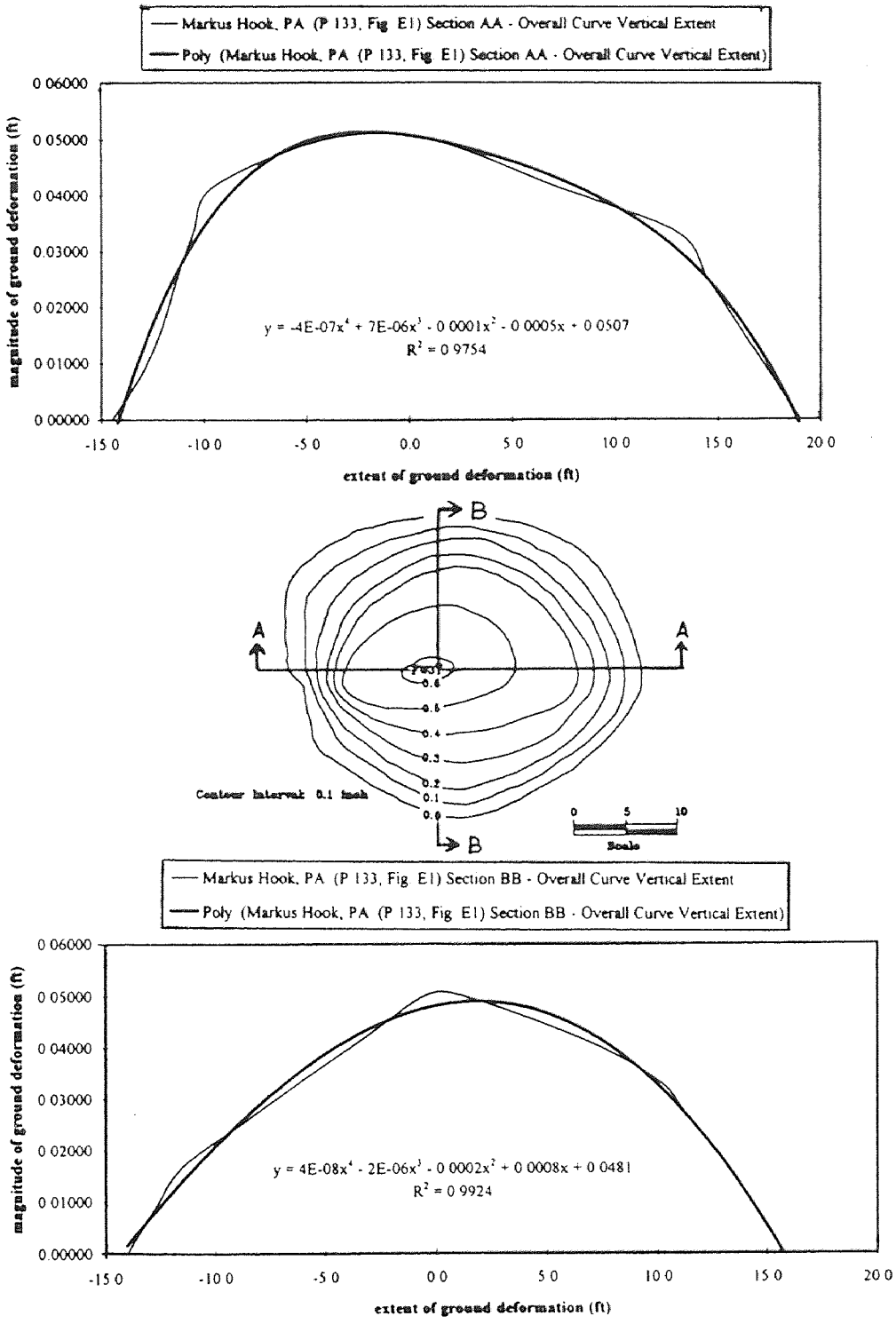

Figure 4.1 Typical Plan and Sections of Plotted Ground Surface Deformation Curves with Fitted Fourth-Degree Polynomial Equations.

process was performed for the deformation data from numerous sites and geologic conditions with the intent of identifying a consistent trend.

In order to facilitate the regression, symmetrical curves were developed based on the actual data. This was done to reduce the effects of minor geologic anomalies and measurement errors. The symmetrical curves were developed by taking one of two perpendicular cross sections (i.e., Section AA or BB as seen in Figure 4.1) of the deformed ground surface and adding a mirrored image of both the positive and negative ends of each section. This process resulted in four curves for each pneumatic injection studied. Figure 4.2 illustrates this process applied to the curves presented previously in Figure 4.1.

Based on a thorough evaluation of the data, the curve shape which consistently represented the field data was the fourth-order polynomial equation using curvilinear regression. The basic form of this equation is:

$$w = A_c \cdot x^4 + B_c \cdot x^3 + C_c \cdot x^2 + D_c \cdot x + F_c \qquad (4.1)$$

where w is the heave magnitude; x is the heave radius; and A_c, B_c, C_c, D_c, and F_c are the equation coefficients.

Another important trend observed in the regression results was that the first and third-degree coefficients of the equation were typically 10 to 20 orders of magnitude smaller than the other terms in the equation, i.e. they were nearly zero. This result was expected and is mathematically consistent with the symmetry of the curve.

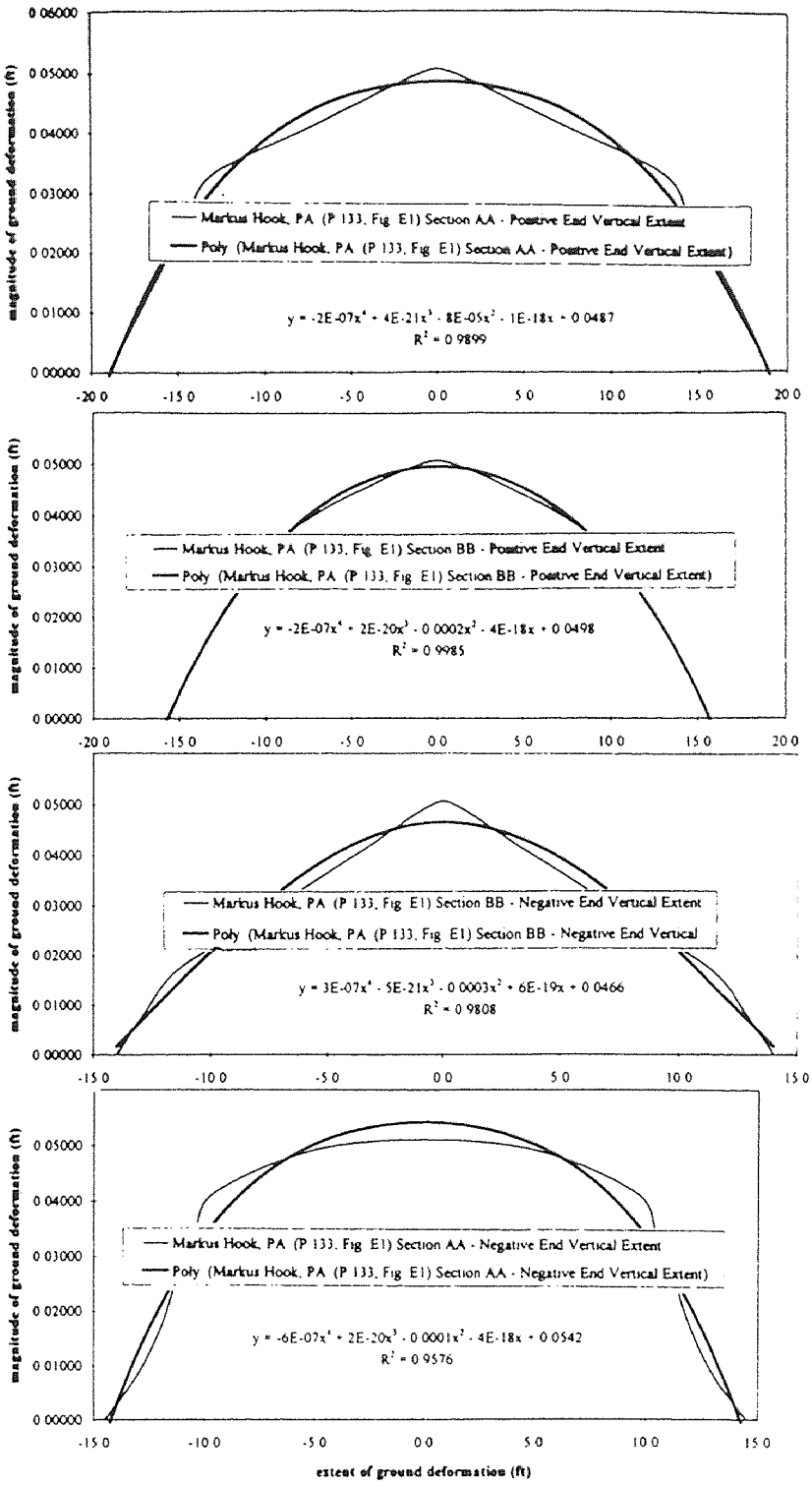

Figure 4.2 Surface Heave Cross-Sections Modified to Create a Symmetrical Profile.

The equations of ground surface deformation developed from five different sites are presented in Table 4.1. The coefficients of the equations have been averaged for each site and are unique to the geologic formation at that site. The small magnitudes of the first and third degree terms is apparent. Based upon these results, the final generic form of the ground surface deformation equation was simplified to the following:

$$w = A_c \cdot x^4 + C_c \cdot x^2 + F_c \qquad (4.2)$$

Table 4.1 Averaged Ground Deformation Curves for Fractured Sites.

Site Location	Geologic Formation	Ground Surface Deformation Equations
Hillsborough	Siltstone	$w = (1\text{x}10^{-8})\cdot x^4 + (1\text{x}10^{-22})\cdot x^3 - (4\text{x}10^{-5})\cdot x^2 - (7\text{x}10^{-20})\cdot x + 0.0256$
Flemington	Siltstone	$w = (5\text{x}10^{-8})\cdot x^4 - (4\text{x}10^{-22})\cdot x^3 - (7\text{x}10^{-5})\cdot x^2 + (2\text{x}10^{-19})\cdot x + 0.0209$
Marcus Hook	Clayey Silt, Silty Clay (CL, ML)	$w = (1\text{x}10^{-6})\cdot x^4 - (5\text{x}10^{-21})\cdot x^3 - (4\text{x}10^{-4})\cdot x^2 + (2\text{x}10^{-19})\cdot x + 0.0436$
Frelinghuysen	Sandy Silt and Clay (CL, ML)	$w = (7\text{x}10^{-6})\cdot x^4 + (1\text{x}10^{-20})\cdot x^3 - (5\text{x}10^{-4})\cdot x^2 - (5\text{x}10^{-19})\cdot x + 0.0161$
Oklahoma	Silty Clay (CL)	$w = (3\text{x}10^{-8})\cdot x^4 - (2\text{x}10^{-21})\cdot x^3 - (8\text{x}10^{-5})\cdot x^2 + (6\text{x}10^{-19})\cdot x + 0.0266$

In order to verify that these equations actually represented the individual fractures at each site, the data were normalized using the following ratio:

$$\text{heave ratio} = w_{act} / w_{mod} \qquad (4.3)$$

in which w_{act} is the actual heave magnitude, and w_{mod} is the heave calculated from the average equation. A typical normalized plot is shown in Figure 4.3, and a complete set for all injections studied is contained in Appendix A.

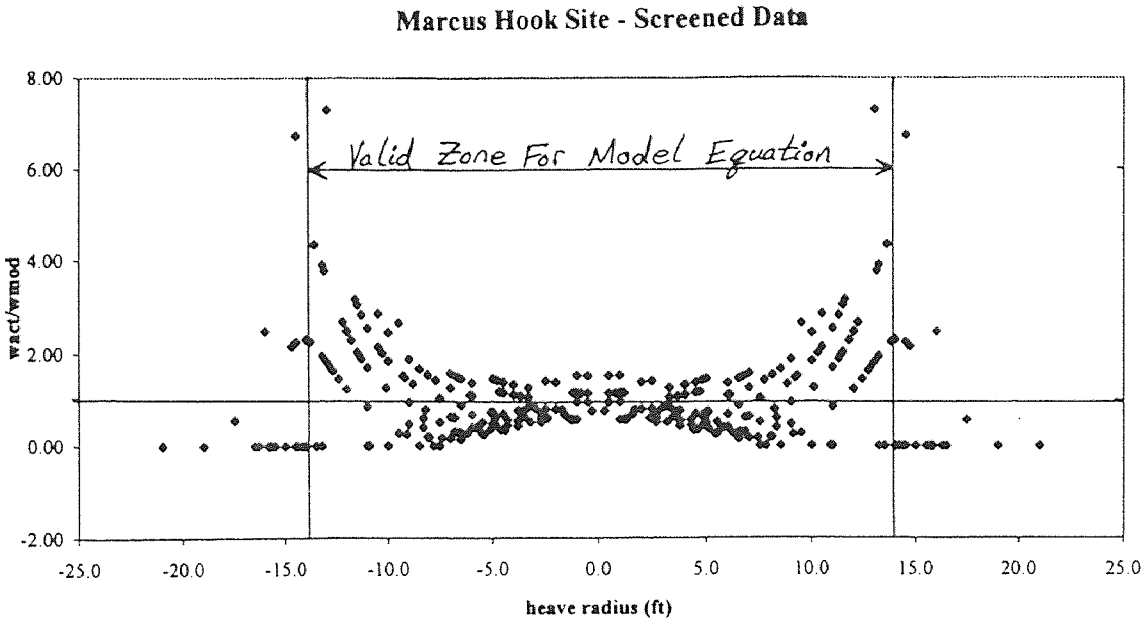

Figure 4.3 Typical Normalized Plot for Validation of the Averaged Heave Curves.

A review of the normalized plots confirm that the average equations are reasonably representative of the individual curves within the central region of heave, typically within a range of ± 50%. However, towards the extremities of the plot where the deformed surface tapers off to zero, deviations from the model increase. This behavior is attributed to two mathematical phenomena: (1) at the extremities, the surface deformation magnitudes in the divisor approach zero, thus inflating the ratio; and (2) the final radius lengths of the model fracture and the actual fracture do not always coincide. Fortunately, the outer region of fracture influence is of least concern during pneumatic fracturing owing to its relatively small magnitude.

4.2 Relating the Characteristic Ground Surface Deformation Curve with the Elastic Bending Models

The next step in model development was relating the characteristic ground deformation curve with the elastic plate bending solutions presented previously in Chapter 3. Although a number of solutions are available for various plan shapes and loading cases, two were evaluated in detail for development of the design model: (1) an anticlinal plate subjected to a uniform pressure distribution; and (2) a circular plate subjected to a linear tapering pressure distribution. Both of these are depicted in Figure 4.4 and the justification for selecting these cases will now be discussed.

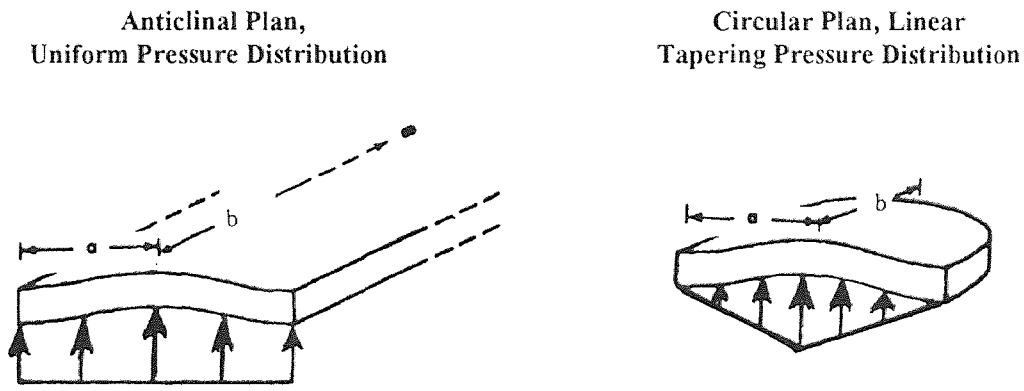

Figure 4.4 Extreme Plan Shapes and Loading Distribution Cases Causing Deformations.

The first case, an anticlinal plate subjected to a uniform pressure distribution, probably represents the upper extreme limit of surface ground deformation which could be observed in the field. The application of this case to geologic formations has been studied by Pollard and Johnson (1973), and Turcotte and Schubert (1982) as discussed previously in Chapter 3. This case is simply a modified analysis of a beam subjected to a uniform

load and fixed at both ends. The obvious advantage of this case is that the solution has been well studied in structural engineering and has a high confidence level. However, owing to the pressure leak-off and friction losses which occur radially during the pneumatic fracturing process (discussed in Chapter 2), this case will likely overestimate the ground deformation magnitude by at least several times.

The second case, that of a circular plate subjected to a linear tapering pressure distribution, is likely to be more representative of actual field conditions. It reflects the characteristic circular plan shape of the deflection and also depicts a more realistic pressure distribution. This case presumably represents the lower extreme of ground surface deformation, since the only lesser loading case is a point load distribution, and this would not realistically occur during the pneumatic fracturing process.

The first step in the analysis is to factor Equation 4.2 into the following form:

$$w = A_c \cdot [x^4 + (C_c / A_c) \cdot x^2 + (F_c / A_c)] \tag{4.4}$$

It is now possible to establish a direct relation between this equation and the previously presented elastic solutions. For an anticlinal plate subjected to a uniform pressure, Equation 4.4 becomes:

$$w = [p_d \cdot (1-\nu^2)/(2 \cdot E \cdot t^3)] \cdot [(x^4 - 2 \cdot a^2 \cdot x^2 + a^4) \tag{4.5}$$

where the coefficients may be expressed as:

$$A_c = [p_d \cdot (1-\nu^2)/(2 \cdot E \cdot t^3)] \tag{4.6}$$

$$(C_c/A_c) = (-2 \cdot a^2) \tag{4.7}$$

$$(F_c/A_c) = (a^4) \tag{4.8}$$

In a similar manner, an expression may be developed for a circular shaped plate subjected to a linear tapering pressure distribution as:

$$w = [(p_d) \cdot (1-(|x|/a)) \cdot (1-\nu^2)/(16 \cdot E \cdot t^3)] \cdot [(x^4 + (2 \cdot y^2 - 2 \cdot a^2) \cdot x^2 + (a^4 + y^4 - 2 \cdot a^2 \cdot y^2)] \tag{4.9}$$

Relating terms:

$$A_c = [(p_d) \cdot (1-(|x|/a)) \cdot (1-\nu^2)/(16 \cdot E \cdot t^3)] \tag{4.10}$$

$$(C_c/A_c) = (2 \cdot y^2 - 2 \cdot a^2) \tag{4.11}$$

$$(F_c/A_c) = (a^4 + y^4 - 2 \cdot a^2 \cdot y^2) \tag{4.12}$$

An examination of Equations 4.6 to 4.12 reveal that at the point of maximum deformation (i.e., x = y = 0), the (C_c/A_c) and (F_c/A_c) terms are equivalent. However, at the point of maximum deformation, w_{max}, the term (A_c) differs by a ratio of 8:1 (anticlinal-uniform to circular-linear). Thus, the anticlinal-uniform solution would predict w_{max} 8 times larger than the circular-linear tapering solution for equivalent borehole pressures and geologic formation properties. Clearly, this range of predicted deformations is too wide for reliable field predictions.

Consequently, the loading case finally selected for pneumatic fracturing was the circular plate subjected to a linear tapering pressure distribution. This selection was based on three premises. First, field data have consistently shown that the pattern of surface heave is generally circular shaped, not anticlinal. Second, both field pressure measurements and other analytical studies have confirmed that the pressure in a fracture reduces with increasing radius. This behavior is due to a combination of fluid leak-off into the formation and fluid friction losses within the fracture.

A final premise for selecting the circular-linear pressure model is it yields elastic properties which are consistent with those reported in the literature. This agreement is apparent in Table 4.2 which provides values of the elastic modulus back-calculated for both the anticlinal-uniform case and the circular-linear case. As indicated, the elastic modulus values calculated for the circular-linear case are most representative of those found in published literature (e.g., AASHTO, 1996 or U.S. Navy, 1982), whereas the values for the anticlinal-uniform case seem to greatly overpredict published values. Suggested values of the modulus of elasticity and Poisson's ratio for incorporation into the design model are presented in Appendix D.

Now that the circular-linear tapering solution has been selected as being the most representative of ground deformations resulting from pneumatic fracturing, this case can be adapted to a more practical form. Beginning with Equation 4.9, the "y-term" can be factored out considering the radial symmetry of the problem. In addition, the equation nomenclature can be changed into more familiar geotechnical terms. This yields the following equation:

$$w = [P_x]\cdot[(1-\nu^2)]\cdot[(x^4 - 2\cdot R^2\cdot x^2 + R^4)]/[16\cdot E\cdot z^3] \qquad (4.13)$$

Table 4.2 Back-Calculated Values of the Modulus of Elasticity.

Site Location	Geology Type	Dry Unit Weight (ft) $\gamma_{overburden}$	Average Depth (ft) t	Max. Heave (ft) w_{max}	Average Heave Radius (ft) R	Drivin Press. psi p_d	Assumed Poisson's Ratio ν	Extreme Calculated Values of the Modulus of Elasticity, E (psi)	
								Uniform Pressure Anticlinal Plan E_{U-A}	Linear Pressure Circular Plan E_{L-C}
Hillsborough (Phase II - 2-1)	Siltstone	140	10.1	0.0305	31.5	11.18	0.25	164204	20525
Hillsborough (Phase II - 2-2)	Siltstone	140	12.3	0.0204	30.8	13.04	0.25	144921	18115
Hillsborough (Phase II - 2-3)	Siltstone	140	14.2	0.0247	29.8	6.194	0.25	32378	4047
Flemington	Siltstone	140	15.6	0.0208	19.3	14.83	0.25	12217	1527
Marcus Hook (FW3-Inj.#1)	Clayey Silt, Silty Clay (CL-ML)	105	6	0.0498	15.8	7.625	0.3	20100	2513
Marcus Hook (FW3-Inj.#3)	Clayey Silt, Silty Clay (CL-ML)	105	6	0.0399	15.1	13.63	0.3	37396	4675
Marcus Hook (FW3-Inj.#4)	Clayey Silt, Silty Clay (CL-ML)	105	6	0.0481	16.4	14.63	0.3	46332	5792
Marcus Hook (FW3-Inj.#5)	Clayey Silt, Silty Clay (CL-ML)	105	4	0.0619	14.4	11.08	0.3	54734	6842
Marcus Hook (FW1-Inj.#3)	Clayey Silt, Silty Clay (CL-ML)	105	6.2	0.0261	8.8	15.48	0.3	6790	849
Marcus Hook (FW2-Inj.#5)	Clayey Silt, Silty Clay (CL-ML)	105	4	0.0356	9.6	13.08	0.3	22191	2774
Oklahoma (SWT5,Inj.#1)	Silty Clay (CL)	105	8	0.0401	20.5	25.17	0.3	98500	12313
Oklahoma (SWT6,Inj.#4)	Silty Clay (CL)	105	19	0.013	34.7	116.1	0.3	859268	107409
Frelinghuysen (Fig.A13)	Sandy Silt and Clay(CL,ML)	105	6	0.007	5.7	10.63	0.3	3375	422
Frelinghuysen (Fig.A14)	Sandy Silt and Clay(CL,ML)	105	8.3	0.0179	12.2	11.95	0.3	11767	1471
Frelinghuysen (Fig.A17)	Sandy Silt and Clay(CL,ML)	105	8.6	0.0297	12.1	10.73	0.3	5539	692
Frelinghuysen (Fig.A21)	Sandy Silt and Clay(CL,ML)	105	9	0.016	14.3	9.938	0.3	26912	3364
Frelinghuysen (Fig.A22)	Sandy Silt and Clay(CL,ML)	105	9	0.0131	12.1	8.138	0.3	8311	1039
Frelinghuysen (Fig.A23)	Sandy Silt and Clay(CL,ML)	105	6	0.0221	12.3	8.125	0.3	17726	2216
Frelinghuysen (Fig.A24)	Sandy Silt and Clay(CL,ML)	105	8.3	0.0116	11.5	10.95	0.3	13135	1642

where w is the magnitude of surface deformation; P_x is the fracture maintenance pressure at a distance x from the injection point (i.e., $[P_x = p_d \cdot (1-(|x|/R))]$); R is the fracture radius; x is the variable distance from the injection point towards the outer extremes of the surface deformation; ν is Poisson's ratio; and E is the modulus of elasticity. Another useful relationship which can be applied is for the maximum surface displacement, w_{max}:

$$w_{max} = [P_x] \cdot [(1-\nu^2)] \cdot [R^4]/[16 \cdot E \cdot z^3] \qquad (4.14)$$

It is noted that the fracture maintenance pressure, P_x, is a function of the driving pressure, p_d, which deforms the geologic formation. In the laccolith models presented previously in Chapter 3, the overburden stress, $z \cdot \gamma_{overburden}$, was subtracted from the driving pressure of the magma. However, analysis of pneumatic fracturing field data indicates that the overburden stress should not be deducted from the driving pressure, i.e. use the full value of p_d. The following explanation is offered for this behavior. The magnitude of the pressure required to breakdown the formation is typically at least five times greater than the pressure required to maintain the fracture in an open state. Apparently, after the formation is broken and lifted, it develops a certain degree of self-support, probably due to arching effects. Therefore, once equilibrium is established, the action of the driving pressure is more to deform the formation rather than to sustain the weight of overburden.

To validate the proposed model, a series of comparative plots were developed. The plots compare: (1) the actual measured ground surface deformation in the field; (2) the predicted ground surface deformation using the model Equation 4.13; and (3) the "averaged" ground surface deformation computed from the site-specific equations

presented in Table 4.1. A typical comparative plot is presented in Figure 4.5, which depicts the same deformed ground surface shown previously in Figure 4.2. Additional comparative plots for the sites used to develop the model are contained in Appendix A.

A review of the comparative plots shows the deformed surface predicted by the model equation, Equation 4.13, is in reasonable agreement with the measured field data for deformations greater than about 0.25 inches. In general, the middle portion of the curve in the vicinity of the injection point showed better agreement than at the extremities. However, for smaller deformations (i.e., $w < 0.25$ in.), the model deviates significantly from the measured field deformation curves. This is partly attributed to limitations of the field instrumentation systems, which can not actually record small ground movements. Therefore, comparison with the predictive model equation may be less reliable.

A review of the plots also indicates reasonable agreement between the measured field deformations and the averaged site equations from Table 4.1, often providing a better match than the model equation. This is particularly true for the deeper fractures where the model equation showed the greatest deviations. This result was expected since these equations were regressed directly from site-specific field data. The applicability of the regressed equations is limited, however, since they are only valid for a narrow range of fracture geometries (i.e., radius and depth). Nevertheless, this comparison confirms that a pilot test performed at an actual site within the fracture zone would be the best predictive tool. In lieu of a pilot test, it is clear that the model equation still provides reasonable predictions of ground deformation behavior.

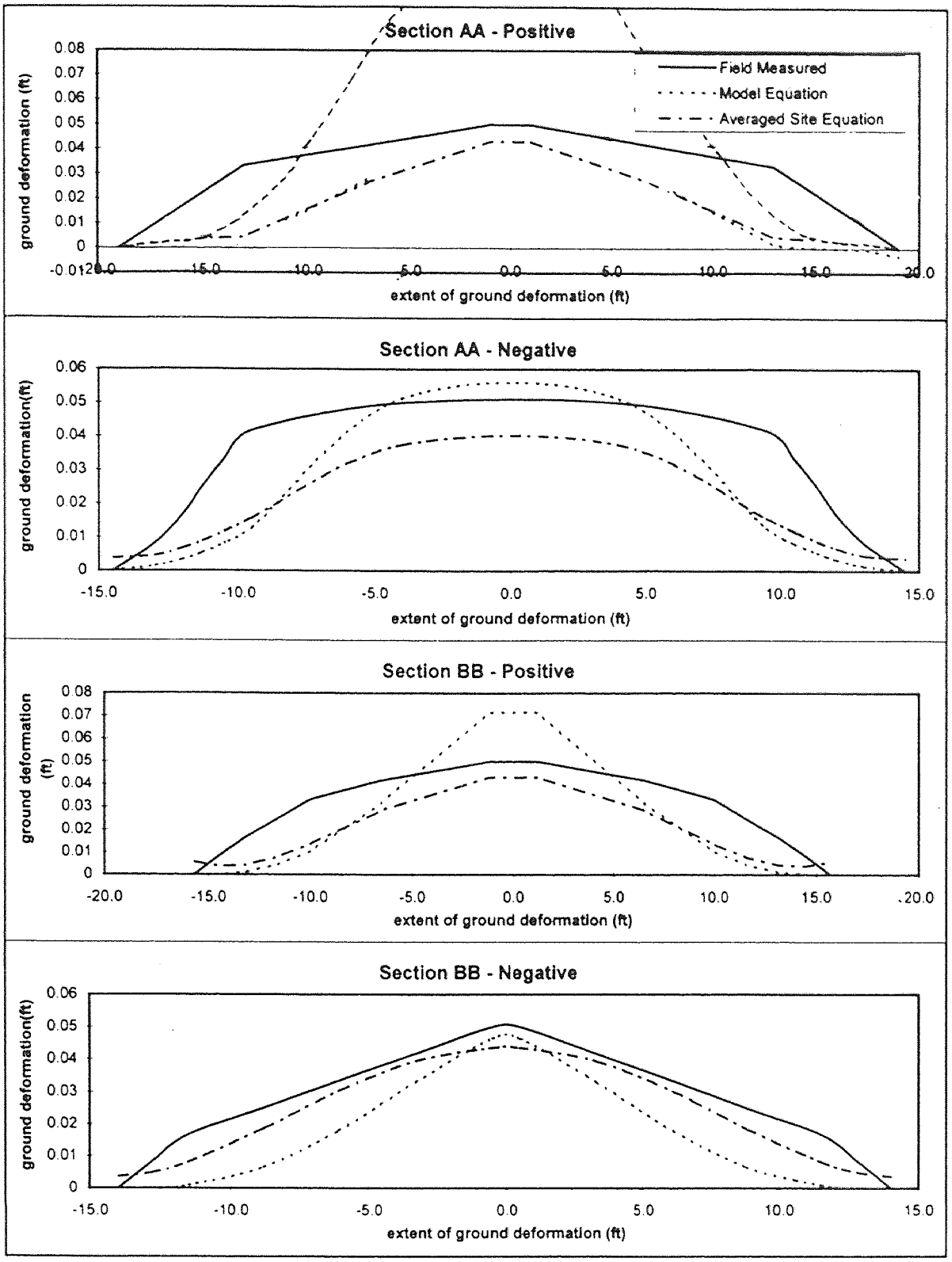

Figure 4.5 Comparative Plots of Ground Deformation Curves for the Site Presented in Figure 4.2 with the Proposed Model Equation Superimposed.

4.3 Adapting the Model to Consider Overlying Structures

Now that an approach for determining the curvature of the ground surface resulting from pneumatic fracturing has been established, the next step is to investigate the response of overlying structure to the ground movement. One approach is to represent the structure as another geologic layer which is superimposed on the actual geologic formation. This can be accomplished by adapting Equations 3.25 to 3.28 (Pollard and Johnson, 1973) for analyzing multiple layers of overburden above a forming laccolith. The basic concept is to combine layers of differing thickness and elasticity into an equivalent unit which resists the applied load from pneumatic fracturing. This approach is similar in concept to the analysis of a transformed composite beam section (or the "flitch plate" problem), which has been thoroughly studied in structural engineering. The basic equation which was previously presented in Chapter 3 is reintroduced here:

$$D_e = \sum (E_i \cdot t_i^3)/[12 \cdot (1-\nu_i^2)], \text{ from } i=1 \text{ to } n \qquad (4.15)$$

where D_e is the effective flexural rigidity of the combined layers (i.e., geologic formation and structure); E_i is the modulus of elasticity of each layer; t_i is the thickness of each layer, and ν_i is the Poisson's ratio for each layer.

Application of Equation 4.15 requires that the structure be transformed into an equivalent geologic layer. This approach is obviously simplistic and does not consider the complexity of different structure types or the soil-structure interaction, which can have a profound effect on the final form of the deformed surface. In addition, the depth of fracture determines the amount of influence that an overlying structure will have (or will

not have) as a result of pneumatic fracturing. These issues will now discussed with the intent of adapting Equation 4.15 for use in predicting the response of different structure types at varying pneumatic injection depths.

4.3.1 Effects of Fracture Depth

Fracture depth plays an important role in determining whether or not the structure has enough influence to be considered a resisting element. Limited field observations involving cases of fracturing beneath structures reveal that the deformed surface differs to some degree depending on the depth of injection and the type of geologic formation. Presumably, the influence zone of the pneumatic injection is analogous to the standard concept of stress distribution (e.g., Newmark, 1942 or Schmertmann, et.al., 1978). That is, as the injections progress to deeper depths, the magnitude of the ground deformation decreases while the overall lateral area of influence increases.

The principal of stress distribution is also useful in estimating the fracture depth below which the surface structure will have minimal influence on fracture propagation. For example, in settlement computations, the lower limit of influence is commonly considered to be the point at which the distributed stress is 10% of the applied surface pressure. This concept is illustrated in Figure 4.6 which gives pressure bulbs for square and continuous footings. Inspection of Figure 4.6 shows that the 10% criteria is reached at a depth ranging from $2 \cdot B_F$ to $6 \cdot B_F$ depending on the footing type (where B_F represents the footing width). At depths greater than this, the applied surface load is considered to have a negligible effect.

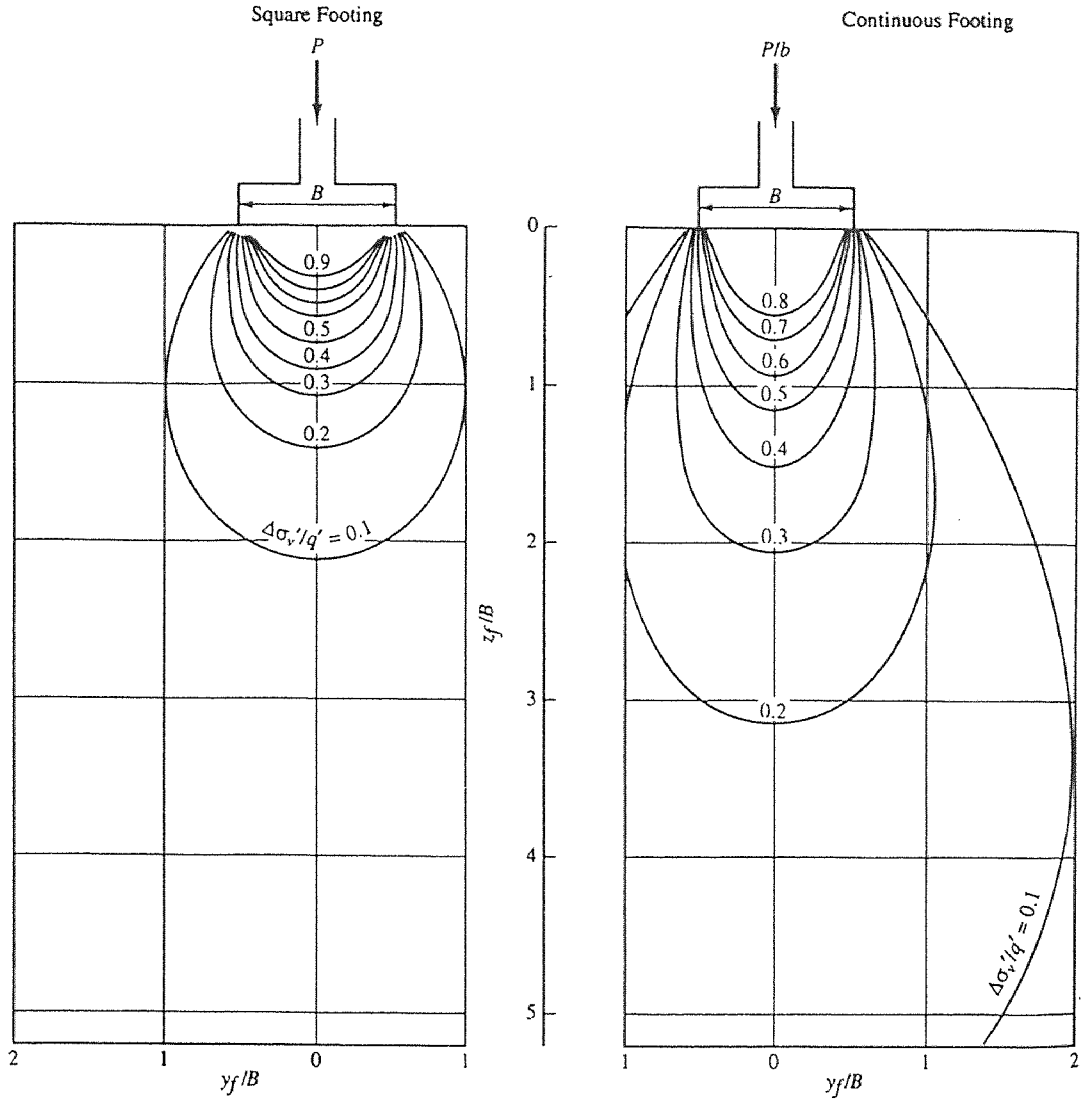

Figure 4.6 Pressure Bulbs Based on Newmark's Solution of Boussinesq's Method for Square and Continuous Footings (modified after Coduto, 1994).

A similar depth criteria for stress influence is available from the design of tunnels and buried conduits. In this case, the concept is known as "arching." Széchy (1973) describes the mechanics of arching as the action of an applied stress being redistributed as

smaller stresses over a larger area. At some point the deflections and bending stresses in the geologic formation have decrease significantly. That is, at some depth the stresses developed over a tunnel opening become constant since the geologic formation is now acting as an arch. The average depth limit below which arching may be expected is $3 \cdot B_T$, where B_T is the width of the tunnel opening.

In summary, a review of the theory of stress distribution has been used to suggest a depth limit of structure influence on pneumatic fracturing injections. This will be useful in defining various design cases later in Chapter 6. The effect of different structure types on ground deformations will now be reviewed.

4.3.2 Soil-Structure Interaction

Soil-structure interaction is primarily a function of the rigidity of the structure, as well as the engineering properties of the structural materials and the geologic formation. In the extreme, structures are classified as either rigid or flexible, although in reality most structures tend to behave somewhere between these two extremes. In the context of this study, "rigid" structures are those containing mat foundations and/or load-bearing masonry walls, and "flexible" structures are those having steel and/or wood frames. Figure 4.7 illustrates how the pressure distribution differs beneath rigid and flexible mat foundations which is useful in understanding the response of different structure types to loads imposed by pneumatic fracturing.

When considering rigid structures, the potential for damage from pneumatic injections should generally be low due to the ability of the structure to redistribute applied loads without large differential movements. The exception to this is the potential for

hogging (discussed in Section 3.3) which may occur if fracturing is conducted close to masonry walls. In general, it should be possible to fracture beneath rigid structures at shallow depths without causing adverse differential movements. Likewise, the magnitude of the foundation movements will be smaller.

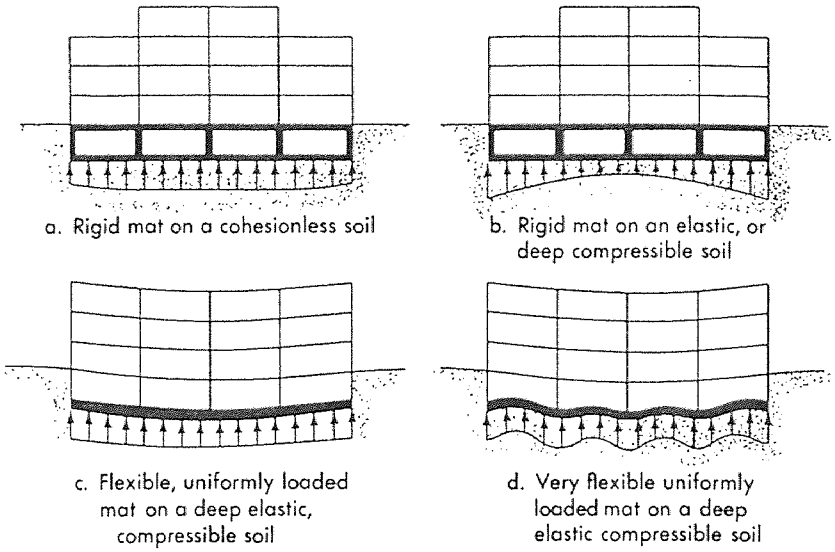

Figure 4.7 Pressure Distribution on Mat Foundations (after Sowers, 1962).

Flexible structures will likely be more prone to damage from pneumatic injections since they are less capable of redistributing applied loads. Individual sections of the building can move more or less independently resulting in greater differential movements. On the other hand, flexible structures can also tolerate greater deflections than rigid structures before they experience structural damage. However, architectural and cosmetic damage (e.g., cracked walls, doors sticking, and broken walls) occur at much smaller deflections and could be extensive in flexible structures.

Aside from the general structure type, there are other factors which will influence the surface deformation resulting from fracturing beneath a structure. For example, the massive loads imposed by masonry bearing walls or heavy steel columns onto individual foundations in the vicinity of the injection well will affect the geologic response. This is actually the concept of limital thickness by Gilbert (1877) previously described in Section 3.2: if the foundation pressure exceeds the force applied by the pneumatic injections, then no movement of the foundation will occur. Conversely, it is probable that the deformation of adjacent open areas will be magnified (or "ballooned") as the pressure reflects towards a region of lower ground stress. Underground obstructions (e.g., storage tanks) also have the potential to cause reflections of the injected pneumatic pressure. When fracturing adjacent to buried tanks, the ground may be expected to be both magnified and irregularly shaped.

CHAPTER 5

FIELD PILOT TEST - HIGHLAND PARK, NJ

An instrumented field test was performed beneath an actual contaminated industrial facility to obtain data on the dynamic response of the structure. The test was performed at the former Midland-Ross site located in Highland Park, New Jersey. The site is presently undergoing a remedial clean-up to extract volatile organic compounds (VOCs) which leaked into the subsurface as a result of past industrial activities. The site is located on New Jersey's Passaic (Brunswick) Formation which consists of fractured mudstone and shale. A detailed report on this field pilot test is available from the Hazardous Substance Management Research Center (HSMRC) at the New Jersey Institute of Technology in Newark, NJ, entitled *"Investigation of the Effects of Pneumatic Fracturing on Structures and Utilities,"* November 1996, by Dr. John R. Schuring, Michael C. Canino, Thomas M. Boland, and Dr. Ivan Nelson. This chapter is actually an abridgment of the full report, and the reader is directed to the complete report for further study.

5.1 Description of the Test Structure

The test structure is an abandoned industrial warehouse and light manufacturing facility which was built around 1930 according to the Middlesex County tax records. The structural frame consists of steel columns and beams with intermittent brick masonry shear walls. The building floor is concrete, with a six-inch thickness in the vicinity of the fracture well. It appears that the original structure was modified and expanded several times during its lifetime.

In general, measurement accuracy of the structural members and building dimensions were ±0.1 in. and ±0.01 ft, respectively. Based on the results of the site survey, a floor plan of the building was developed for the fracture well vicinity as shown in Figure 5.1. A coordinate system has been implemented to show the exact location of all of the structural elements. The plan also indicates the location of an underground vault which is located approximately 16 ft from the fracture well.

The structural steel members were identified by comparing the field measurements with data from steel handbooks published around the time of the original construction. In some cases, precise member identification was not possible, therefore the section properties were estimated sufficiently close for the purposes of this analysis. A framing plan showing the assumed steel sections for the structural analysis is shown in Figure 5.2.

The depth and size of the foundation footings has been assumed based on standard engineering practice, since the actual dimensions were unattainable. Based upon the design loads and the local geology, it has been assumed that the footings are 6 ft by 6 ft square and are located at a depth of 5 ft below the top of the floor slab.

As the original design calculations were not available, the design loads were estimated based upon the building survey and contemporary (1930's) structural practice. For the purposes of the structural evaluation, the following design loads were assumed:

- Dead Load = 14 psf (for roof load)
- Snow Load = 30 psf
- Wind Load = 20 psf

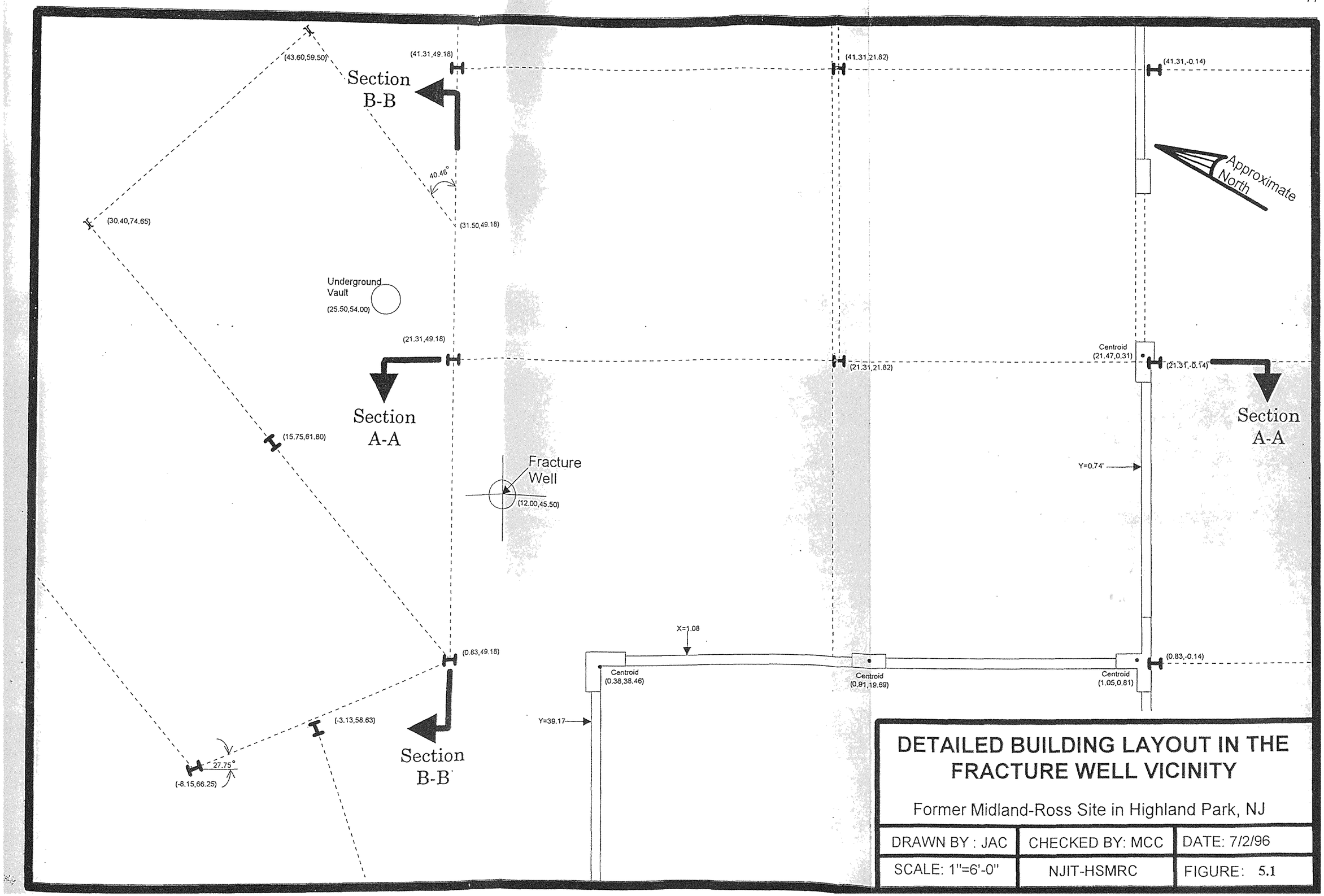

DETAILED BUILDING LAYOUT IN THE FRACTURE WELL VICINITY

Former Midland-Ross Site in Highland Park, NJ

DRAWN BY : JAC	CHECKED BY: MCC	DATE: 7/2/96
SCALE: 1"=6'-0"	NJIT-HSMRC	FIGURE: 5.1

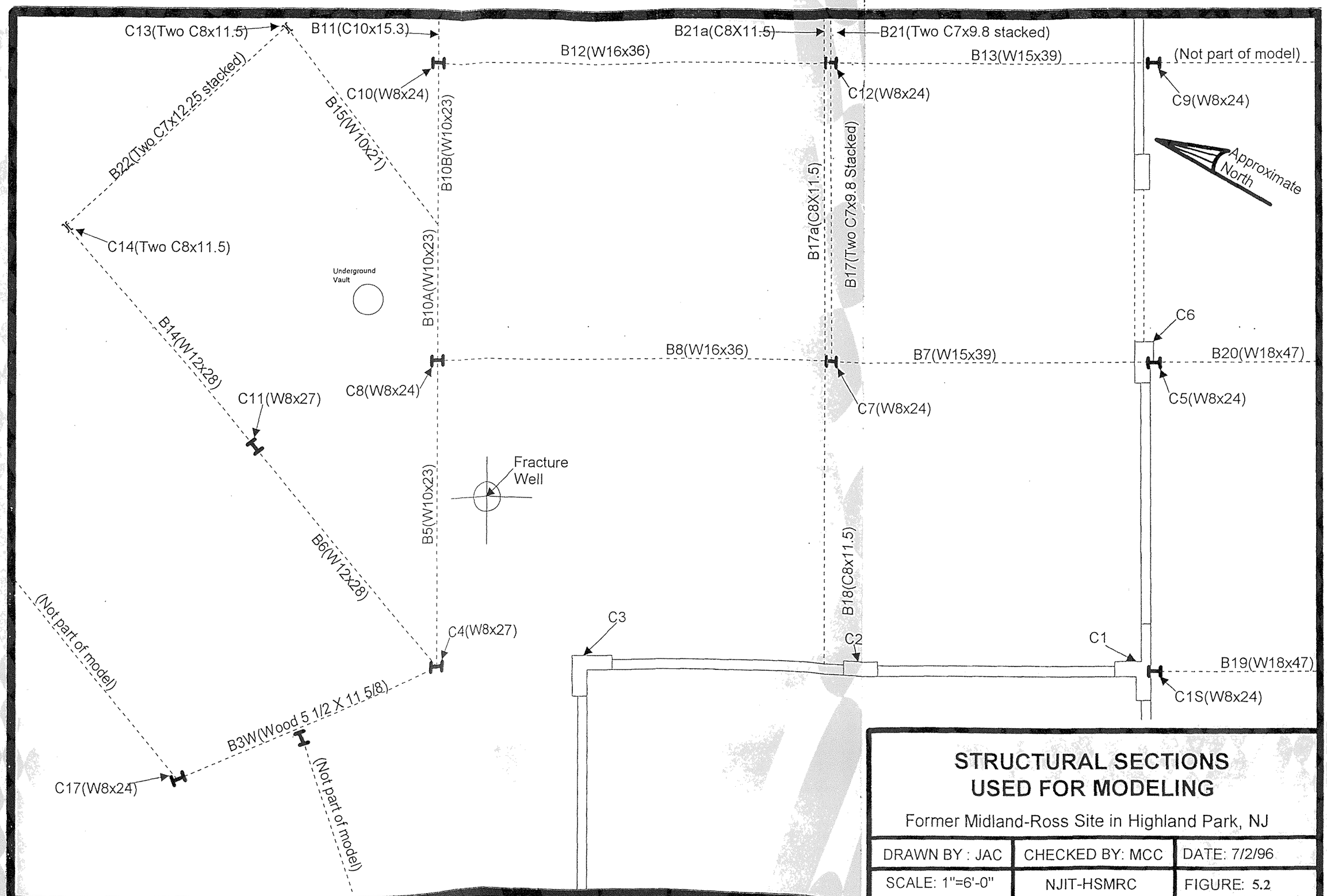

STRUCTURAL SECTIONS USED FOR MODELING

Former Midland-Ross Site in Highland Park, NJ

DRAWN BY : JAC	CHECKED BY: MCC	DATE: 7/2/96
SCALE: 1"=6'-0"	NJIT-HSMRC	FIGURE: 5.2

5.2 Field Test Layout

In the present study, surface heave and structural movements were monitored during each of the five pneumatic injections using both electronic and optical instrumentation systems. In particular, strain gages, tiltmeters, linear variable displacement transducers (LVDTs) and optical engineering levels with graduated heave rods were used for the test. A discussion of the concept and function of each of these instrumentation systems is contained in Appendix B. Locations of all of the instruments in relation to the fracture well are shown in Figure 5.3.

Electronic strain gages were used to measure the stress levels in the steel members during injection and to provide qualitative visualization of the overall structural deformation. For the present study, a total of 18 electronic strain gages were installed (as nine pairs) on the structural steel columns and beams in the vicinity of the injection well. The gages used were single grid, 120 ohm, bonded foil resistance gages manufactured by Measurements Group, Inc. of Raleigh, NC (Part No. CEA-06-500UW-120). The gages were bonded to the surfaces of the steel members in accordance with the manufacturers recommendations, and each gage was checked electronically for the proper response after installation. These gages had a gage factor of 2.085, an accuracy on the order of ±5 microstrain, and were self-temperature compensated for steel (based on the specific thermal expansion coefficient of steel). Data from the gages were recorded by the data acquisition system and later downloaded to a microcomputer for interpretation. For each fracture injection, the gages were monitored for a 3 to 5 minute period using a sampling rate of 2 times per second. Data were later analyzed using Microsoft Excel for use in a stress-strain analysis of the structure.

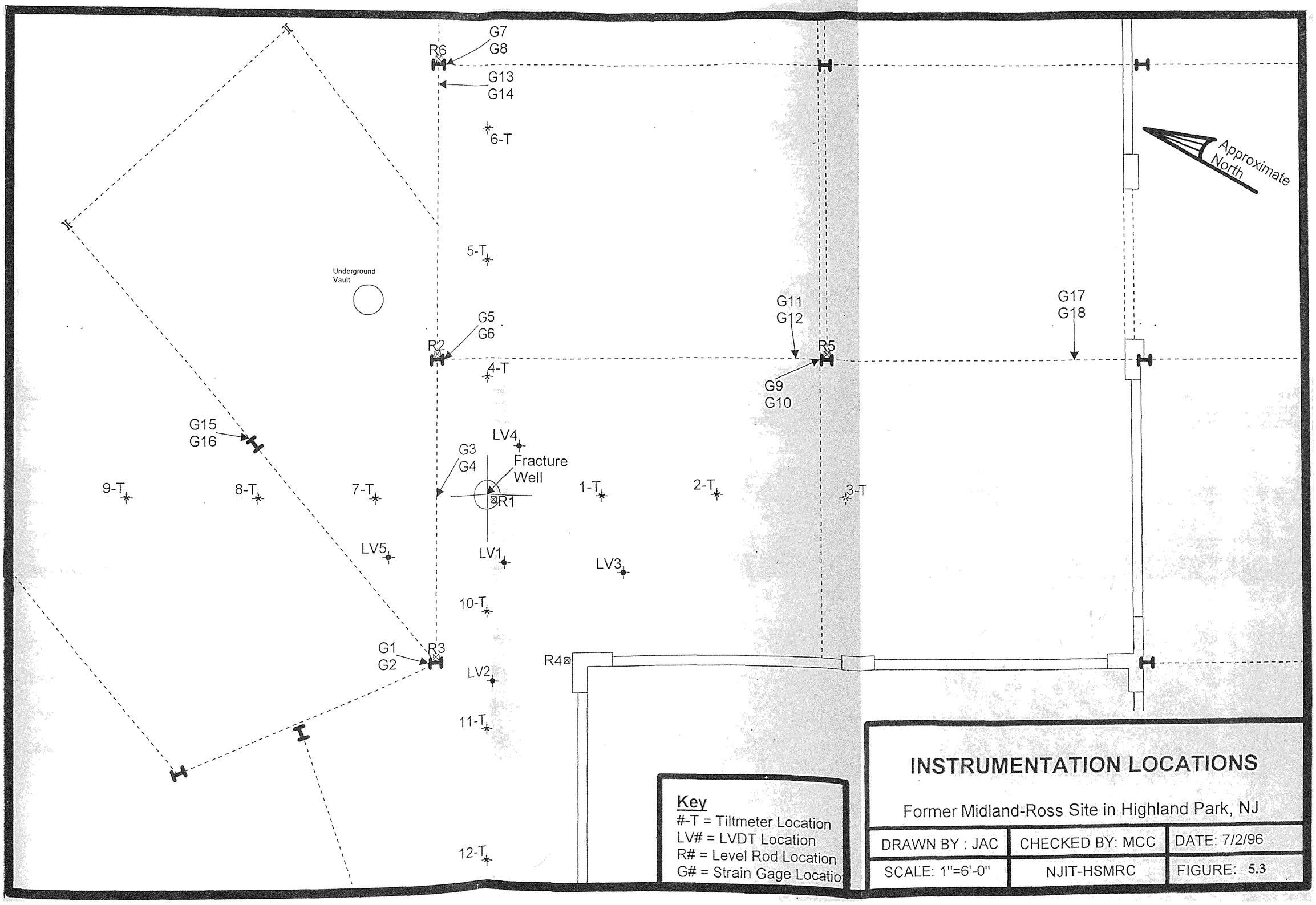
G7
G8
R6
G13
G14
6-T
Approximate North
5-T
Underground Vault
G11
G12
G17
G18
G5
G6
R2
R5
4-T
G9
G10
G15
G16
LV4
G3
G4
Fracture Well
9-T
8-T
7-T
R1
1-T
2-T
3-T
LV5
LV1
LV3
10-T
G1
G2
R3
R4
LV2
11-T
12-T
Key
#-T = Tiltmeter Location
LV# = LVDT Location
R# = Level Rod Location
G# = Strain Gage Locatio
INSTRUMENTATION LOCATIONS
Former Midland-Ross Site in Highland Park, NJ
DRAWN BY : JAC
CHECKED BY: MCC
DATE: 7/2/96
SCALE: 1"=6'-0"
NJIT-HSMRC
FIGURE: 5.3

Highly sensitive electronic tiltmeters were used to measure the angular deflection of the concrete slab around the fracture well during the fracturing event. For the current study, twelve separate tiltmeters were placed on the floor slab in a radiating pattern around the fracture well. Sensors were positioned 8-feet, 16-feet, and 25-feet from the injection point in the four orthogonal directions. The tiltmeters used for this project are described in Appendix B. The same data acquisition system and sampling intervals used for the strain gages were employed for the tiltmeters. Downloaded data were later analyzed with proprietary software from AGI and using Golden Software's Surfer program, to create contour maps of the surface heave.

Linear variable displacement transducers (LVDTs) were used to calibrate the tiltmeter data by providing the actual vertical displacement of the concrete slab during each of the five injections. For the present study, five LVDTs were installed in a radiating pattern around the fracture well at distances ranging from 4 to 13 feet. The same data acquisition system and sampling intervals used for the strain gages were also employed for the LVDTs. Downloaded data were later analyzed using Microsoft Excel, to create graphs of the varying vertical displacements at each LVDT location.

For the present study, six optical engineering levels with graduated heave rods were used to monitor the concrete slab and structural column movements. These data were used to complement data from the strain gages and the LVDTs. Four levels were targeted at the base of structural steel columns, one was sighted next to the injection well, and the last was sighted on a structural masonry wall. The levels were read by six different observers from positions outside of the presumed influence area of the fracture.

5.3 Fracture Injections

The pneumatic fracturing operations for this project were performed by Accutech Remedial Systems using their PFE^{SM} injection trailer. The injection system was previously described in Chapter 2. Successful fracturing is dependent on two parameters which are adjusted according to the site geology and fracture injection depth. These are the injection pressure and injection flow rate. A typical fracture injection sequence for this study involved the following steps: (1) the HQ injector is placed at the depth interval to be fractured; (2) a 2.5-ft interval was sealed off by inflating the flexible packers on either side of the HQ injector; (3) the monitoring instrumentation was activated to begin sampling; (4) a surge of pressurized air from the tanks was applied to the packed-off interval at a predetermined setting for approximately 15 seconds; and (5) the packers were depressurized, the HQ injector was moved to the next depth, and the process was repeated. The entire cycle for each injection was approximately 30 minutes in duration, which included downloading data and resetting the monitoring instruments.

Five pneumatic fracture injections were made beneath the building structure as part of this study. Fracturing was performed on August 3, 1995 at Injection Well No.1B. The five injections in Fracture Well No. 1B were made over a depth interval of 11.5 ft to 24 ft.

Table 5.1 provides a summary of the operating parameters as recorded by Accutech Remedial Systems. It is noted that the structural analysis in this study focused on the first injection (11.5 ft to 14 ft). The other fracture injections were at deeper intervals and provided similar results, but as expected, caused smaller structural movements. As indicated in the table, pressure readings were not obtained in the borehole during fracturing due to a transducer malfunction.

Table 5.1 Pneumatic Fracturing Injection Parameters (Accutech Remedial Systems).

Injection				Pressure		Packer	Bottle Pressure			Inj.	Re-
Depth (feet)	Well No.	Inj. No.	Time of Day	Gage #1	Gage #2	Pressure	Initial	Final	Diff.	Period (sec.)	marks
11.5-14.0	1B	1	2:40	90	220	390	2780	2420	2059	15	TNR
14.0-16.5	1B	2	3:05	90	240	400	2600	2280	1830	15	TNR
16.5-19.0	1B	3	3:28	90	260	430	2460	2150	1773	15	TNR
19.0-21.5	1B	4	4:10	90	320	455	2410	2080	1888	15	TNR
21.5-24.0	1B	5	4:36	92	350	525	2280	1950	1888	15	TNR
Note: TNR = Transducer not reading.											

5.4 Field Test Results

This section presents test results for the instrumented field tests conducted on the Highland Park structure. Included are the ground surface heave and structure heave results (5.4.1), and the strain measurement results (5.4.2).

5.4.1 Ground Surface Heave and Structure Heave

The ground surface heave and structure heave were monitored using three independent systems: optical engineering levels, LVDTs, and tiltmeters. Results for the engineering levels are summarized in Table 5.2 which shows the maximum and residual movements during each fracture injection. The largest magnitude of heave observed during the test was 0.625 in. at Column C7 (see Figure 5.3 for exact location) during the first injection. Maximum residual magnitudes of 0.125 in. of heave were measured after Fracture Injections 1, 2, 3, and 4 at a total of five separate locations. A review of the data indicates that while recorded heave generally decreased with injection depth, increases were observed in some cases. This behavior was attributed to the fact that as the fractures progressed deeper, the injection pressure was increased. This clearly demonstrates the interaction between surface heave and injection pressure.

The LVDTs provided additional data on ground surface displacement around the fracture injection well. The values of maximum and residual heave recorded for each fracture injection have been summarized in Table 5.3, and the complete time-histories can be found in the report mentioned at the beginning of the chapter. These LVDT results correlated well with the tiltmeter data, thus increasing the confidence level for both instrumentation types. It is noted that LVDT L4 malfunctioned throughout the field tests, and some difficulties were experienced with data downloading during Fracture Injection No.3.

Table 5.2 Optical Engineering Level Readings.

Fracture No.1 (Injection Pressure = 220 psi)	Level Rods (reference Figure 5.3 for locations)					
	R1	R2	R3	R4	R5	R6
Maximum Heave (in.)	0.625	0.313	0.250	0.219	0.313	0.063
Residual Heave (in.)	0.125	0.125	0	0.063	0.063	0
Fracture No.2 (Injection Pressure = 240 psi)	Level Rods (reference Figure 5.3 for locations)					
	R1	R2	R3	R4	R5	R6
Maximum Heave (in.)	0.313	0.250	0.188	0.188	0.250	0.094
Residual Heave (in.)	0.063	0.125	0.063	0.063	0.031	0.031
Fracture No.3 (Injection Pressure = 260 psi)	Level Rods (reference Figure 5.3 for locations)					
	R1	R2	R3	R4	R5	R6
Maximum Heave (in.)	0.250	0.188	0.313	0.188	0.250	0.063
Residual Heave (in.)	0.063	0.063	0.063	0.063	0.125	0
Fracture No.4 (Injection Pressure = 320 psi)	Level Rods (reference Figure 5.3 for locations)					
	R1	R2	R3	R4	R5	R6
Maximum Heave (in.)	0.188*	0.313*	0.063	0.188	0.250	0.031
Residual Heave (in.)	0.063	0	0	0.063	0.125	0
Fracture No.5 (Injection Pressure = 340 psi)	Level Rods (reference Figure 5.3 for locations)					
	R1	R2	R3	R4	R5	R6
Maximum Heave (in.)	0	0.188	xxx	0.063	0.188	0
Residual Heave (in.)	0	0	xxx	0	0	0

xxx = means that the optical level moved as a result of the pneumatic injection.
* = negative values were observed after maximum heave was seen at the well as the fracture propagated to the level.

Table 5.3 Summary of LVDT Field Results.

Fracture No.1 (Injection Pressure = 220 psi)	LVDTs (reference Figure 5.3 for locations)				
	L1	L2	L3	L4	L5
Maximum Heave (in.)	0.203	0.098	0.123	xxx	0.154
Residual Heave (in.)	0.139	0.090	0.093	xxx	0.084
Fracture No.2 (Injection Pressure = 240 psi)	LVDTs (reference Figure 5.3 for locations)				
	L1	L2	L3	L4	L5
Maximum Heave (in.)	0.185	0.077	0.012	xxx	0.039
Residual Heave (in.)	IDR	IDR	IDR	xxx	IDR
Fracture No.3 (Injection Pressure = 260 psi)	LVDTs (reference Figure 5.3 for locations)				
	L1	L2	L3	L4	L5
Maximum Heave (in.)	0.093	0.062	0.071	xxx	0.185
Residual Heave (in.)	0.093	0.062	0.066	xxx	0.108
Fracture No.4 (Injection Pressure = 320 psi)	LVDTs (reference Figure 5.3 for locations)				
	L1	L2	L3	L4	L5
Maximum Heave (in.)	0.098	0.049	0.064	xxx	0.130
Residual Heave (in.)	0.071	0.047	0.051	xxx	0.048
Fracture No.5 (Injection Pressure = 340 psi)	LVDTs (reference Figure 5.3 for locations)				
	L1	L2	L3	L4	L5
Maximum Heave (in.)	0.744	0.031	0.042	xxx	0.077
Residual Heave (in.)	0.744	0.031	0.028	xxx	0.029

xxx = means that the LVDT malfunctioned during the pneumatic injection.
IDR = incomplete data record due to malfunction during data downloading.

The tiltmeters provided time histories of ground surface tilt during the injections. The tiltmeters were "zeroed" with LVDT and engineering level results in order to develop contour maps of ground surface heave. Contour maps for Fracture Injections 1, 2, 4, and 5 are shown in Figures 5.4, 5.5, 5.6, and 5.7, respectively. Tiltmeter data were not recorded during Fracture Injection No.3.

An examination of the heave contours reveals that they are asymmetric, and do not exhibit the near circular shape typically observed for fracture injections performed in unobstructed, open ground. This deviation is attributed to the influence of the structure and to reflections off the underground storage tank. For example, there was a massive masonry shear wall immediately north of the injection well which significantly suppressed

the surface heave for the shallower fracture injections. As expected, the influence of the deeper fracture injections was less. Also, in the area southwest of the fracture injection well, there is an underground storage tank which extends from 4 to 13 feet below the ground surface and is estimated to cover an area of 10 ft by 12 ft. The heave contours show that the fracture apparently reflected away from the tank area for the shallower fracture injections, but to a lesser degree for the deeper fractures. As the fracture injections progressed deeper, the heave contours became more nearly circular as the influence of the masonry wall and underground tank were diminished.

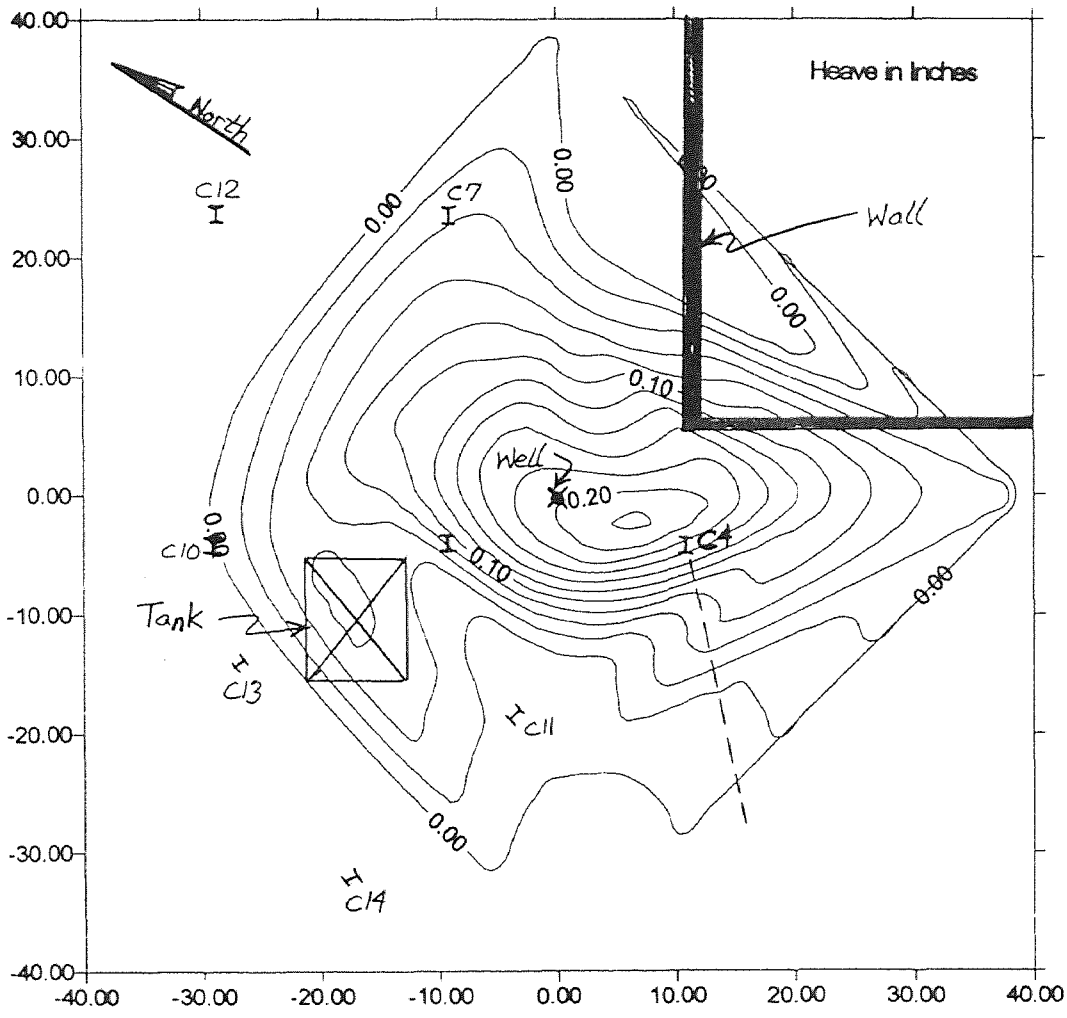

Figure 5.4 Heave Contour Plot for Fracture No.1 using Tiltmeter Results.

This trend suggests an apparent transition of building structural response with fracture depth. For shallow fracture injections, individual foundation elements tend to "steer" the fractures into open areas. As fracture depth increases, the increased weight and thickness of the overburden "masks" the effect of the individual structural elements and the structure behaves more as a single unit. Another factor in deeper fractures is increased "beam action" as the formation arches upwardly in response to the injection.

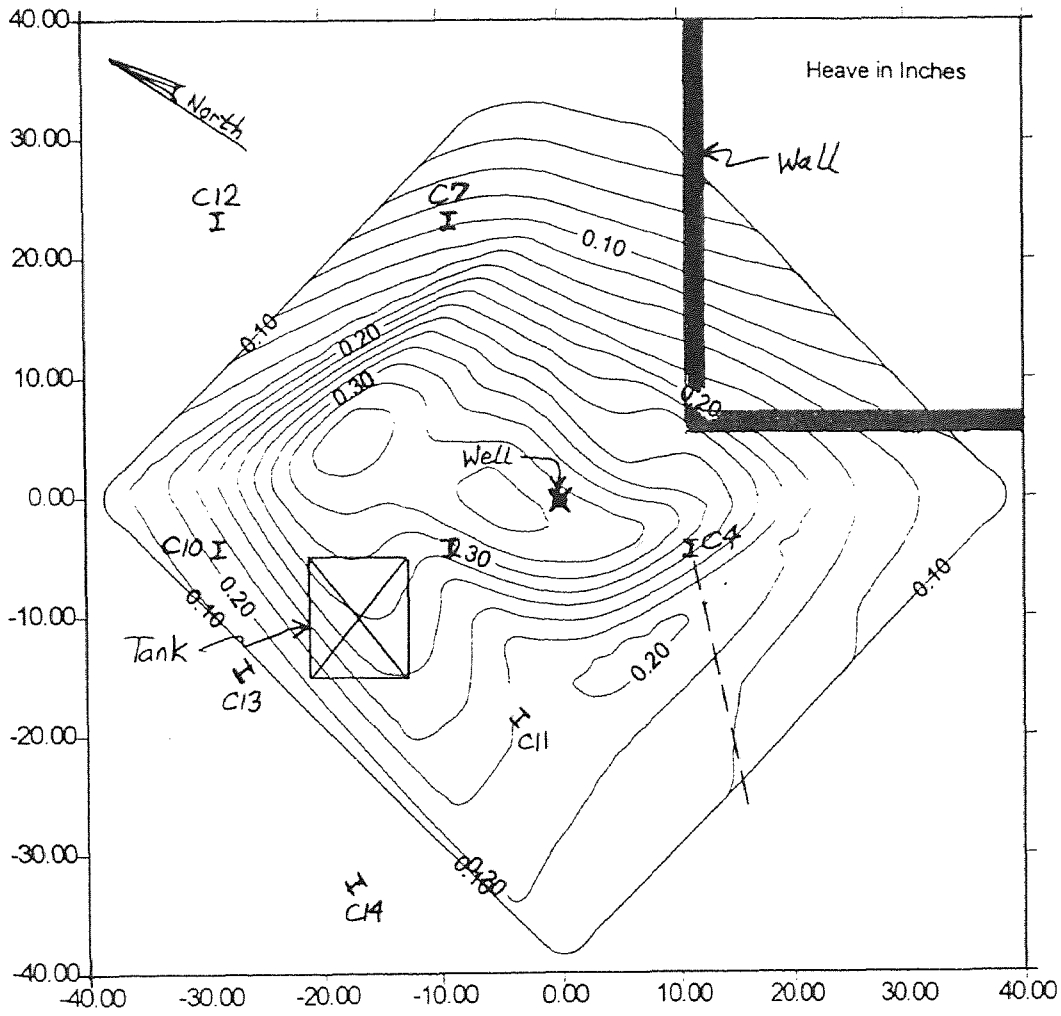

Figure 5.5 Heave Contour Plot for Fracture No.2 using Tiltmeter Results.

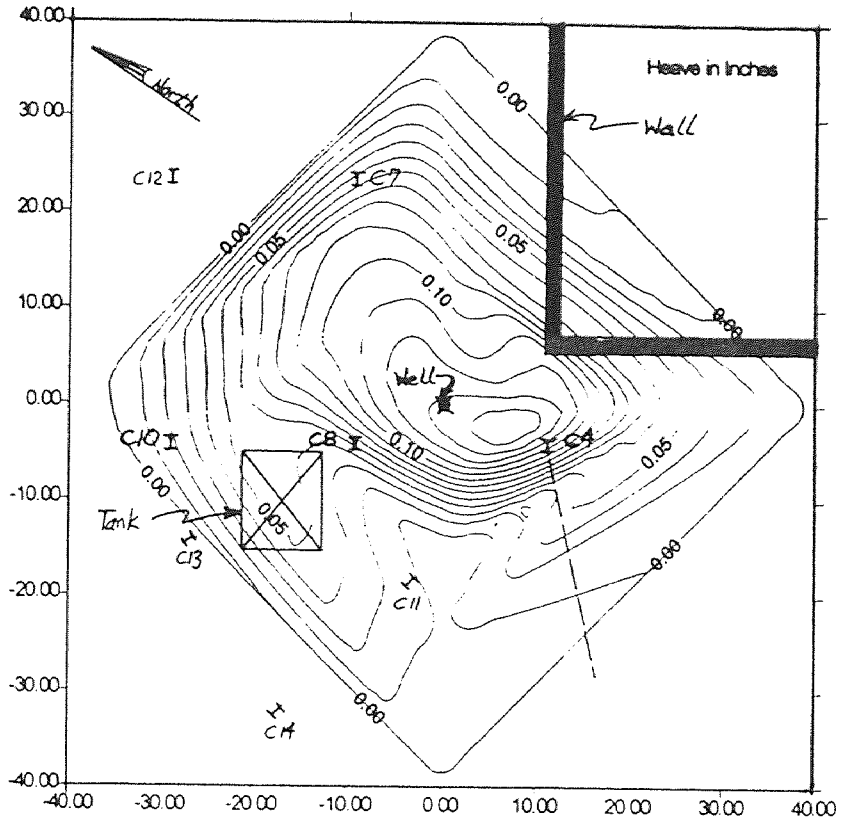

Figure 5.6 Heave Contour Plot for Fracture No.4 using Tiltmeter Results.

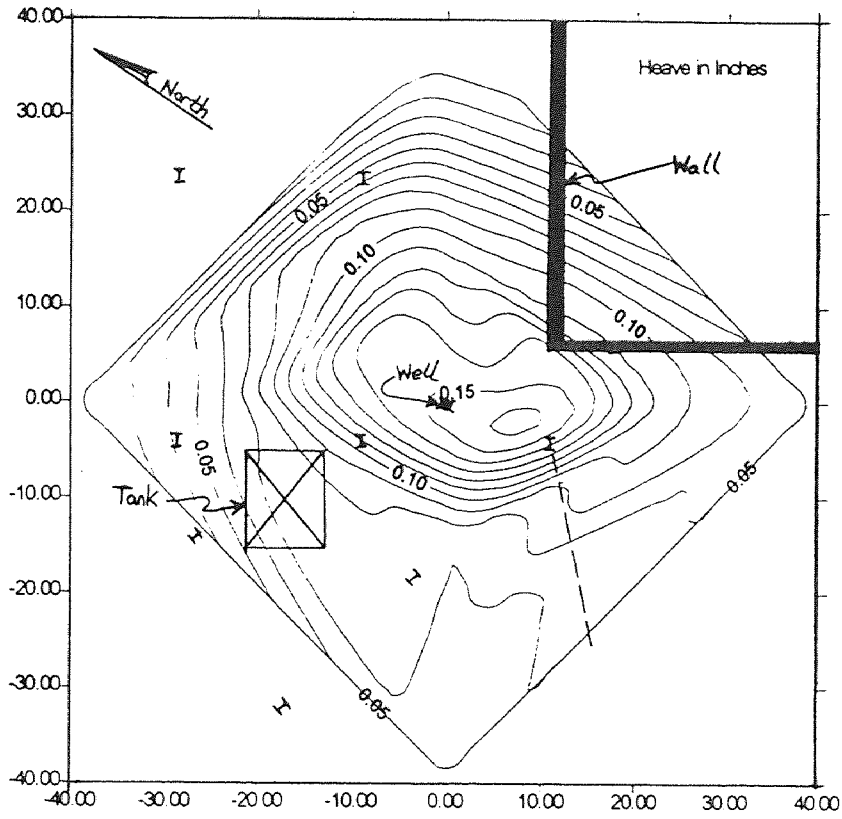

Figure 5.7 Heave Contour Plot for Fracture No.5 using Tiltmeter Results.

5.4.2 Strain Measurements

The 18 strain gages used for the 5 fracture injections provided a large body of strain results. Table 5.4 provides a summary of the maximum (tensile and compressive) and residual strains measured during the field test. A complete time-history for each gage can be found in the report mentioned in the introduction of this chapter. A detailed analysis of the strain data is presented in the next section. The following brief discussion is limited to general data trends and observations.

The "noise" level from the strain gages was estimated at ±5με. Strain gage noise is caused by a combination of random voltages in the recording channel and building vibrations. In view of the noise level, any values in Table 5.4 within the ±5με range should be considered as zero strain.

An inspection of the data reveals that the majority of the beams experienced considerably less strain than the columns. One exception was a beam which terminated into a masonry shear wall. The higher strain values here are attributed to the added fixity of the connection since the beam was "built in" to the wall. The other beams were connected to the columns with web connections, so they can be considered to be simply supported for practical purposes.

The strain observed in the columns correlated well with the tiltmeter heave plots in that maximum strain was observed at the column in the open bay areas. Conversely, the instrumented column farthest from the fracture injection well, along with the column located closest to the massive masonry shear wall, experienced the least amount of heave and strain.

Table 5.4 Summary of Strain Gage Results.

Strain Gage No.	Fracture No. 1			Fracture No. 2			Fracture No. 3			Fracture No. 4			Fracture No. 5		
	Max.ε (tens.)	Max.ε (comp.)	Resid. ε	Max.ε (tens.)	Max.ε (comp.)	Resid. ε	Max.ε (tens.)	Max.ε (comp.)	Resid. ε	Max.ε (tens.)	Max.ε (comp.)	Resid. ε	Max.ε (tens.)	Max.ε (comp.)	Resid. ε
G1	7.5	-7.0	2.0	IDR	IDR	IDR	2.5	-11.7	0.0	5.0	-7.9	3.0	4.5	-4.4	1.0
G2	4.1	-36.8	-10.0	IDR	IDR	IDR	8.6	-24.8	-4.0	2.8	-22.0	0.5	2.2	-9.5	-1.0
G3	6.0	-3.4	1.0	IDR	IDR	IDR	3.3	-4.3	1.0	3.8	-3.8	2.0	4.5	-1.4	2.0
G4	5.4	-5.8	1.0	IDR	IDR	IDR	5.1	-3.8	2.0	4.9	-2.6	2.0	4.4	-2.1	2.0
G5	4.0	-53.0	-13.0	IDR	IDR	IDR	2.0	-33.1	-11.0	0.9	-33.9	-5.0	2.3	-23.5	-1.0
G6	23.0	-16.0	1.0	IDR	IDR	IDR	10.9	-4.4	1.0	13.5	-0.7	3.0	7.6	-1.3	2.0
G7	10.0	-23.9	-3.0	IDR	IDR	IDR	1.3	-22.2	-6.0	4.4	-9.2	-5.0	0.7	-6.4	-3.0
G8	26.0	-6.2	0.0	IDR	IDR	IDR	15.7	-3.1	2.0	13.4	-5.4	-4.0	10.7	-3.9	-0.5
G9	18.5	-32.3	9.0	IDR	IDR	IDR	4.0	-31.8	-17.0	2.6	-24.3	-3.0	5.5	-26.1	2.0
G10	23.6	-32.8	15.0	IDR	IDR	IDR	3.6	-36.2	-20.0	2.7	-29.6	-6.5	3.0	-48.7	-2.0
G11	8.7	-12.4	0.0	IDR	IDR	IDR	5.5	-3.0	1.0	4.6	-6.0	-4.5	5.6	-5.5	-1.0
G12	8.5	-11.0	0.0	IDR	IDR	IDR	5.5	-3.0	1.0	0.5	-10.4	-7.0	10.1	-4.7	3.0
G13	12.4	-11.0	1.0	IDR	IDR	IDR	6.3	-3.5	1.0	18.3	-14.6	8.0	4.9	-7.5	1.0
G14	11.0	-13.7	0.0	IDR	IDR	IDR	11.4	-2.9	2.0	17.0	-21.1	0.0	3.2	-12.0	-2.0
G15	39.7	-7.6	8.0	IDR	IDR	IDR	IDR	IDR	IDR	49.2	-15.3	10.0	7.9	-8.0	-1.5
G16	82.1	-8.5	20.0	IDR	IDR	IDR	IDR	IDR	IDR	78.5	-7.8	24.0	20.5	-5.6	2.0
G17	36.1	-6.9	8.0	IDR	IDR	IDR	IDR	IDR	IDR	35.9	-29.8	6.0	10.8	-4.4	0.5
G18	16.9	-7.4	1.0	IDR	IDR	IDR	IDR	IDR	IDR	33.8	-23.8	2.0	14.9	-1.7	4.0

NOTES: 1. ε = strain.
2. Max. = maximum; Resid. = residual; tens. = tensile; and comp. = compressive.
3. tensile strain is represented by positive numbers.
4. compressive strain is represented by negative numbers.
5. IDR = incomplete data record due to malfunction during data downloading.

Some other observed trends in the strain data are worth noting. As the fracture sequence progressed deeper, the magnitude of strain tended to decrease. Also, the residual strain readings in the beams were nearly zero, while the residual strains in the columns ranged up to 63.6% of the maximum readings. Further interpretation of the strain is presented in Section 5.5, "Structural Response and Analysis."

5.5 Structural Response and Analysis

Using the field test results, a structural analysis involving the key steel members of the building frame has been performed. The objective was to compare the stresses induced by the fracture injections with the original design stresses of the building.

5.5.1 Stress-Strain Analysis

A stress-strain analysis has been performed for Fracture Injection No.1 using data obtained from 18 electronic strain gages installed on the steel frame, and complemented by selected LVDT, tiltmeter, and engineering level data. Refer back to Figures 5.1, 5.2, and 5.3 for detailed structure layout, structural components, and instrumentation locations, respectively. In addition, Table 5.5 provides the steel section information for the structural columns and beams used in the analysis.

The stress-strain analysis was performed on two building sections, designated as Sections A-A and B-B in Figure 5.3. These sections were selected since they provide insight on the structural behavior of the two principal frame axes. The assumed geometry for the analysis of Sections A-A and B-B are shown schematically in Figures 5.8 and 5.12, respectively. The analysis of each of these sections will now be presented separately.

Table 5.5 Section Properties of Structural Steel Columns and Beams.

Beam or Column Label	Steel Section Designation	Member Length (in.)	Section Area A_x (in.^{2})	Moment of Inertia I_z (in.^{4})	Strain Gages Attached to this Member
SECTION A-A					
C5	W 8x24	292.80	7.06	82.8	----------
C7	W 8x24	171.36	7.06	82.8	G9 and G10
C8	W 8x24	174.96	7.06	82.8	G5 and G6
B7	W 15x39	254.23	11.47	448.8	G17 and G18
B8	W 16x36	336.83	10.59	448.0	G11 and G12
SECTION B-B					
C4	W 8x24	292.92	7.06	82.8	G1 and G2
C8	W 8x24	174.96	7.06	82.8	G5 and G6
C10	W 8x24	299.76	7.06	82.8	G7 and G8
B5	W 10x22	245.76	6.49	118.0	G3 and G4
B10A	W 10x22	115.32	6.49	118.0	----------
B10B	W 10x22	123.84	6.49	118.0	G13 and G14

SECTION A-A: The first step in the analysis was to determine the deflected shape of the structure. This was based on the sign and magnitude of the measured strain (i.e., + = tension, - = compression) and noting the position of the respective gage in the frame. At most locations, gages were installed in pairs with one on the flange center and the other on the flange edge. Inspection of the gage pairs allowed for determination of the type of bending occurring at that location. If both gages measured strain of approximately the same magnitude (agreeing within ± 5 $\mu\varepsilon$), then uniaxial bending was confirmed. Alternatively, if the pair of gages measured different magnitudes, then biaxial bending was indicated. For the analysis, only values of maximum and residual strain were chosen. An interesting observation at some of the gage locations was that as the fracturing event progressed (i.e., the fractures propagated from the injection well), there were some stress reversals of members (i.e., tension to compression, or vice versa).

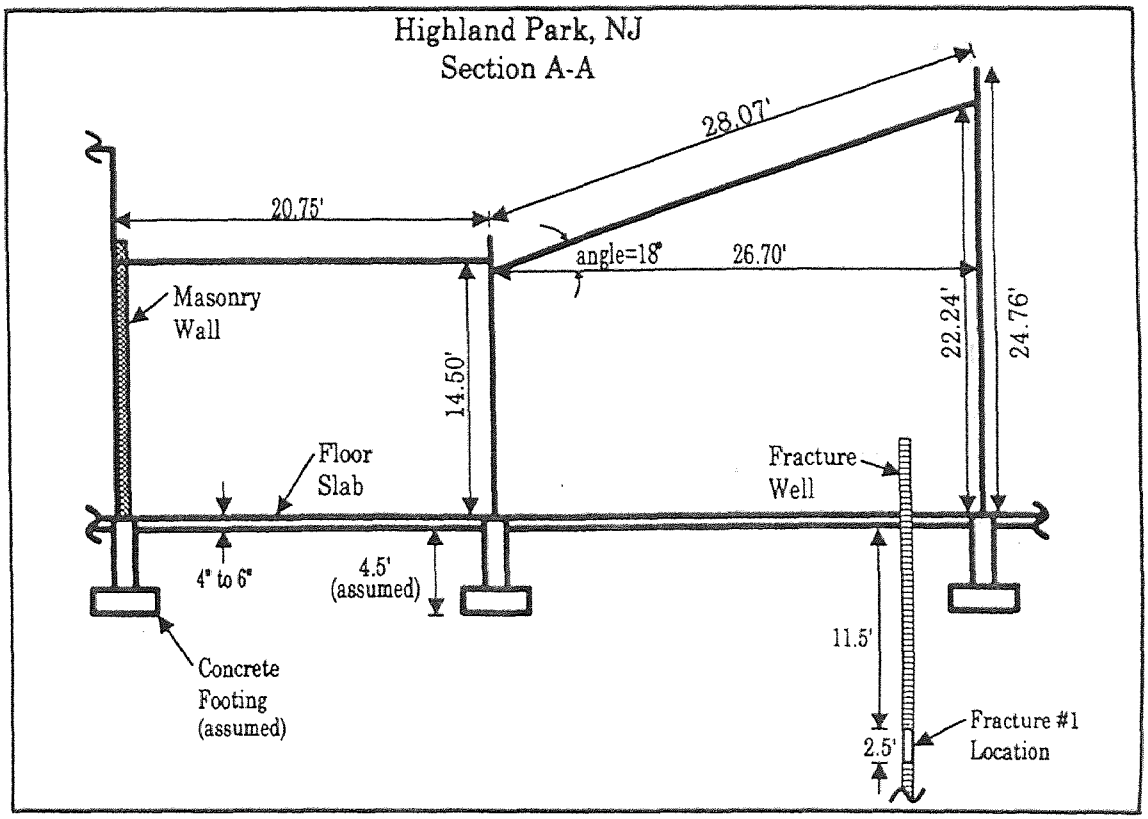

Figure 5.8 Section A-A, Fracture No. 1, Highland Park, NJ.

The results of the deflected shape analysis are depicted in Figure 5.9 which also shows relative slab and column heave based on data from the LVDTs, tiltmeters, and engineering levels. It is noted that the deflections have been greatly exaggerated for the purposes of visualizing the movements. An inspection of Figure 5.9 reveals that the deflected form is consistent with an upward heaving shape at the fracture well.

The next step in the analysis was to determine the maximum strain recorded during the fracturing event, as well as the residual strain after injection. This information was extracted from Table 5.4. The values of maximum and residual strain for the gages in section A-A are shown in Figure 5.10. As indicated, the maximum strain recorded during Fracture Injection No.1 was -53.0 με, while the maximum residual strain was 15.0 με.

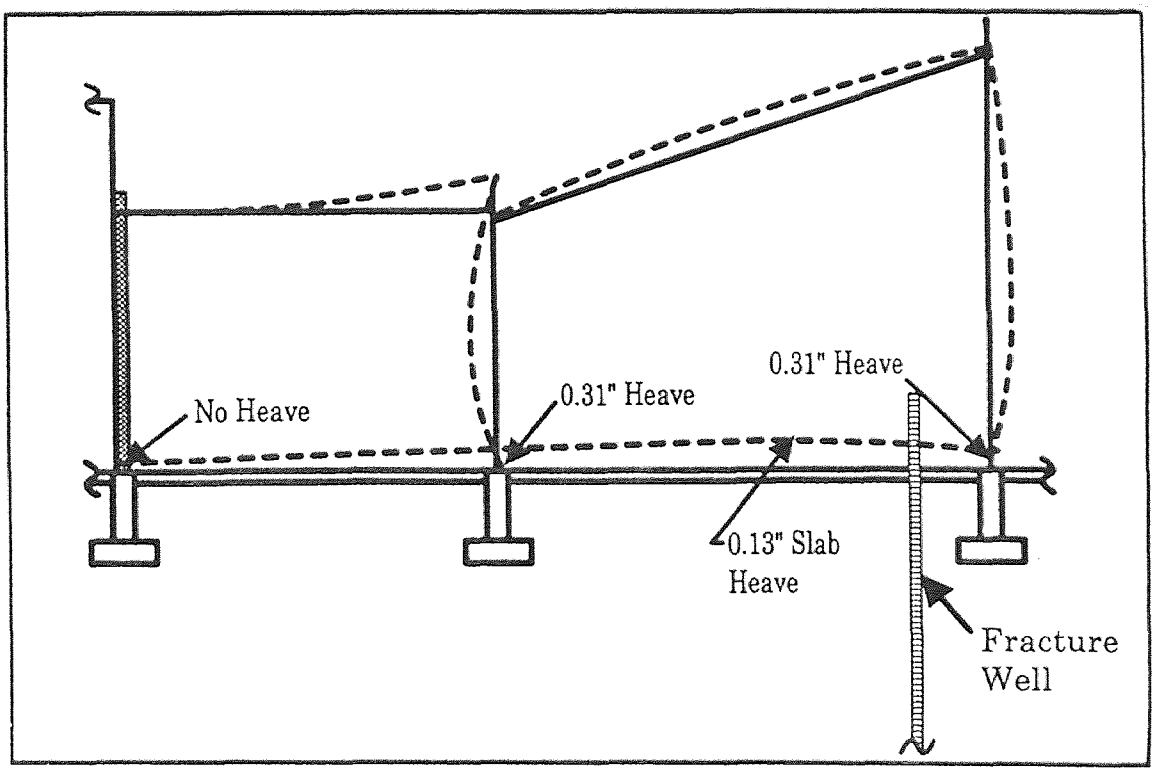

Figure 5.9 Exaggerated Deflected Structure Shape for Section A-A, Fracture No. 1.

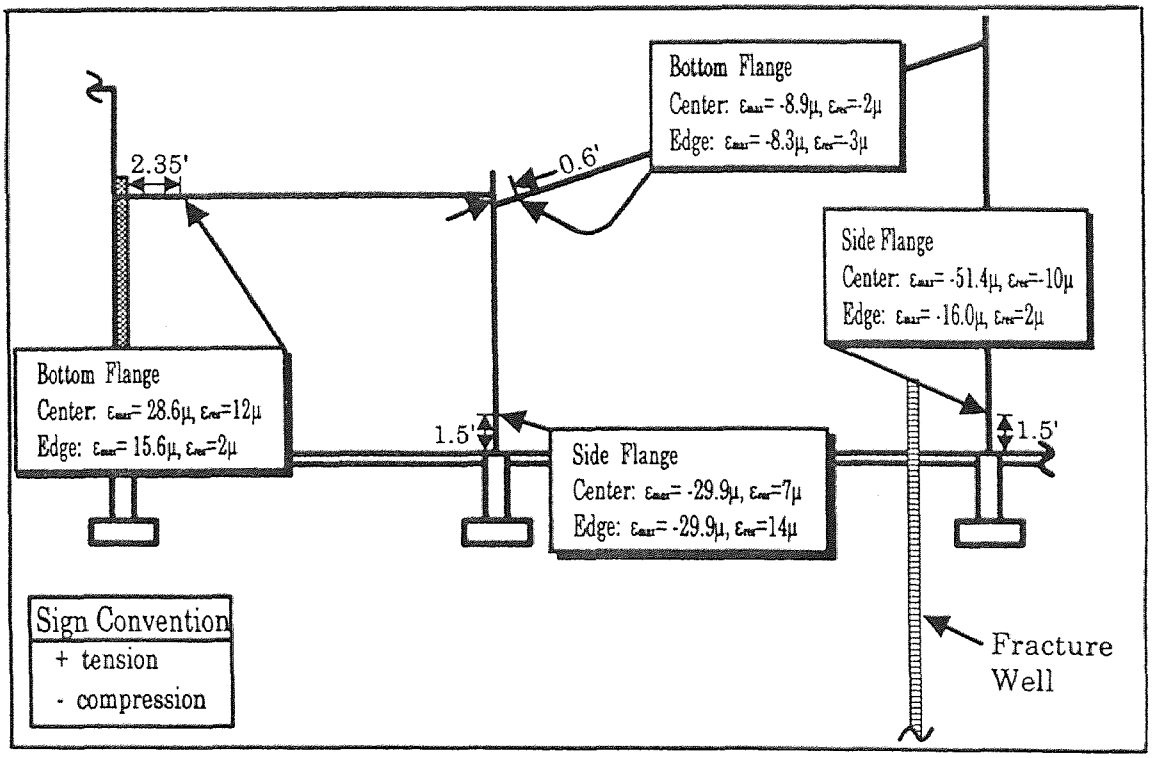

Figure 5.10 Strain Gage Measurements for Section A-A, Fracture No. 1.

The third step in the approximate analysis was to convert the maximum and residual strains into stresses, and then compare them with the original design stresses for the structure. Conversion from stress to strain was done (using Hooke's Law) by multiplying the assumed elastic modules for steel of 29,000,000 psi. The original design stresses were calculated using the tributary area method of load distribution. Dead loads were based on measurements of the actual building materials, and live loads were estimated using code design values which were presumably in effect at the time of the original construction. The original design loads and stresses for the columns and beams in Section A-A assumed for the analysis are summarized in Table 5.6, and the supporting calculations are contained in Appendix C.

Table 5.6 Original Design Loads and Stresses for Section A-A at Highland Park, NJ.

Member	Gages	Assumed Original Design Load, P (lbs.)	Axial Stress σ_a (psi)	Maximum Moment M_{max} (lb.-in.)	Stress Due to Bending σ_b (psi)	Estimated Original Design Stress at Gage Location σ_{total} (psi)
C5	None	--------	--------	--------	--------	--------
C7	G9, G10	23,460	3322.9	2437.4	464.5	3,787
C8	G5, G6	17,191.4	2,435	204,554	9,831	12,266

Member	Gages	Maximum Moment M_{max} (lb.-in.)	Estimated Original Design Stress at Beam Center σ_{total} (psi)	Estimated Original Design Stress at Gage Location σ_{total} (psi)
B7		674,191.5	11,972	--------
	G17, G18	302,235	--------	5,367
B8		977,596.6	18,334.6	--------
	G11, G12	70,161.5	--------	1,316

A comparison of the measured stresses and original design stresses is presented in Figure 5.11. The numbers in parentheses represent the measured stress as a percent of the

estimated original design load, while the numbers in brackets represent the percent of the estimated original design stress at the beam center. As Figure 5.11 shows, the maximum stress observed during the fracture injection event was 22.9% of the original design stress. Residual stresses were generally half the maximum values. While both the maximum and residual stresses were clearly measurable, their magnitude will not have a significant effect on the structural integrity of the steel frame. In fact, if a direct comparison of the stresses caused is made with the allowable steel stress in bending of 18,000 psi at the time of original construction, the percentage of induced stress drops to a maximum of 14.6%. When the factor of safety inherent in the original design is considered, it is clear that the stresses induced by fracturing are well within the elastic range.

It is interesting to note that the beams consistently experienced less stress than the columns. This was attributed to the generally low degree of fixity of the beam-column connection. This is especially seen for the angled beam which is attached by a flexible web connection. The other beam experienced somewhat higher stress values owing to its embedment in the masonry wall.

Although the movements of the building frame did not greatly affect structural integrity, they were sufficient to cause cosmetic damage had the building contained finished surfaces. Cosmetic damage consists of cracked plaster walls, cracked floors, broken windows, jamming doors and windows, and other minor damages which are non-structural in nature. During the current study no cosmetic damage was observed, since the interior was largely unfinished. It is noted, however, that Accutech reported two broken windows during a sequence of fractures at another injection well 8 ft outside of the test structure, thereby confirming the potential for cosmetic damage.

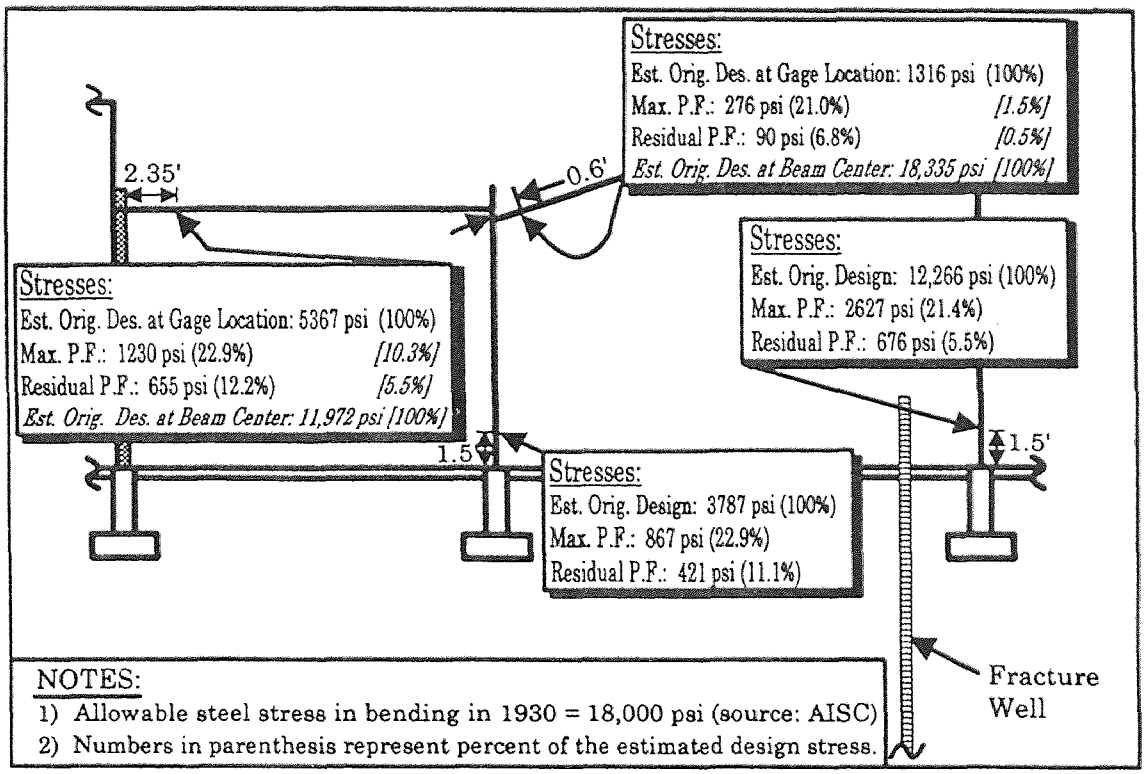

Figure 5.11 Stresses for Section A-A, Fracture No. 1.

SECTION B-B: A similar, but less rigorous analysis was performed for Section B-B. The assumed geometry for analysis is shown schematically in Figure 5.12. In general, the same procedure was used to determine the deformed shape of Section B-B, and the results are shown in Figure 5.13. As before, the deflections have been greatly exaggerated for the purposes of visualizing the movements. Figure 5.13 reveals that the deflected ground surface around the fracture injection well had an upward heaving shape, which is consistent with observations from the analysis of Section A-A.

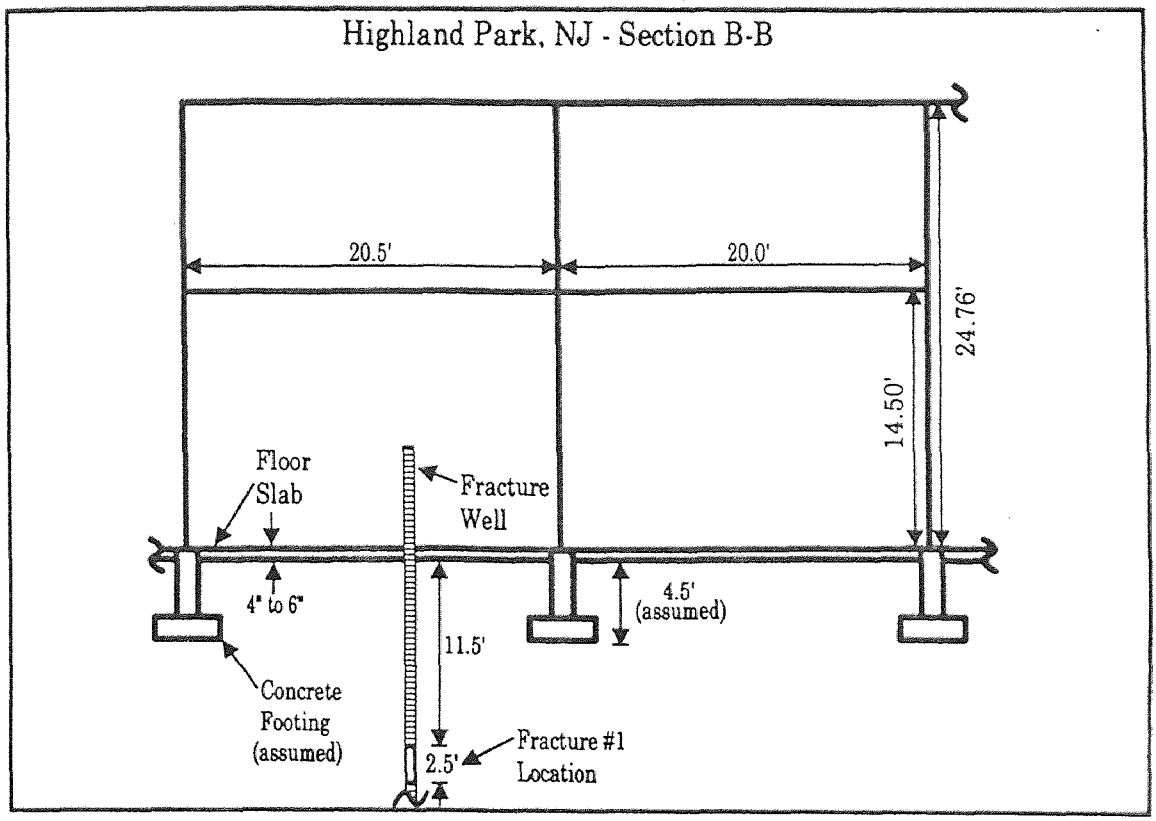

Figure 5.12 Section B-B, Fracture No. 1, Highland Park, NJ.

The maximum strain value recorded in Section B-B during Fracture Injection No.1 was -53.0 με, while the maximum residual strain was -13.0 με. It is noted that the maximum strain recorded for Section B-B occurred at the same location as the maximum strain for Section A-A, i.e., at the intersection of the two frames. Since the measured strains for this section were equal to or smaller than those of Section A-A, the resulting computed stresses were also equal or smaller.

The stress-strain analysis provided another important insight into the response of the test structure to pneumatic injections. This can be seen in Figure 5.14, in which the solid black bar represents the heave of the columns, while the cross-hatched area represents the heave of the slab. A comparison of the relative heave magnitudes clearly

shows that the columns and the slab acted independently, with the columns heaving considerably more than the slab. This can be explained by the fact that the columns are supported on footings which are founded at least several feet deeper than the ground slab. Thus, the column footings were closer to the fracture level and therefore experienced greater movements. Conversely, the additional thickness of soil fill beneath the slab apparently attenuated the vertical strain due to the fracture.

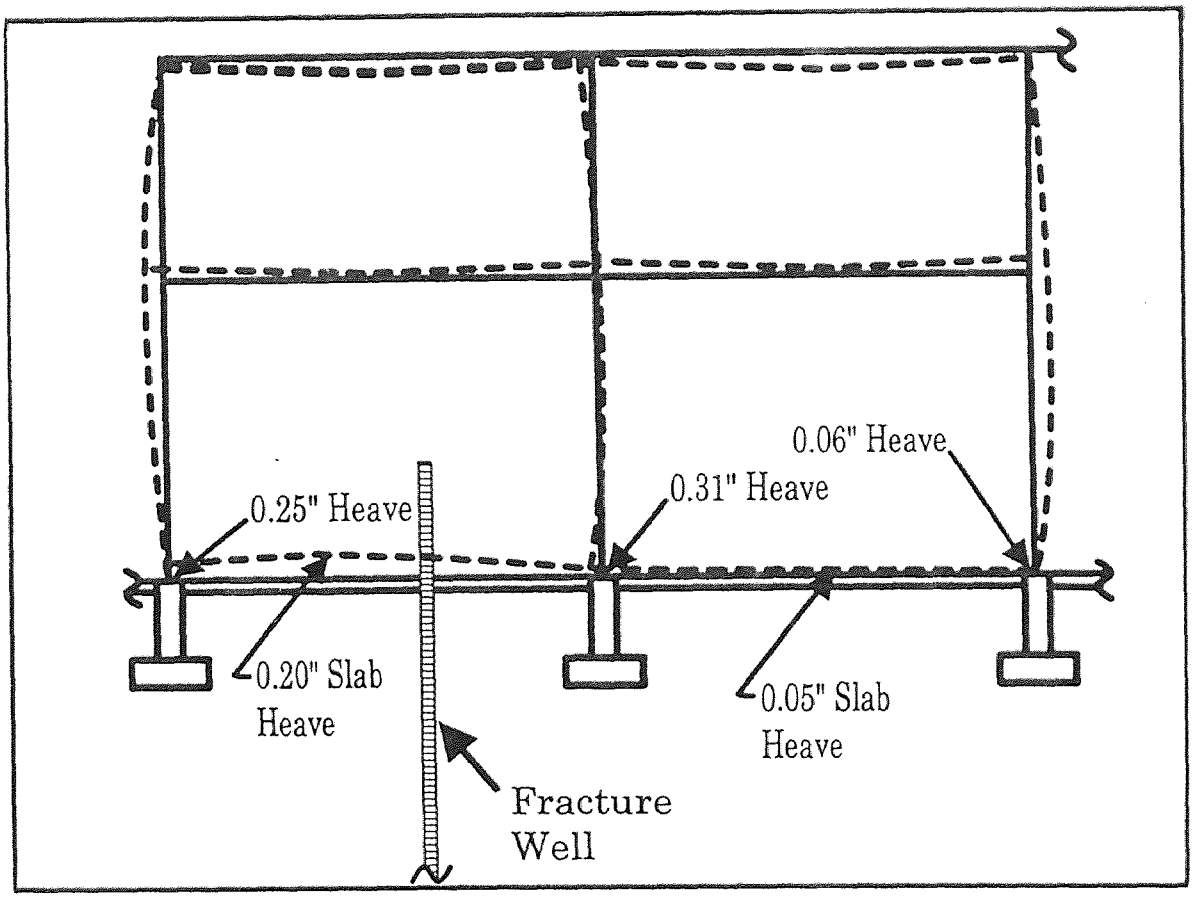

Figure 5.13 Exaggerated Deflected Structure Shape for Section B-B, Fracture No. 1.

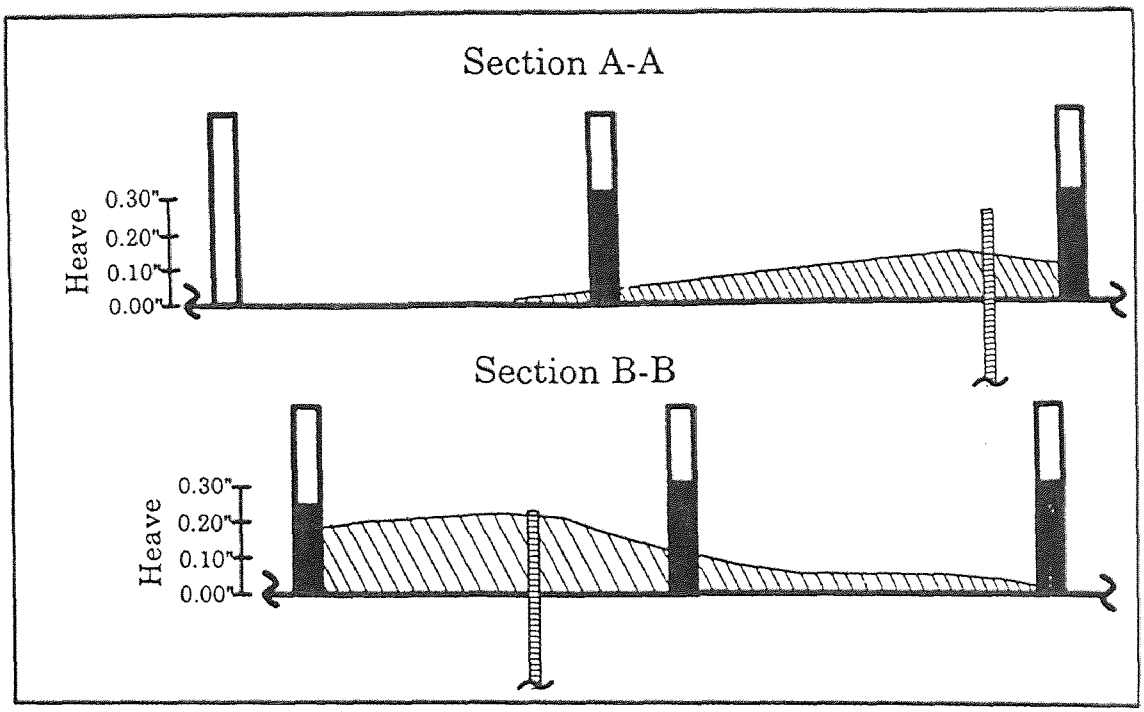

Figure 5.14 Conceptual Diagram Showing the Different Movements of the Slab and Structural Columns.

SUMMARY OF RESULTS: The most significant conclusions of the stress-strain analysis are summarized as follows:

1. The instrumented field tests provided good insight into the dynamic response of this building structure to pneumatic injections. The multiple electronic strain gages revealed the magnitude of stresses in the frame, as well as the general deflected shape. The tiltmeters, LVDTs, and optical engineering levels successfully recorded the heaving slab and columns.

2. Maximum stresses in the steel members during the injection were found to be quite tolerable, ranging from 1.5% to 22.9% of the original design stress. Residual stresses were consistently less, ranging from 0% to 11.1% of the original design stress. All stresses experienced during the pneumatic injections were well within the design factor of safety and elastic range of the structural steel, so the integrity of the steel members were not seriously affected.

3. In some cases, strain gage data showed progressive structural movements and stress reversals (i.e., tension to compression and vice versa). This suggests that different types of damage may occur at various times as the fracture network progressively radiates away from the fracture injection well.

4. The deflected shapes revealed that the structure and slab reacted as independent units during the fracturing event. This is attributed to the footings being located several feet closer to the actual pneumatic injection.

5. Although the structural integrity of the building was not compromised, the movements were of sufficient magnitude to cause considerable cosmetic damage if the building had interior finishes. The test suggests that repairs such as patching plaster, replacing windows, and adjusting doors and windows may be necessary in some applications.

5.5.2 Two-Dimensional Computer Analysis

A computer analysis was performed for the frame Section A-A to provide a check of the stress-strain analysis, and also to study the effect of "incremental" movements of the building frame. The analysis was performed in two dimensions using the program STAAD

III by Research Engineers, Inc. Details of this analysis are not included with this study, but can be found in the HSMRC report cited in the introductory paragraph of this chapter (Schuring, et.al, 1996). Only a summary of key findings of the analysis are presented.

The computer analysis confirmed the findings of the stress-strain computations presented in Section 5.5.1. Most importantly, the computer analysis confirmed that the structural integrity of the building frame was not adversely affected by the fracturing process. In fact, the computer model predicted lower stress levels in the frame members than the stress-strain analysis. The maximum combined stress predicted by the computer model was 1658 psi, and the maximum shear stress was 102 psi. The computer analysis also indicated that the stresses in the masonry wall were insufficient to cause cracking of the mortar. These findings suggest that the stress-strain analysis provides a conservative approach for future applications of pneumatic fracturing beneath structures.

CHAPTER 6

DESIGN GUIDELINES

Knowledge gained from the analysis of this test structure, combined with observations made at other previously fractured sites, were used to define three hypothetical cases of building response. Contaminated sites with overlying structures can be classified into one of these three cases based on site geology, fracture injection well location, fracture depth, and injection parameters (pressure and flow). The end objective is the development of a systematic design procedure which can be applied on a site-by-site basis.

6.1 Definition of Various Cases of Movement for Structures

The general analytical approach used to develop the three hypothetical cases was to treat ground surface heave as "reverse" settlement, and modify soil-structure interaction theory accordingly. The analysis incorporates both the stiffness response of the structure, as well as the stiffness response of the geologic strata overlying the fracture injection interval. The approach is based on a combination of methods which includes elastic plate bending theory and the deformation response of intrusive igneous laccolith formations. Observations from the current field study and other fracturing projects (see Table 6.1) suggest that at most sites, the geologic formation and overlying structures behave as deformable elastic media, with some exceptions which will be identified. Therefore, the movement can be described mathematically using the theory of elasticity.

The proposed concept of "reverse" settlement requires two important modifications compared with conventional settlement analysis. First, from a perspective of strain rate, ground movements caused by pneumatic fracturing are much more rapid

than gradual building settlements. This will alter the strain response for most structural materials, and will require a "total strain energy" approach integrating both deformation and time. Another deviation is deflection curvature, since upwardly heaving structures differ from structures which settle downward. The effect of deflection reversal may be significant, since many structures are specifically designed to resist downward deflection. This limitation was mentioned previously in Section 3.3 with regard to "hogging and sagging." For some structures (i.e., masonry) the relative magnitude of movement necessary to cause damage is significantly smaller for conditions of hogging than sagging.

Table 6.1 Summary of Pneumatic Fracturing Near Structures and Utilities.

Site	Formation and Fract. Depth	Nearby Structures or Utilities	Heave During Inj. (in.)		Residual Heave (in.)		Remarks
			Max	Ave	Max	Ave	
Richmond, VA	Stiff Silty Clay 7-11 ft	Abandoned tank farm over inj. area with 6 in. thick reinforced concrete pad (12 in. thick sidewalls).	1.06	0.35	0.19	0.05	Minor effects on concrete pad and wall. Slight widening and extension of existing cracks.
Newark, NJ	Fractured Sandstone 9-17 ft	New asphalt pavement over injection area. Buried sewer pipeline approximately 20 ft away.	0.16	0.12	0.03	0.02	No observable effects on pavement or sewer.
Roseland, NJ	Fill Overlying Silt, Sand, and Clay 4-7 ft	One-story warehouse building approximately 9 ft from injection. Block masonry on concrete footing.	0.86	0.35	0.34	0.05	No observable movement or effect on building structure. Surface heave data indicated that fractures "reflected" away from building.
Shreveport, LA	Medium Stiff, Clayey Silt and Sand 12-15 ft	Active above-ground tank farm approximately 15 ft from injection. Steel tanks mounted horizontally on concrete saddles.	1.0		0.25		Closest tank exhibited differential movement to 0.16 in. maximum. No observable effects on condition and integrity of tank and connecting utilities.
Oklahoma City, OK	(a) Fill Consisting of Mixed Clay, Sand, and Silt 7-9 ft	Abandoned and filled underground storage tanks approximately 12 ft from injection. Concrete tank was 50 ft diameter by 22 ft deep.	1.2	0.67			Structural effects on tank not observable due to burial. Surface heave data indicated tank did not move and fractures "reflected" away from tank walls.
Oklahoma City, OK	(b) Silty Sand and Cemented Sandstone 4-7 ft	Same tank as above. Injection made 2 ft from tank.	0.15	0.11			Structural effects on tank not observable due to burial. Surface heave data indicated tank movement of ≈0.1 in. upward during injection.

Another consideration which affects the model approach is the deformable nature of soil and rock media. Therefore, the actual fracture dimensions are usually larger than the observed surface heave, as some of the vertical movement is absorbed by the formation as elastic strain. Elastic theory indicates that the observed surface heave should vary as the inverse square of the depth. However, at shallow depths the formation does not behave as a totally elastic medium, and a lesser attenuation with depth may be expected. It is these intermediate depths that pose the greatest challenge to analyze. Unfortunately, this is the region most often encountered for sites undergoing pneumatic fracturing.

The response of a structure will depend on the materials and layout of the framing system, as well as the vertical and horizontal location of the injection well in relation to the foundation elements. With the methodology described above, various conditions of building response to pneumatically induced fractures have been subdivided into three conceptual cases as illustrated in Figure 6.1. As the figure shows, these consist of shallow, intermediate, and deep cases. Each of these cases are further described in Figures 6.2, 6.3, and 6.4, which provide a systematic discussion of each case including heave mechanism, heave magnitude and extent, and design recommendations.

Appendix D contains a design example illustrating the application of the ground deformation model equation to prospective pneumatic fracturing sites. This example also provided the basis for the depth limits for the various design cases mentioned above. In addition, recommendations for the selection of the design parameters necessary for application of the deformation model equation are presented.

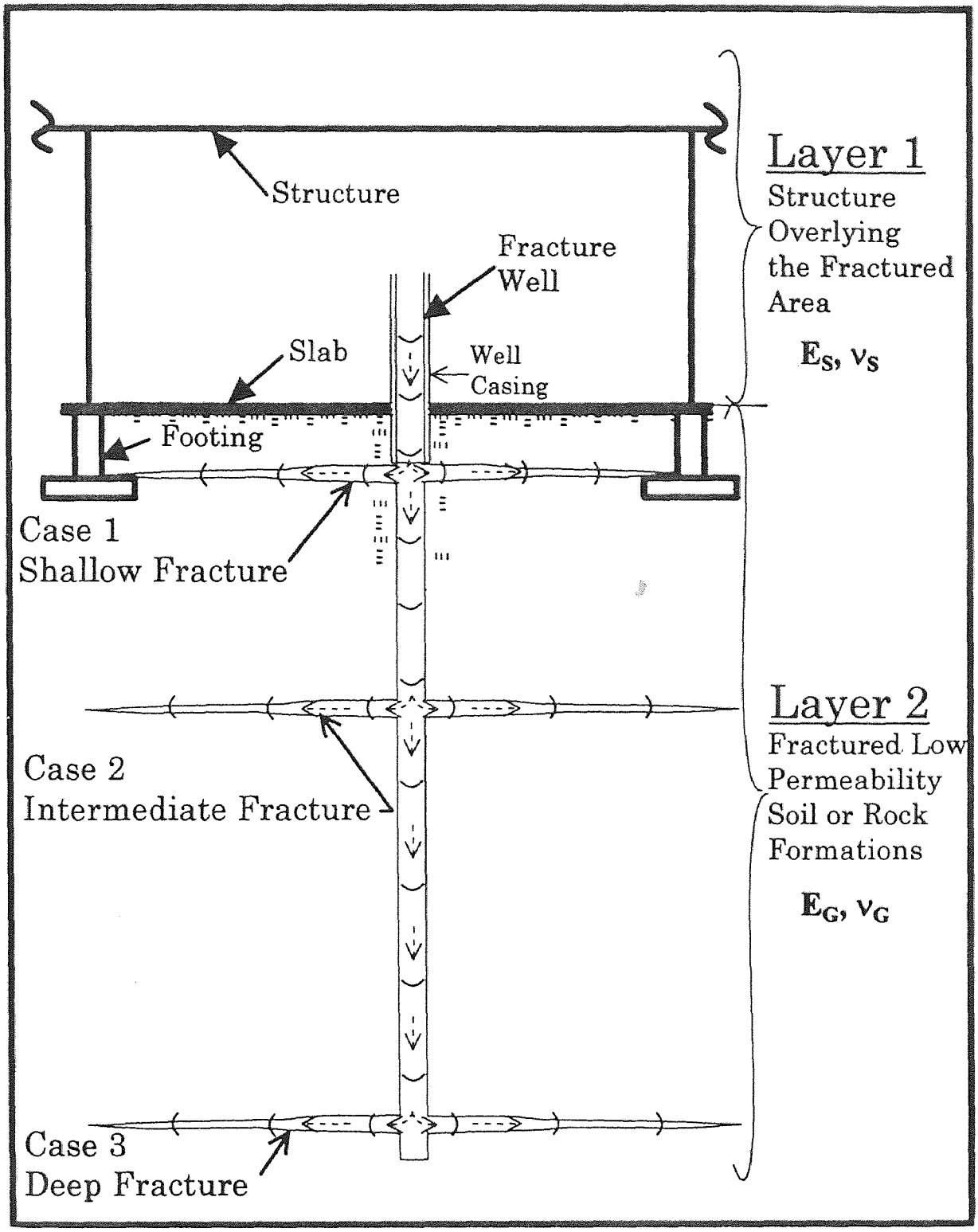

Figure 6.1 Conceptual Diagram Showing Cases for Fracturing Beneath Structures.

CASE 1 - SHALLOW FRACTURE DEPTH BENEATH A STRUCTURE

(last revised 1/17/97)

Case Definition:

Case 1 applies to sites where fracture injections are proposed at a shallow depth inside a structure: $z < 10$ ft for clay, $z < 8$ ft for rock, and $z < 10$ ft for granular materials.

Soil-Structure Heave Mechanism:

In this case, the geologic formation is too thin to establish significant rigidity and the weight of the geologic overburden is generally small. Therefore, a localized lifting of the overburden occurs in the vicinity of the fracture well, followed by a rebound (i.e., residual effect) to near normal conditions.

Magnitude and Extent of the Heave:

The area influenced during the fracturing event will have a relatively small radius as the table shows, and the magnitude of heave will approximately equal the fracture aperture (i.e., $w \approx b_f$). Residual heaves will be small, $w < 0.25$ in. for clays and rock, and $w < 0.13$ in. for granular materials.

CASE 1	Clays	Granular Soils	Fractured Rock
Approximate Range of the Radius of Influence, R, (ft)	R < 15 ft	R < 10 ft	R < 20 ft

Design Recommendations:

For flexible structures with independent footings, the injection wells should be centered between columns and/or wall footings.

For rigid structures (e.g., mat foundation), the open areas between supports for the superstructure are best suited for locating the fracture wells. However, these locations may be expanded outward from the center areas up to 30% due to the increased structure stiffness and weight.

In situations where it is critical to move closer to individual footings or superstructure supports, a pilot fracturing test performed outside of the structure in the same geologic formation can be performed to define the radial extent and magnitude of the expected heave. These values can then be used in conjunction with the tolerable movement criteria to create a new limiting boundary closer to the footings or superstructure support elements.

Figure 6.2 Case 1 - Shallow Fracture Depth Beneath a Structure.

CASE 2 - INTERMEDIATE FRACTURE DEPTH BENEATH A STRUCTURE

(last revised 1/17/97)

Case Definition:

Case 2 applies to sites where fracture injections are proposed at moderate depths beneath a structure: z = 10 ft to 30 ft for clay, z = 8 ft to 30 ft for rock, and z = 10 ft to 20 ft for granular materials.

Soil-Structure Heave Mechanism:

In this case, the geologic overburden is thicker than Case 1 and it begins to establish some rigidity and uniformity as a unit. In addition, the weight of the overburden increases. The overall structure stiffness and weight also start to influence fracture propagation. Consequently, a larger area is influenced by the fracturing as the geologic formation and structure start to act as elastic units.

For flexible structures with individual footings, the footings closest to the pneumatic injections will likely experience the greatest heave magnitudes. In addition, footings will likely move independently of the floor slab and non-structural walls.

For rigid structures with a single foundation element, the deformation will be similar to that of a stack of elastic plates subjected to a uniform or linear pressure distribution. Consequently, this is how it should be studied.

Magnitude and Extent of the Heave:

The area influenced by fracturing will be larger than for Case 1, and the magnitude of heave will be less than the fracture aperture on account of elastic strain shortening, ε_s, of the geologic layer (i.e., $w \approx b_f - \varepsilon_s$). However, in some cases the magnitude of heave of individual footings can be greater for Case 2 than for Case 1. This is because the applied pneumatic injection may apply an upward force directly on the footing in Case 2, whereas in Case 1 the transmitted load is usually not beneath the footing.

CASE 2	Clays	Granular Soils	Fractured Rock
Approximate Range of the Radius of Influence, R, (ft)	R = 15 to 25 ft	R = 5 to 15 ft	R = 20 to 40 ft

Design Recommendations:

The same design recommendations proposed for Case 1 should be applied to Case 2. In addition, for structures with individual footings, extreme caution should be exercised since differential movements of individual footings can lead to potential damage. This is the most difficult case for predicting building response to fracturing.

Figure 6.3 Case 2 - Intermediate Fracture Depth Beneath a Structure.

CASE 3 - DEEP FRACTURE DEPTH BENEATH A STRUCTURE

(last revised 1/17/97)

Case Definition:

Case 3 applies to sites where fracture injections are proposed for deep depths beneath a structure: z > 25 ft for clay, z > 25 ft for rock, and z >20 ft for granular materials.

Soil-Structure Heave Mechanism:

In this case, the thickness of the overlying geologic formation is significant and its modulus will dominate fracture behavior. In addition, the weight of the geologic overburden is also large. As a result, the structure stiffness and weight become insignificant compared with the formation effects. Consequently, heaves will be small and they will influence larger areas than in Cases 1 and 2. Fortunately, the magnitude of differential heave, if it even occurs, will be too small to cause any damage except in very specialized cases (e.g., when the building contains a highly sensitive piece of machinery).

In this case, both rigid and flexible structures may be treated as a stack of elastic plates subjected to a uniform or linear pressure distribution. At these deep depths it is not necessary to look at individual foundation elements.

Magnitude and Extent of the Heave:

The area influenced by the fracturing will be relatively large as the table shows, but the magnitude of heave will be much less than the fracture aperture (i.e., $w << b_f$). In fact, the measured heave may be so small as to be undetectable.

CASE 3	Clays	Granular Soils	Fractured Rock
Approximate Range of the Radius of Influence, R, (ft)	R > 20 ft	R > 10 ft	R > 30 ft

Design Recommendations:

First a survey should be conducted to determine if the facility contains any sensitive equipment/machinery. If so, a pilot test should be performed outside of the structure in the same geologic material with injections at the same proposed depths as inside. Heave values from this test can then be compared with the allowable movements of the equipment/machinery inside.

In general, the magnitudes of heave caused in the deep case are generally tolerable for both rigid and flexible structures. As always, sound engineering judgment should be applied on a site-by-site basis.

Figure 6.4 Case 3 - Deep Fracture Depth Beneath a Structure.

6.2 Utility Design Considerations

The nature of the product being carried within the pipe is probably the most important factor in determining allowable movement criteria for utility pipes. The consequences of failure for certain utilities can be extremely costly, and may even be life-threatening to workers associated with the fracturing. It is therefore mandatory that every possible precaution be exercised when fracturing is conducted in the vicinity of critical utilities. Utility services such as natural gas, chemical lines, and fuel supplies offer the greatest potential danger if failure occurs. Electrical conduits also pose a potential hazard, primarily related to cutting or drilling through of the utility itself. Other utility lines such as storm drains, water lines, and sewer lines pose less of a risk if damaged.

The best assurance against utility damage is to maintain adequate lateral clearance between the injection point and the utility line. Safe clearance distances will vary according to the geologic formation and the piping details, but usually falls within the range of 30 to 50 ft. If clearance cannot be maintained, then sound engineering judgment should be applied based on a reasonable safety factor applied to the deflection limit.

Whenever possible, or when there is any concern of damage, utilities should be shut down prior to the fracturing event, and then checked by the proper authorities prior to restoring service. In some cases, it may be necessary to expose critical points in a utility line by digging test pits so that visual inspections can be performed before and after the fracturing operation. Extreme cases may warrant the use of electronic strain gages or other continuous reading instrumentation to insure the integrity of a utility line.

When storage tanks are present at an industrial site, the potential effects of pneumatic fracturing must be carefully investigated. If movement in the tank area is

suspected, every possible precaution should be taken to insure its integrity. If possible, the tank should be emptied and all rigid connections should be disconnected. Many of the newer installations use fiberglass pipe and special flex-connectors for the product lines at both the tank and the adjoining structure. In these cases, the connections can probably remain intact since minor movements are tolerable. However, the product should still be removed from the tank. Many older tanks contain rigid piping connections and slip joints at the building entrances to allow for small movements. If possible, these connections should be disconnected and the slip joint checked for leakage prior to putting the tank back in service. Prior to the start of pneumatic injections, survey targets should be established on the tank supports to determine whether differential movements occurred during fracturing, otherwise, secondary stresses may be introduced into the tank shell when the tank is refilled with product. If significant movements are measured on the tank and supports, a precision tank tightness test should be performed on the system prior to returning it to service.

The type of bedding and trench backfill, and its contact with the pipe, will greatly influence how a utility line will react to applied loads and movements. In design practice, bedding conditions are generally divided into four classes (Class A through D) as illustrated in Figure 6.5. In general, pipes installed with a Class A or B rating will tolerate greater differential movements, since the select bedding and backfill materials contribute measurably to the structural support of the pipe. The select materials also greatly reduce the risk of localized deflection. There is also the issue of a fracture plane actually intersecting the pipe trench and causing direct damage. Once again, the higher class installations will respond more favorably since the granular fill surrounding the pipe

will dissipate the compressed air. Often, the most difficult part of evaluating existing utilities at sites is determining details of installations, since as-built records are often not available.

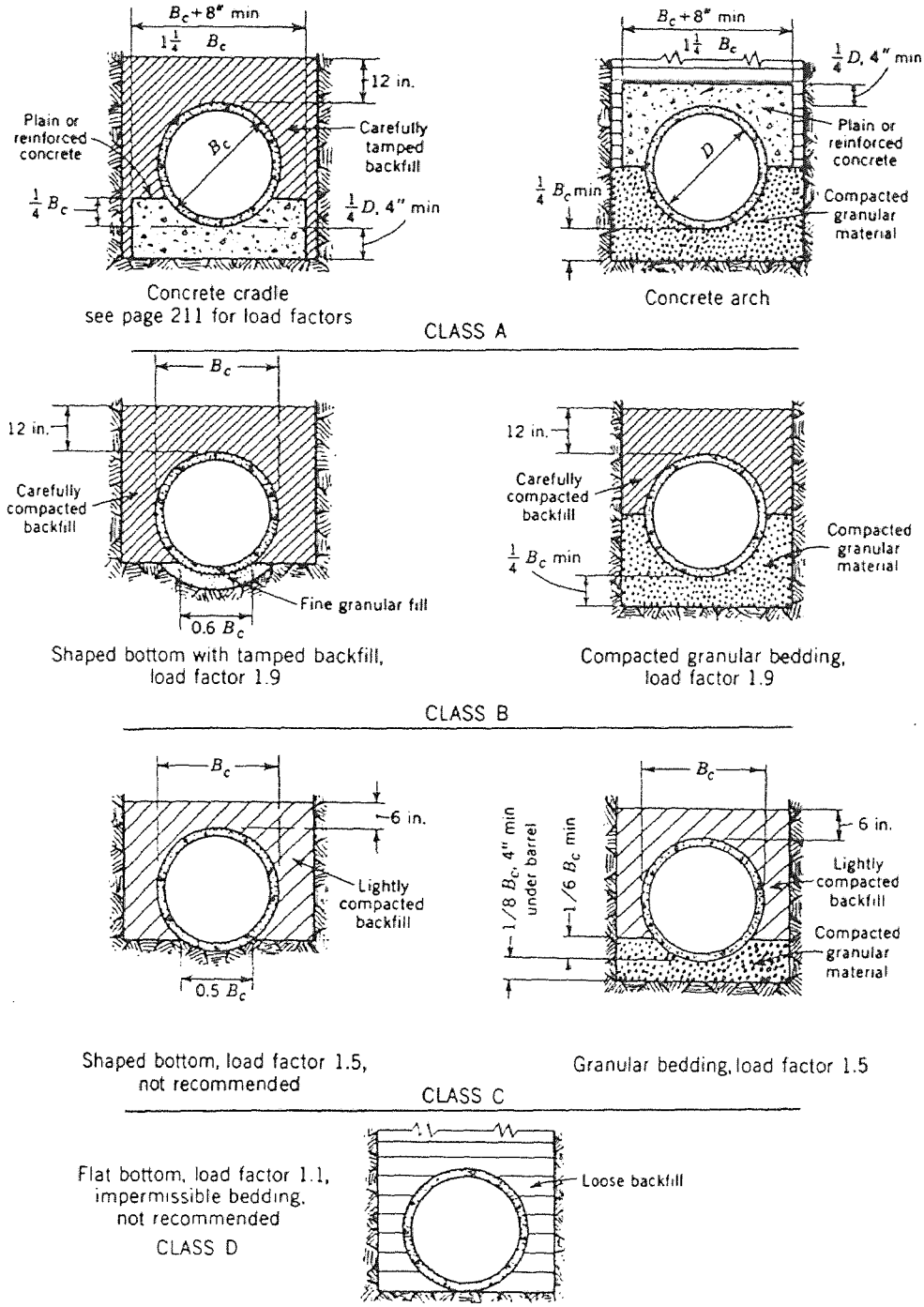

Figure 6.5 Classes of Bedding for Utility Pipes in Trenches (after American Society of Civil Engineers and the Water Pollution Control Federation, 1976).

6.3 Design Approach Procedure

This section presents a design procedure for implementing the pneumatic fracturing process beneath or adjacent to structures and utilities. It is based on the results of the current study, as well as past experience with fracturing. Although the procedure follows a step-by-step format, sound engineering judgment may supersede some the individual recommendations. The steps are as follows:

STEP 1 - Investigate the Facility Function:

Define the function of the facility, and determine how critical are its operations. For example, does it contain or process hazardous material that could leak? Does it house sensitive machinery which cannot tolerate movement? What are the consequences of damage and down time for the facility?

STEP 2 - Review As-Built Information (including utilities):

As-built drawings and other information should be consulted to establish the dimensions and composition of the structure and utilities. If as-builts are not available, exploratory test pits and/or cores may be necessary to determine actual dimensions of foundations and slabs. Also, it is important to thoroughly investigate all utilities in the area, especially critical utilities such as natural gas, liquid fuels, and hazardous chemicals.

STEP 3 - Conduct a Condition Survey:

A walk-through of the facility should be conducted and the condition of the structure examined. Any existing cracks or other distress should be documented with photos and/or video. Strain telltales should be installed across selected joints and significant existing cracks.

STEP 4 - Establish Allowable Movement Criteria:

Based upon information gathered in the previous steps, an allowable movement criteria can be established using values from Section 3.3 of this thesis. This should be coordinated with the facility's structural engineer.

STEP 5 - Perform Fracture Injection Design:

Design calculations should be performed to check the effect of heave on the structure. We recommend analyzing the formation and the structure using elastic plate bending theory. These should be compared with the allowable movement criteria, and fracture pressures and flow rates should be adjusted accordingly. If reliable soils data are not available, laboratory testing of samples recovered from the site should be performed.

STEP 6 - Perform a Pilot Test:

If the results of the design analysis indicate that fracturing can be conducted safely, a field pilot test should be performed. During the pilot test, we recommend movement monitoring of the structure with optical levels, tiltmeters, strain gages, and LVDTs, as appropriate. Critical utilities should be monitored for possible leaks during and after injection. All personnel should be cleared from a building if there is a perceived risk of structural distress or fugitive emissions from the subsurface.

CHAPTER 7

CONCLUSIONS AND RECOMMENDATIONS

7.1 Conclusions

A study was performed to investigate the effects of pneumatic fracturing on overlying structures and utilities. Pneumatic fracturing is a patented process which enhances the removal and treatment of hazardous contaminants from geologic formations. During pneumatic injections, measurable ground deformations are experienced both during the process, as well as after completion.

A mathematical design model for predicting ground deformations resulting from the pneumatic fracturing process was developed using data from over 40 pneumatically fractured sites. The model is based on elastic plate bending theory and geologic models describing igneous laccolith intrusions. The model calculates the magnitude of ground deformation caused by pneumatic fracturing. This calculated value represents the worst case scenario for movements of overlying structures and utilities. In general, overlying structures will tend to decrease the amount of movement due to the extra overburden weight and increased stiffness resulting from the structure.

An instrumented field test was performed beneath an actual contaminated industrial facility to obtain data on the dynamic response of the structure. The test structure was an abandoned warehouse with a steel frame and intermittent brick masonry shear walls. This type of building construction is commonly encountered at contaminated industrial and governmental sites. Although the pneumatic injection well was located within an atypical structural bay, knowledge gained from the field test provided excellent insight into the dynamic response of the structure.

A thorough review of differential settlement criteria from existing geotechnical engineering literature was performed. This allowed for the establishment of allowable movements in the proposed design process. The validity of this approach is based on the premise that all structures can tolerate some degree of differential movement without causing any visible or structural damage.

Finally, the results from the instrumented field test were combined with observations made at previously fractured sites to develop a systematic design guideline. The design guideline classifies the building type as either flexible or rigid, and then categorizes them into one of three characteristic design cases. Design recommendations and potential ground movements are provided so that contaminated industrial and governmental sites can be screened for the potential application of the pneumatic fracturing process.

As a result of this study, the following conclusions were reached:

- A thorough review of allowable differential movements for various classes of structures and utilities was undertaken. This allowed establishment of tolerable differential movement criteria for the structures and utilities typically found at contaminated facilities, and is incorporated into the systematic design guideline.

- Curves plotted from ground deformation field data of pneumatically fractured sites were fitted with symmetrical trendlines using curvilinear regression. The curve shape which consistently represented the field data was the fourth-order polynomial. In addition, due to the symmetry of the curves, the first and third-degree coefficients of

the equations were typically 10 to 20 orders of magnitude smaller than the other terms in the equation (i.e., they were nearly zero). As a result, the equation of the curves developed from the field data closely match the form of the equations used in elastic plate bending theory, thereby increasing the confidence level of the model approach.

- The deformed ground surface resulting from pneumatic injections was successfully modeled using plate bending theory coupled with formation models of intrusive igneous laccolith formations. The model is based on a circular plate subjected to a linear tapering pressure distribution. Comparison of the model results with actual field deformation data displayed reasonable agreement.

- The field test revealed that although the structural integrity of the test structure was not compromised, the movements were of sufficient magnitude to cause considerable cosmetic damage if the building had contained any interior finishes. This suggests that repairs such as patching plaster, replacing windows, and adjusting doors and windows may be necessary for some applications of the pneumatic fracturing technology.

- During the field test, all stresses experienced during the pneumatic injections were well within the design factor of safety and elastic range of the structural steel, so the integrity of the steel members were not seriously affected. Maximum stresses in the steel members during the test injections were found to be quite tolerable, ranging from 1.5% to 22.9% of the original design stress. Residual stresses were consistently less, ranging from 0% to 11.1% of the original design stress.

- Most buildings can be classified into one of three conceptual cases developed within the report. These three cases are defined based on the structural stiffness, site geology, injection well location, fracture depth, and the injection input parameters.

- When evaluating the effects of pneumatic injections on existing utilities, the designer must consider the kind of piping material, the nature of the product being carried, and the type of trench condition. Deflection limits are presented for the more commonly occurring pipes at contaminated industrial sites which can be used for site screening and design purposes. Extreme caution must be exercised when fracturing in the vicinity of critical utilities such as natural gas lines, chemical lines, fuel supplies, and electrical lines.

- With an understanding of the probable structural behavior for a particular building type, contaminated industrial and governmental sites can be screened for application of the pneumatic fracturing process using a systematic design procedure.

7.2 Recommendations

Although this study has greatly expanded the understanding of the effects of pneumatic injections on structures and utilities, further work is necessary to increase the confidence level of the results. The following future research is recommended:

1. Alternative pressure distributions should be analyzed and evaluated for possible inclusion of the model. Specifically, it is recommended that the following pressure distributions be examined: (1) cubic law (exponential); (2) a linear tapering pressure

distribution converted to an equivalent uniform distribution; and (3) a sinusoidal distribution.

2. Every effort should be made to expand the existing data base to improve reliability of the model. The following site conditions are desired to compliment the current pneumatic fracturing data base:
    - a flexible building structure founded on clay/silt soils;
    - a rigid, reinforced concrete structure founded on clay/silt soils;
    - a steel tank surface mounted on concrete supports; and
    - a buried utility pipeline which can be exposed and instrumented.

3. An attempt should be made to correlate Standard Penetration Test (SPT) data with elastic properties of soil formations. A similar correlation should be investigated for Rock Quality Designation (RQD) data for fractured rock formations. Such correlations would facilitate the screening of potential pneumatic fracturing sites where structures are involved.

APPENDIX A

MODEL DEVELOPMENT DATA

A.1 Normalized Ground Deformation Plots

The following five plots were used to validate the quality of the data used for the model development as was described in Chapter 4.

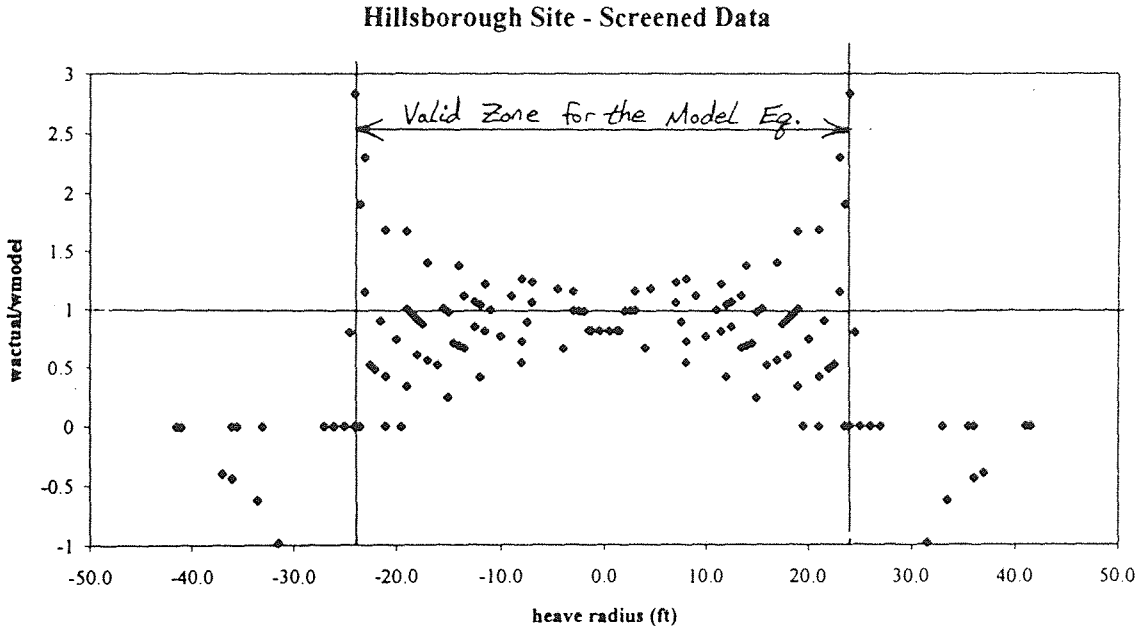

Figure A.1 Normalized Plot for the Hillsborough, NJ Site, Phase II.

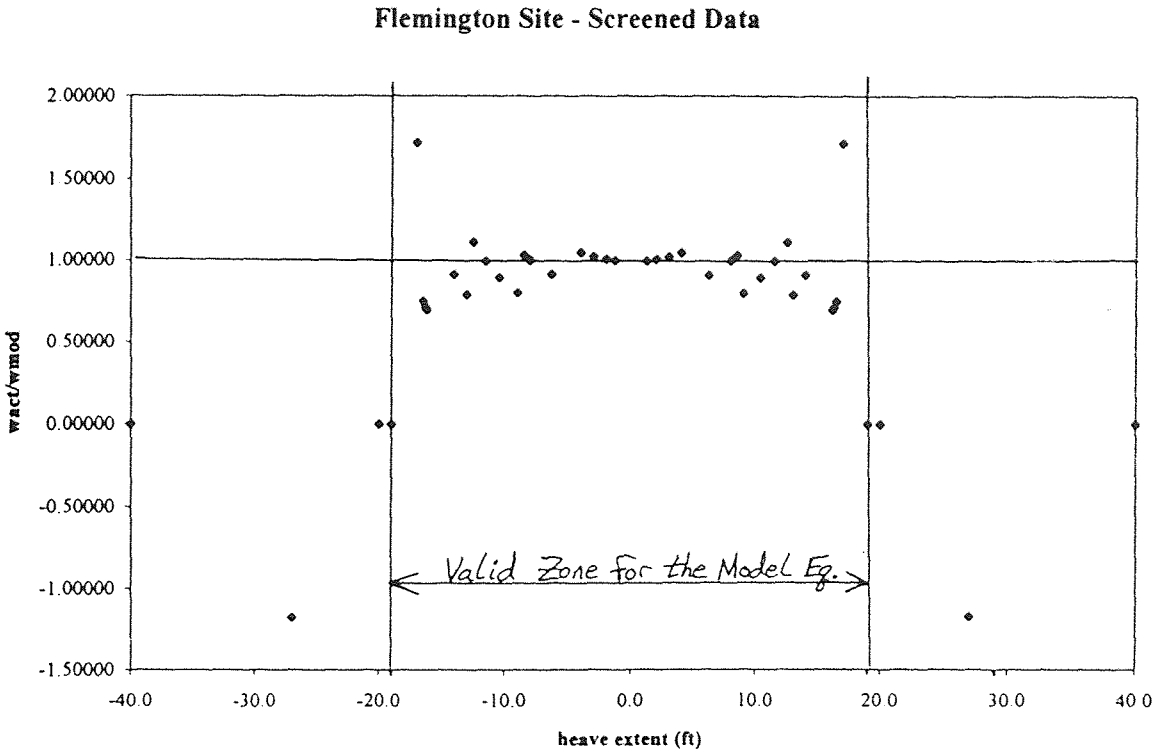

Figure A.2 Normalized Plot for the Flemington, NJ Site.

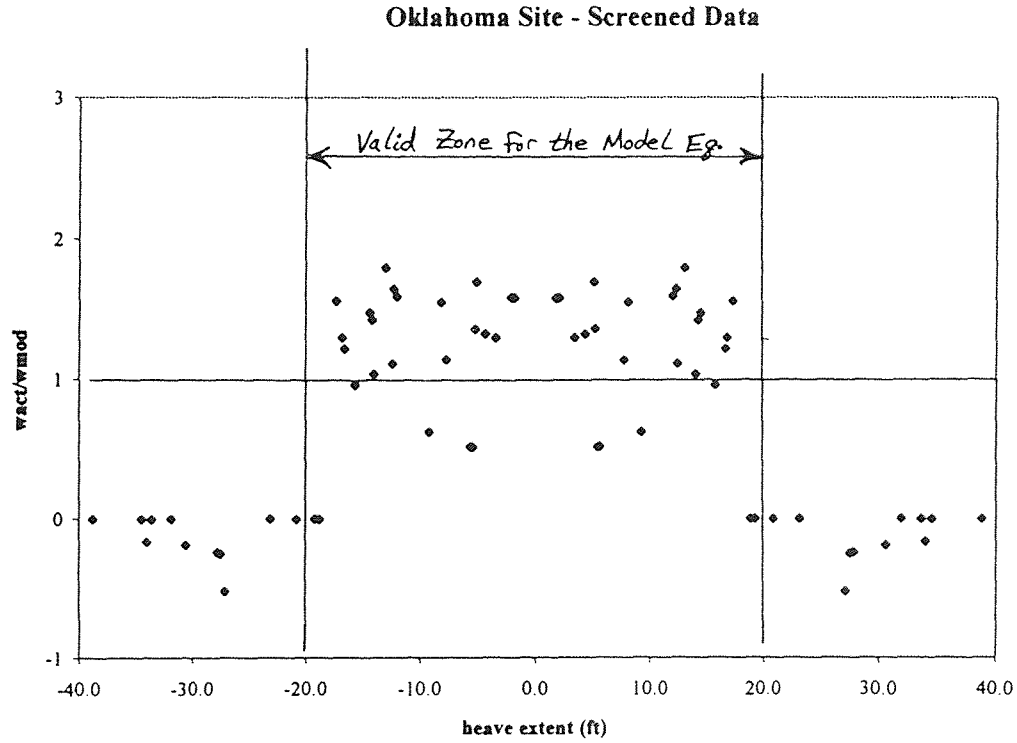

Figure A.3 Normalized Plot for the Tinker Air Force Base, Oklahoma Site.

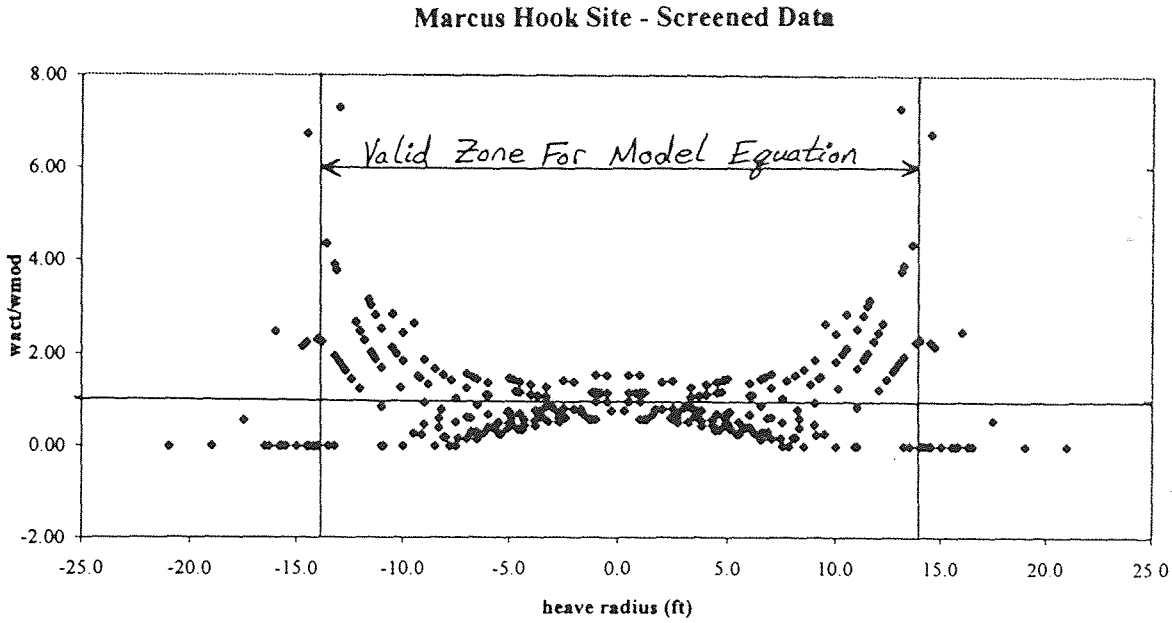

Figure A.4 Normalized Plot for the Marcus Hook, PA Site.

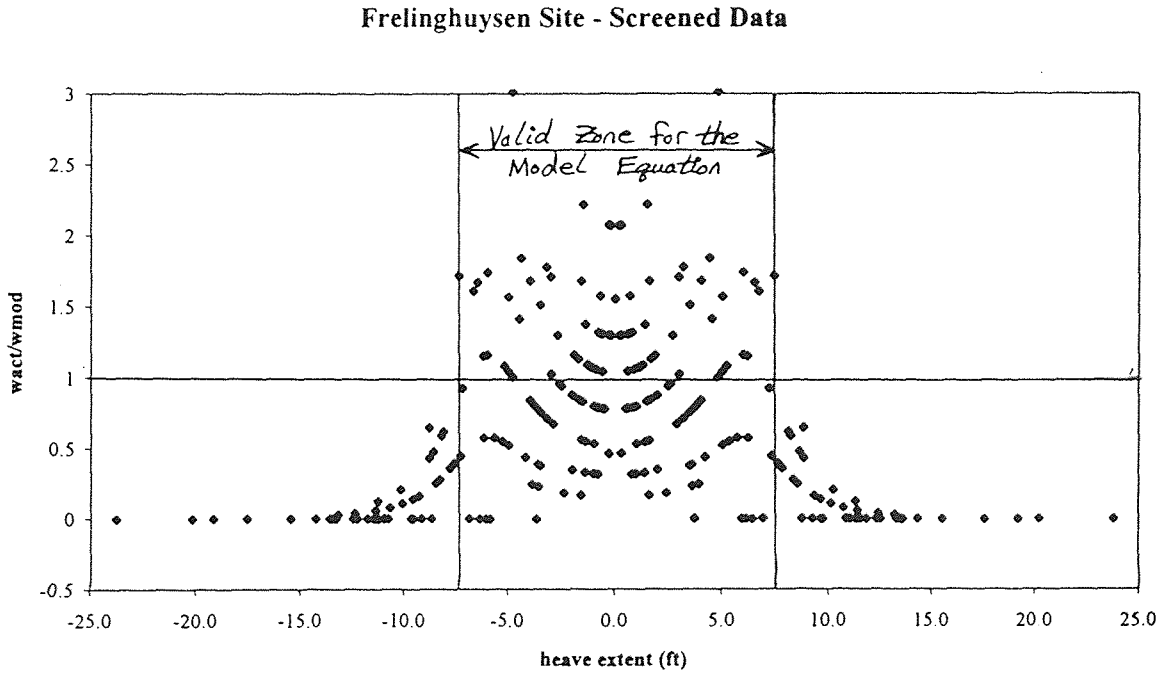

Figure A.5 Normalized Plot for the Frelinghuysen Site.

The following nineteen plots compare the ground deformation curves for three cases: (1) for the measured field deformation curves; (2) for the model deformation curve determined using Equation 4.13; and (3) from the average site curves shown in Table 4.1. Each plot shows four symmetrical curves for each fracture. These curves were developed using the methodology described in Chapter 4.

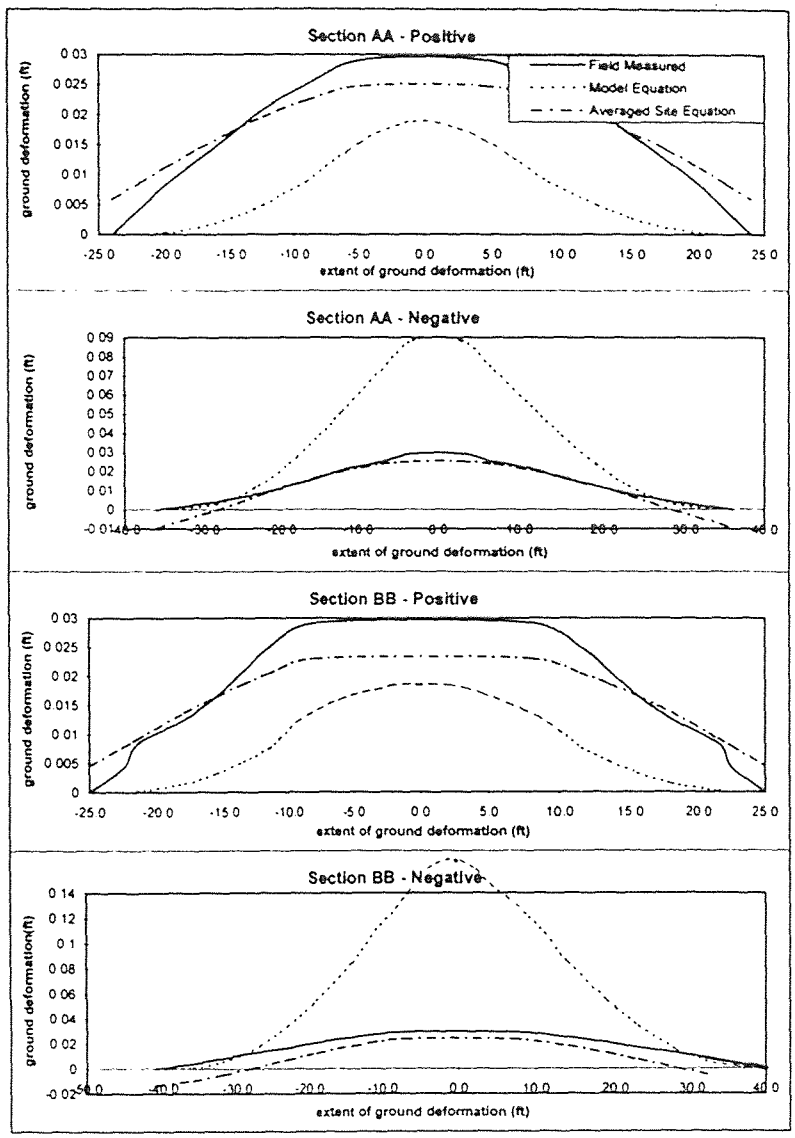

Figure A.6 Comparative Plot - Hillsborough, NJ Site, Phase II, 2-1.

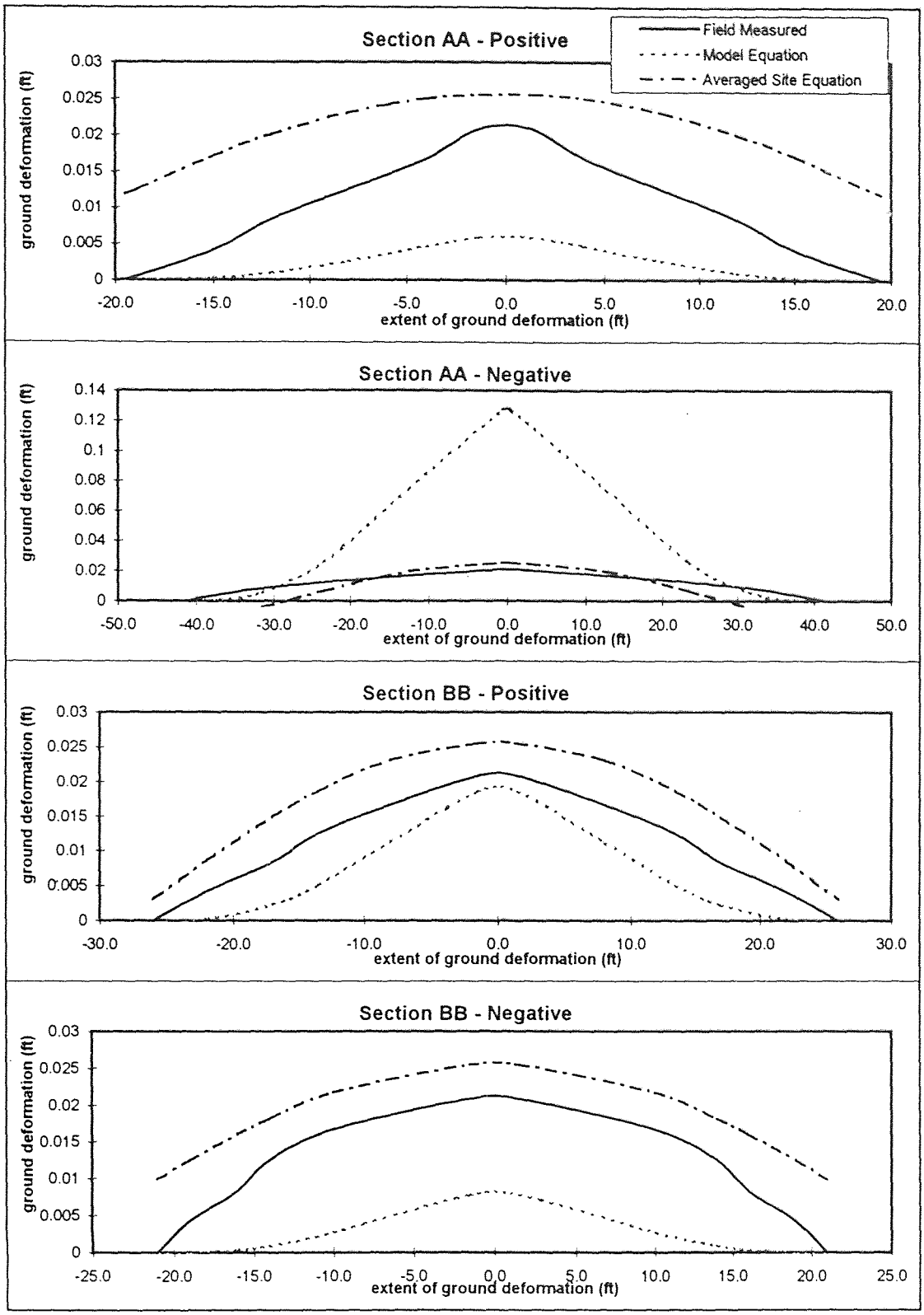

Figure A.7 Comparative Plot - Hillsborough, NJ Site, Phase II, 2-2.

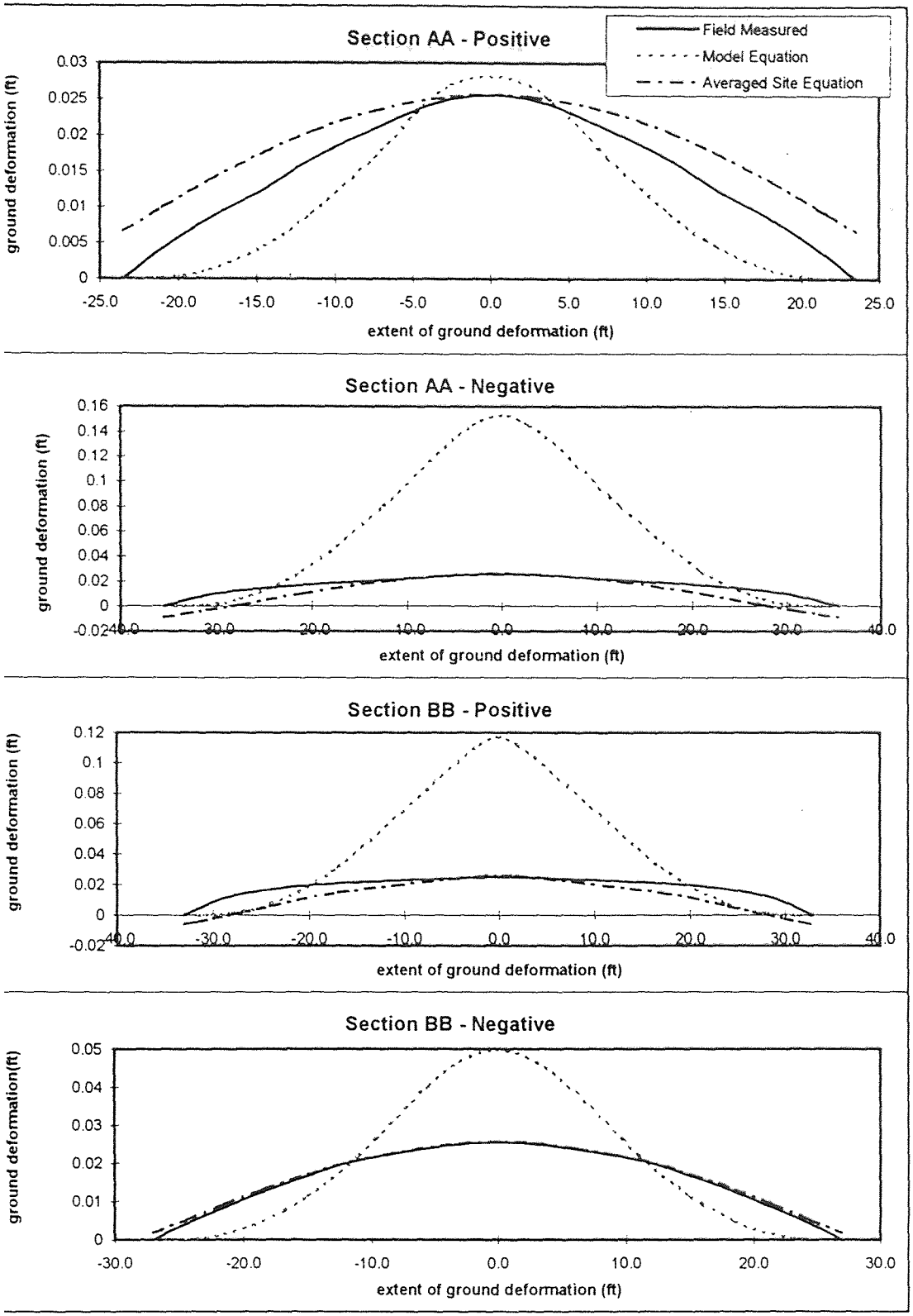

Figure A.8 Comparative Plot - Hillsborough, NJ Site, Phase II, 2-3.

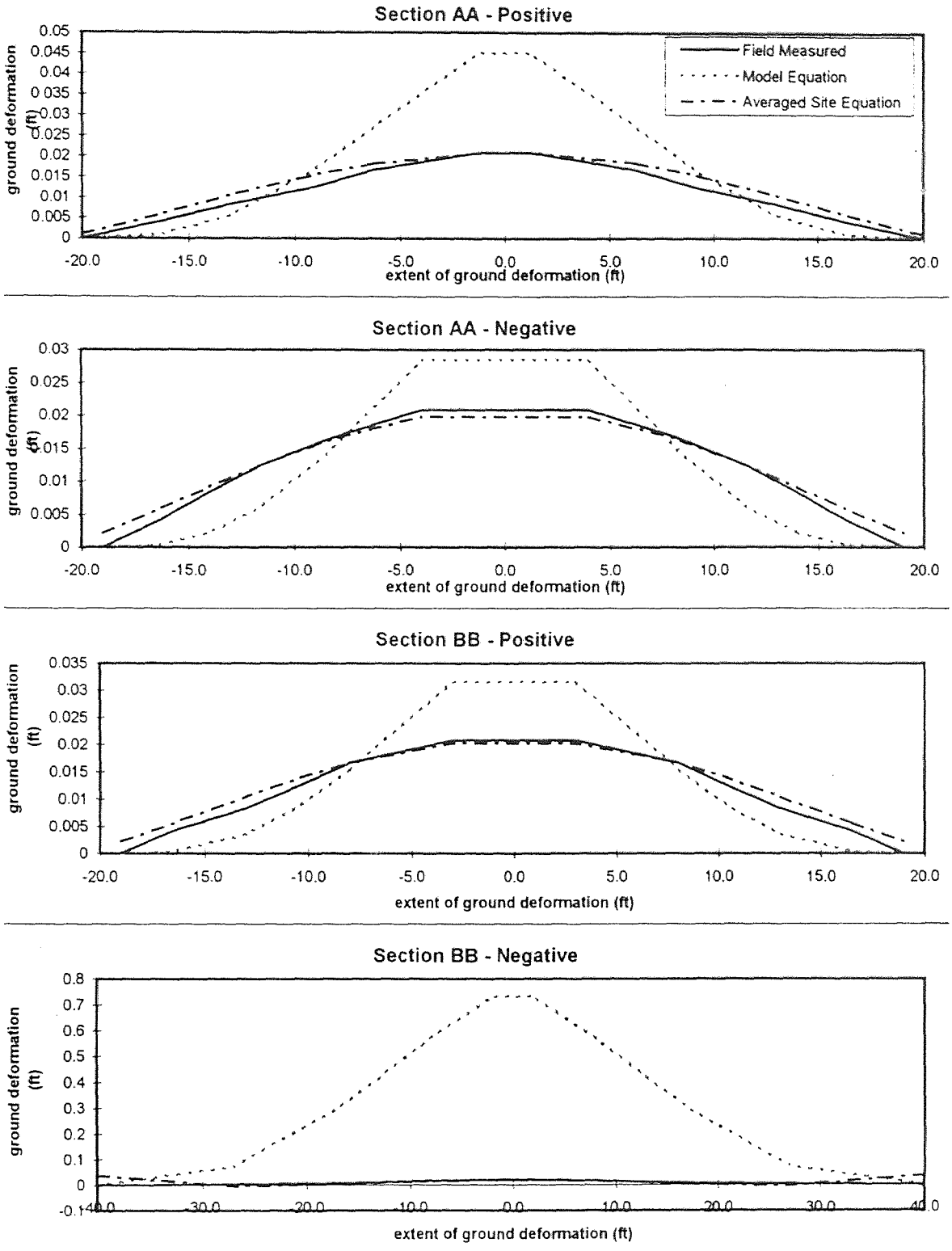

Figure A.9 Comparative Plot - Flemington, NJ Site, Depth = 15.6 feet.

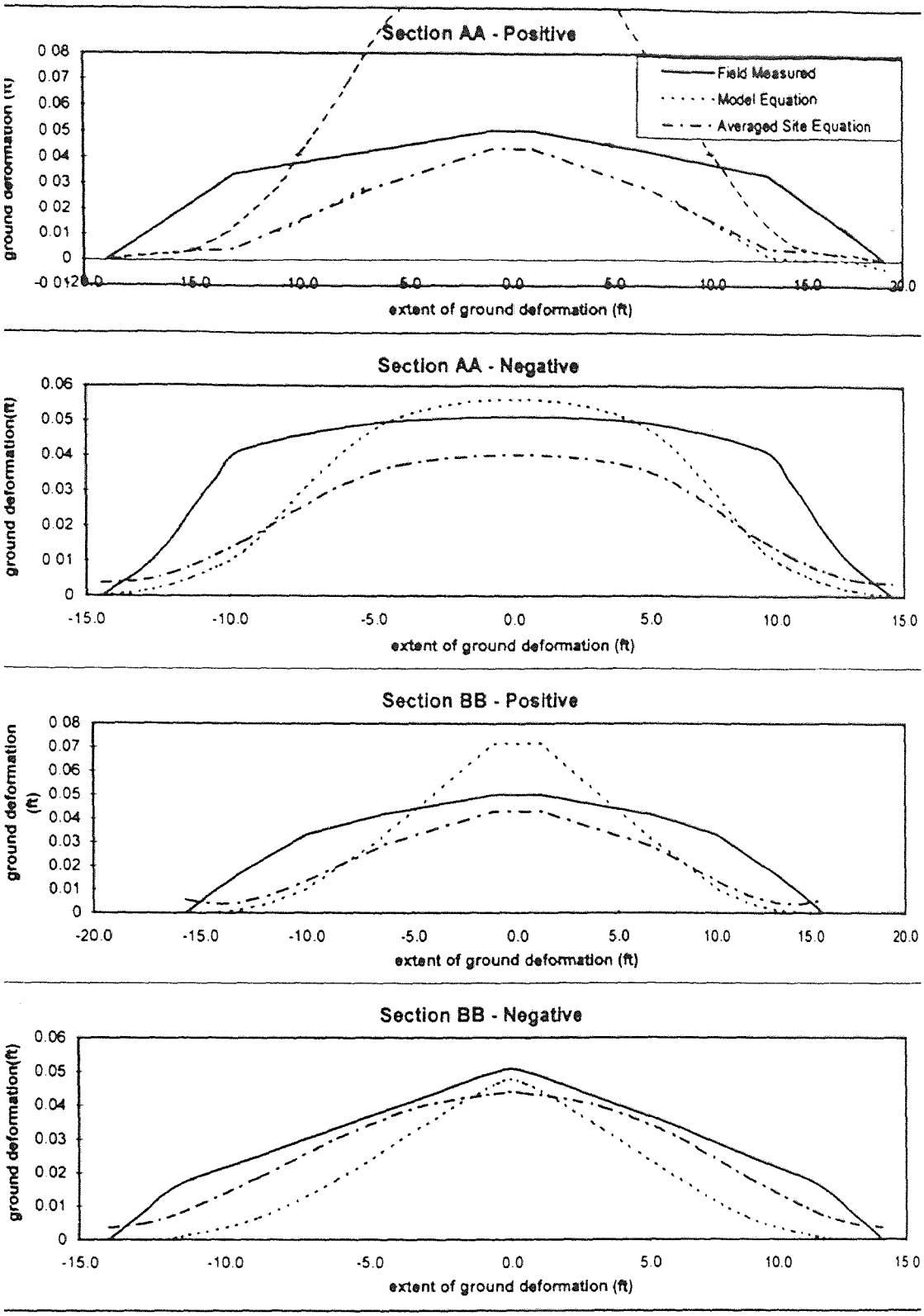

Figure A.10 Comparative Plot - Marcus Hook, PA Site, FW3-Inj.#1.

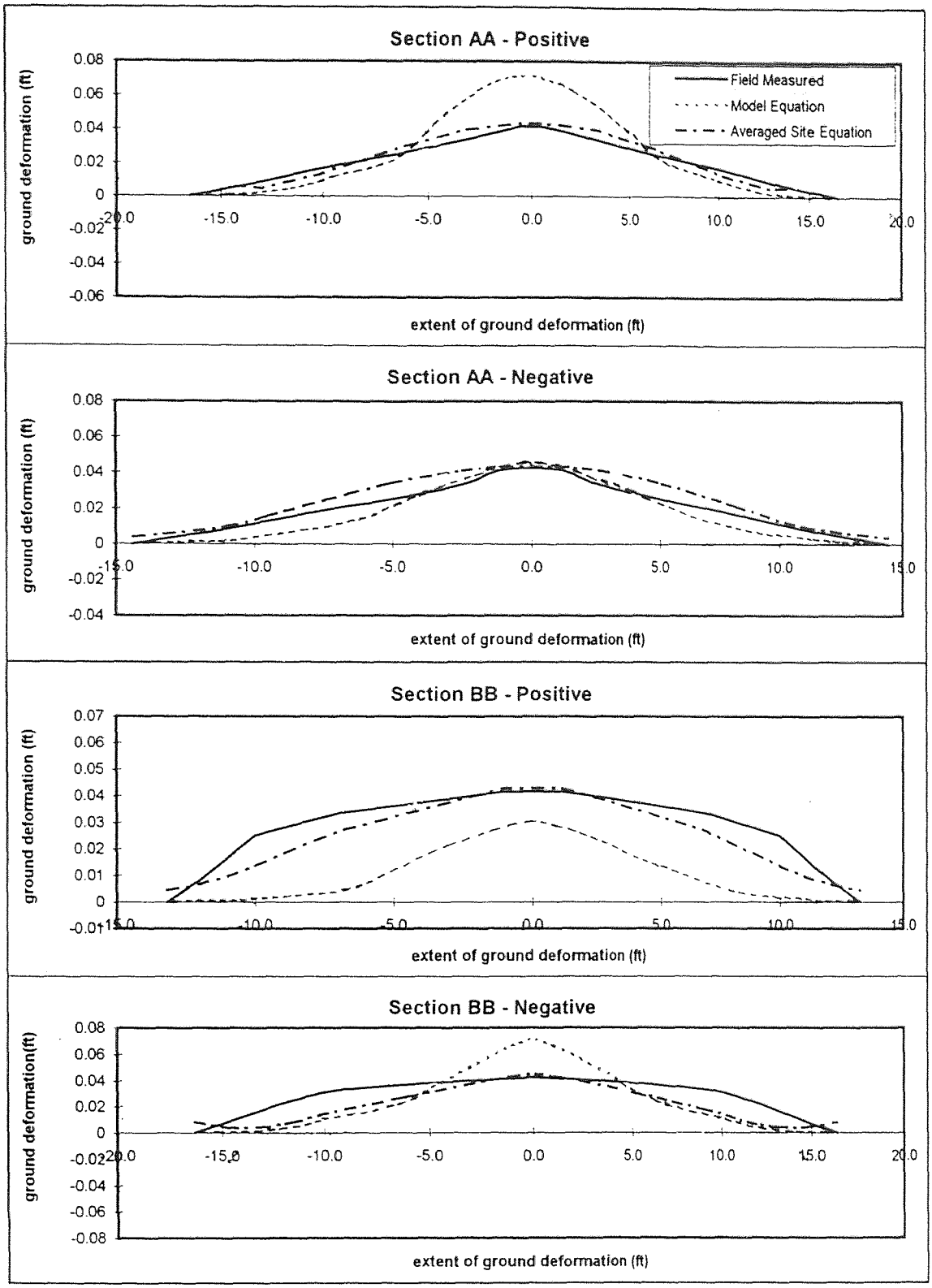

Figure A.11 Comparative Plot - Marcus Hook, PA Site, FW3-Inj.#3.

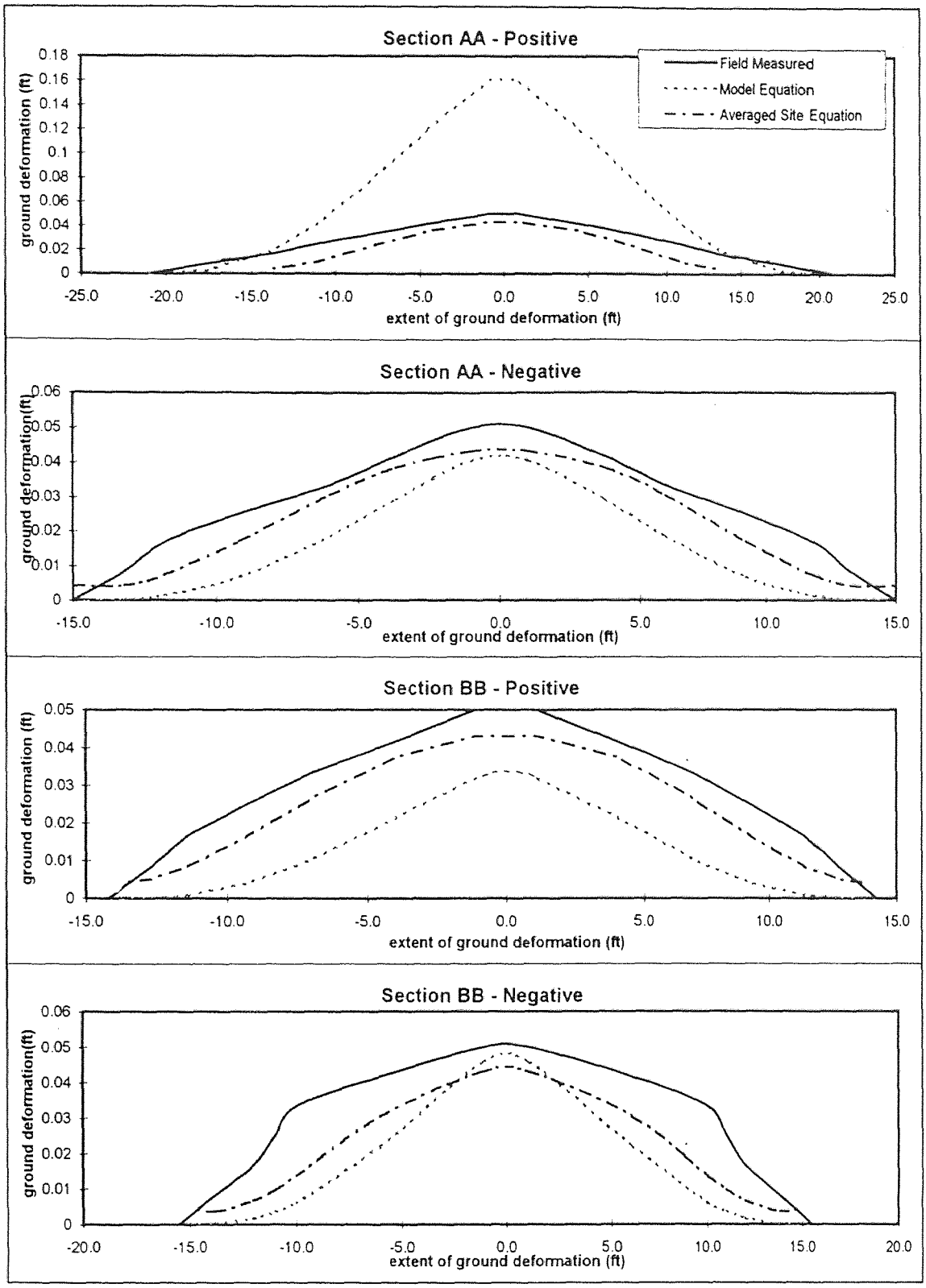

Figure A.12 Comparative Plot - Marcus Hook, PA Site, FW3-Inj.#4.

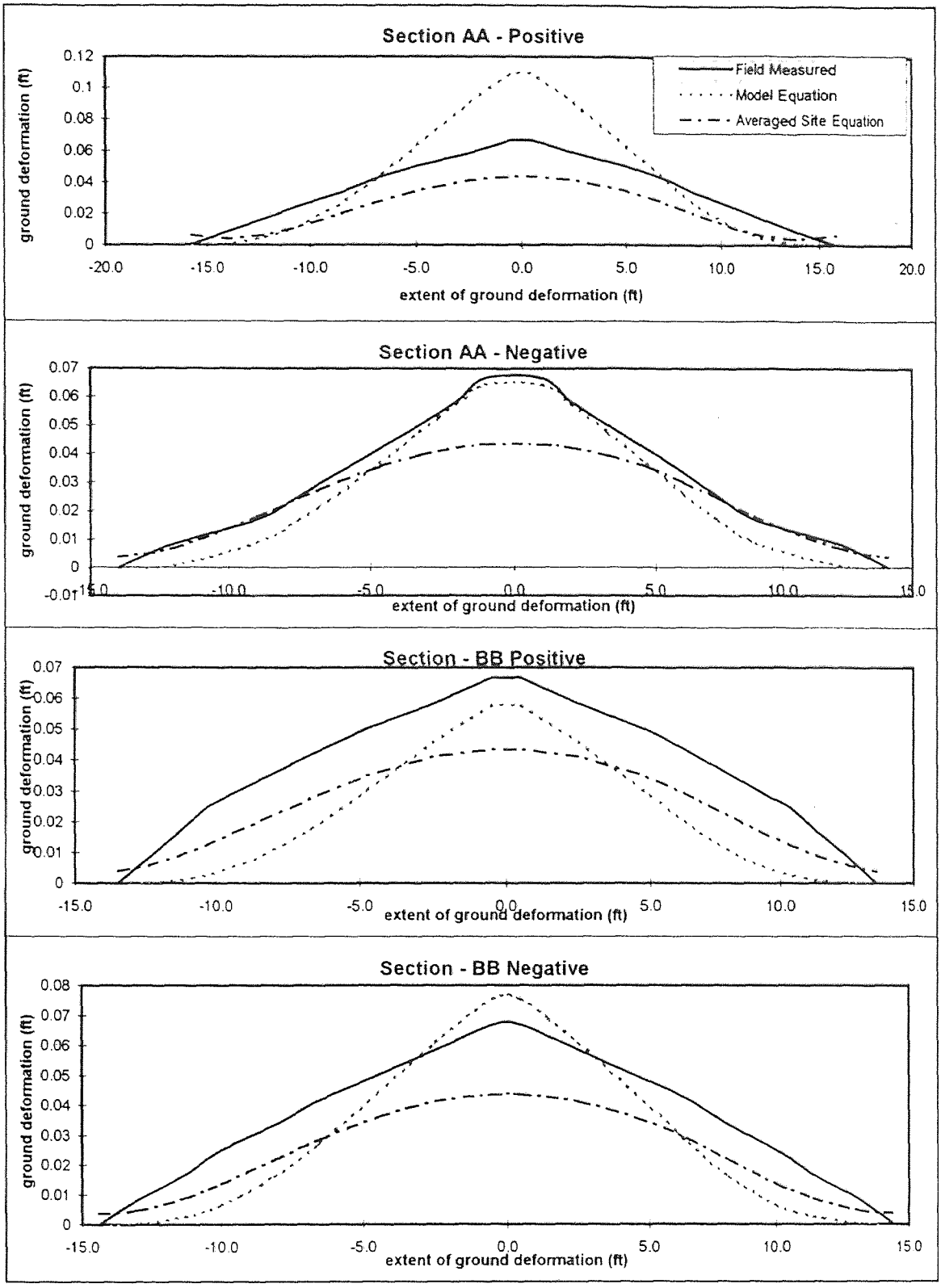

Figure A.13 Comparative Plot - Marcus Hook, PA Site, FW3-Inj.#5.

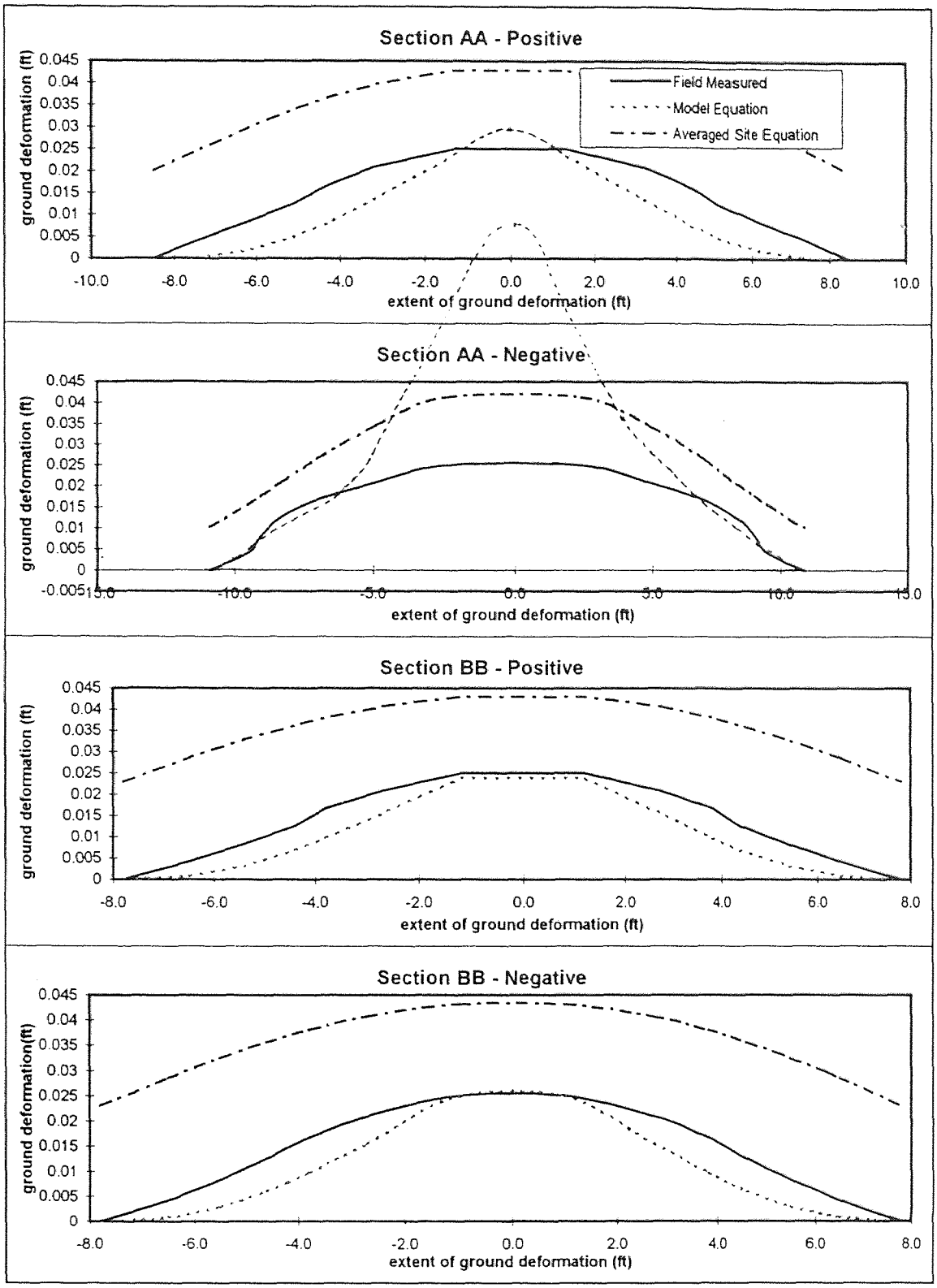

Figure A.14 Comparative Plot - Marcus Hook, PA Site, FW1-Inj.#3.

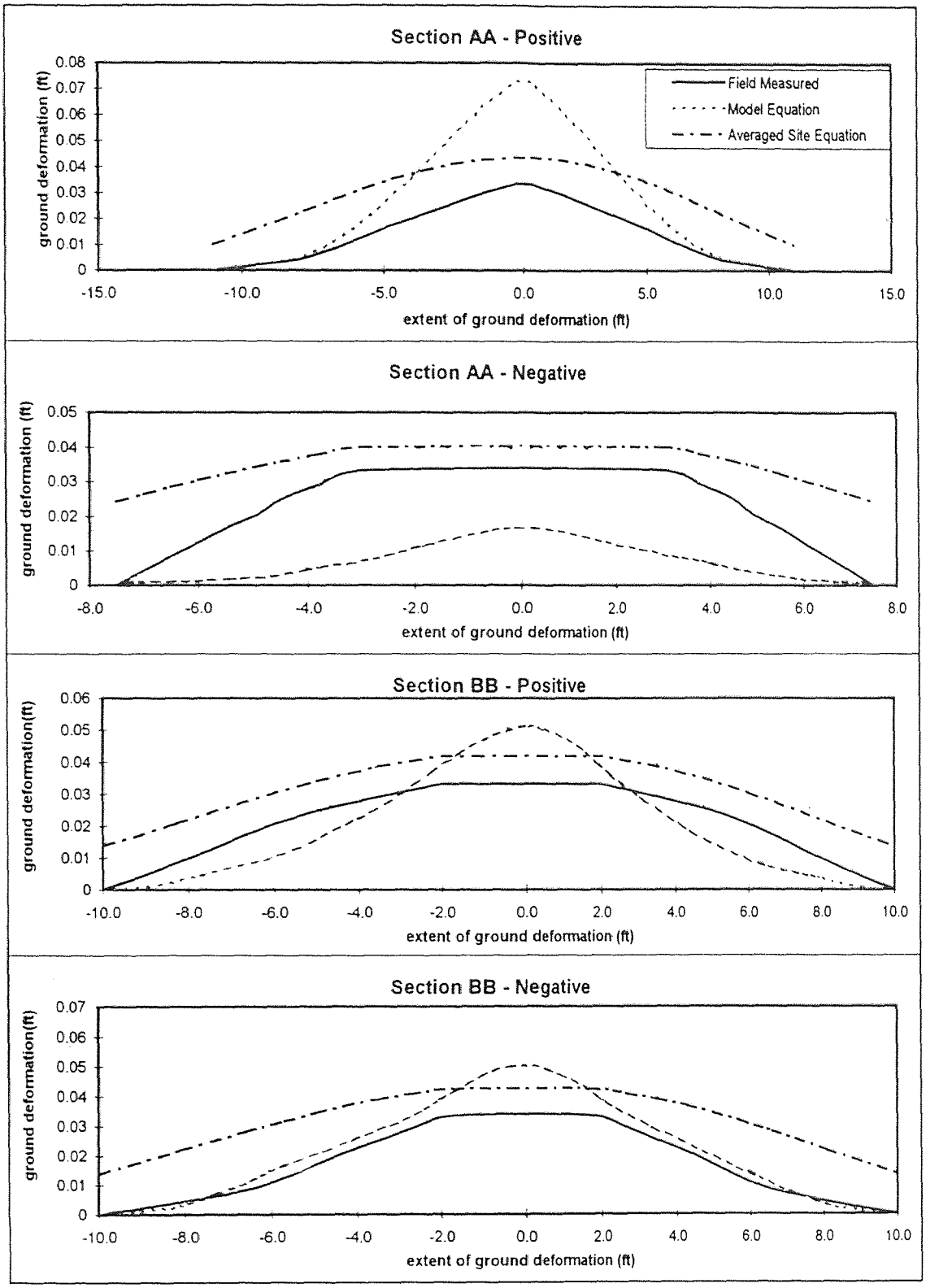

Figure A.15 Comparative Plot - Marcus Hook, PA Site, FW2-Inj.#5.

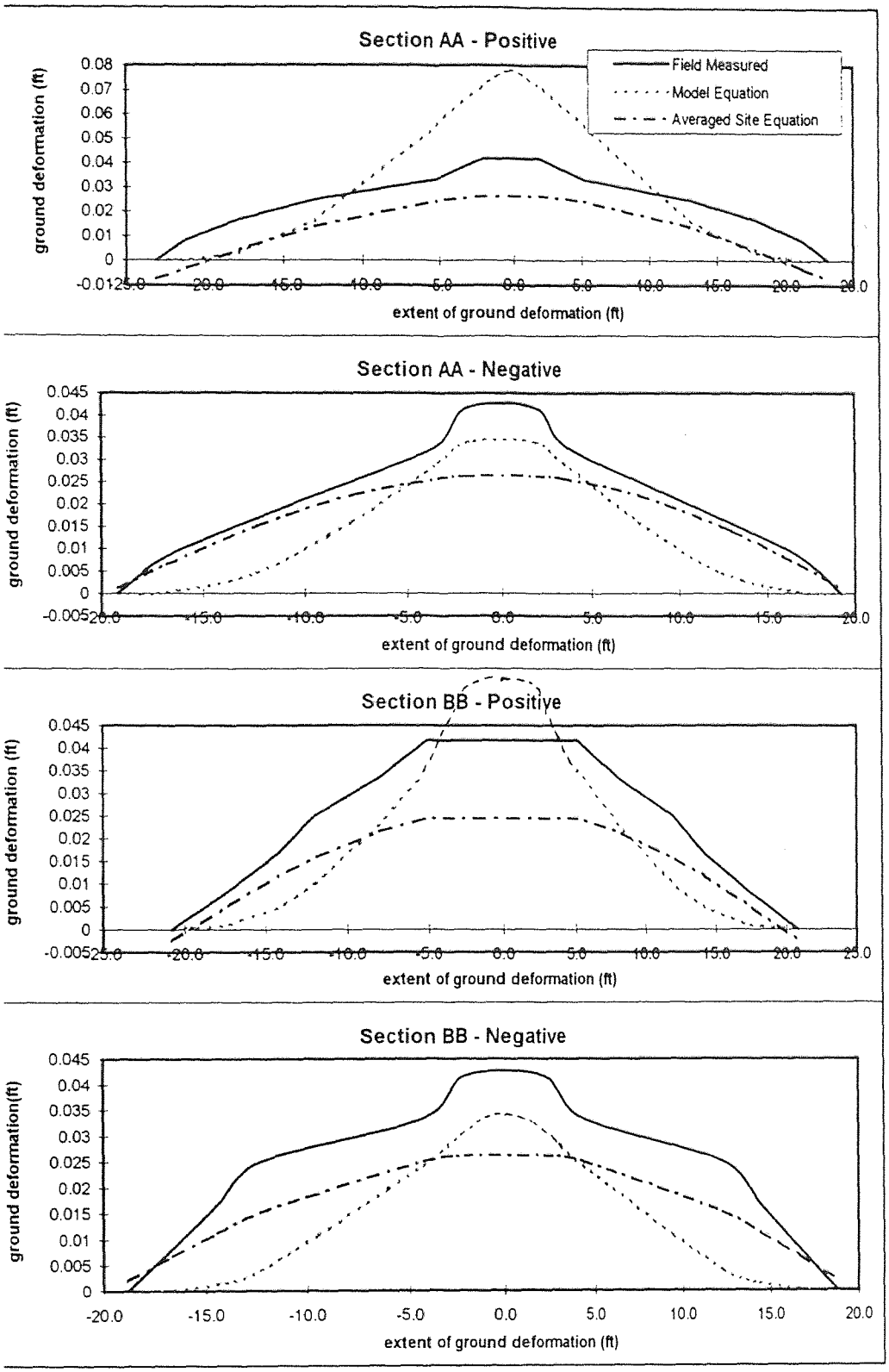

Figure A.16 Comparative Plot - Oklahoma Site, SWT5, Inj.#1.

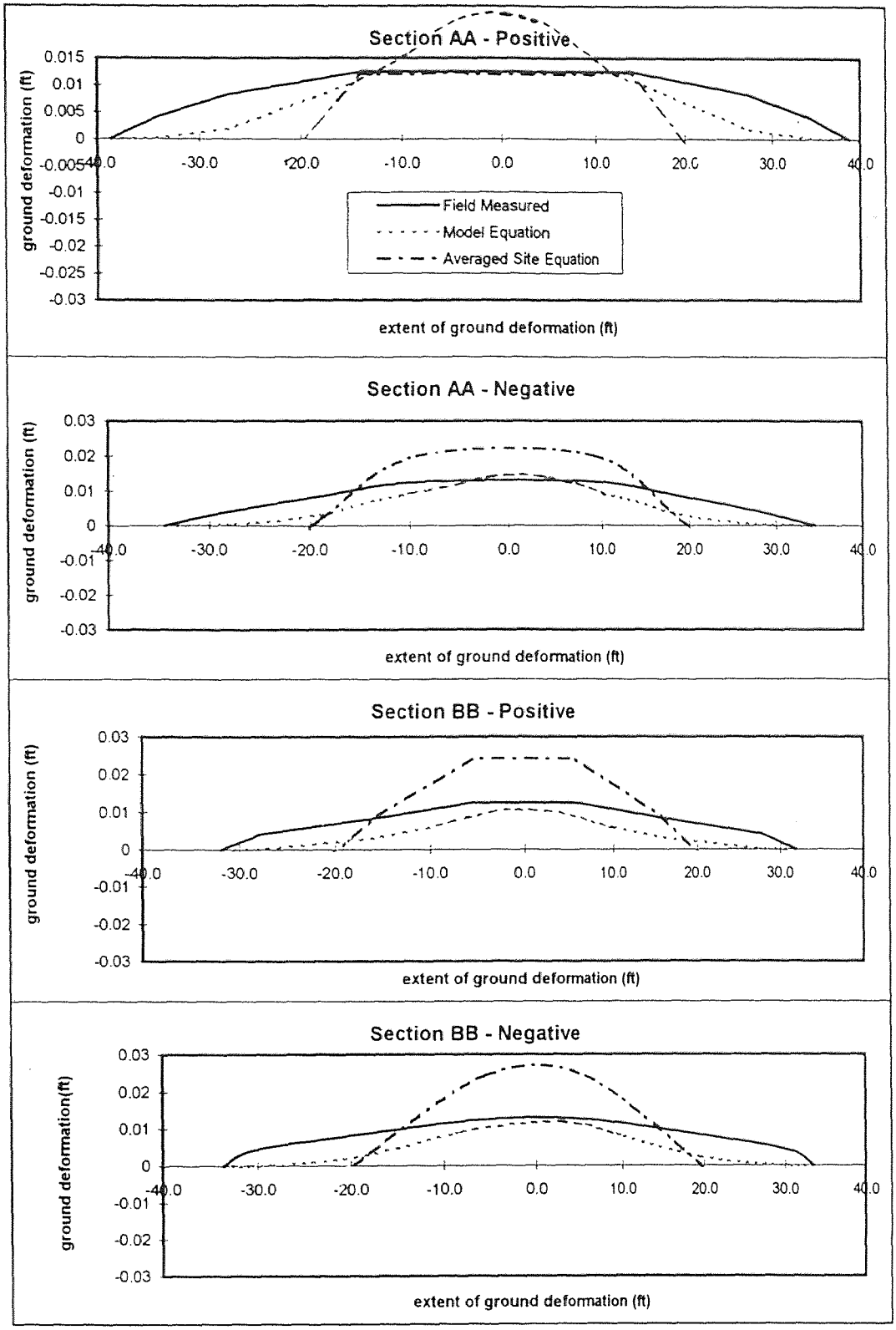

Figure A.17 Comparative Plot - Oklahoma Site, SWT6, Inj.#4.

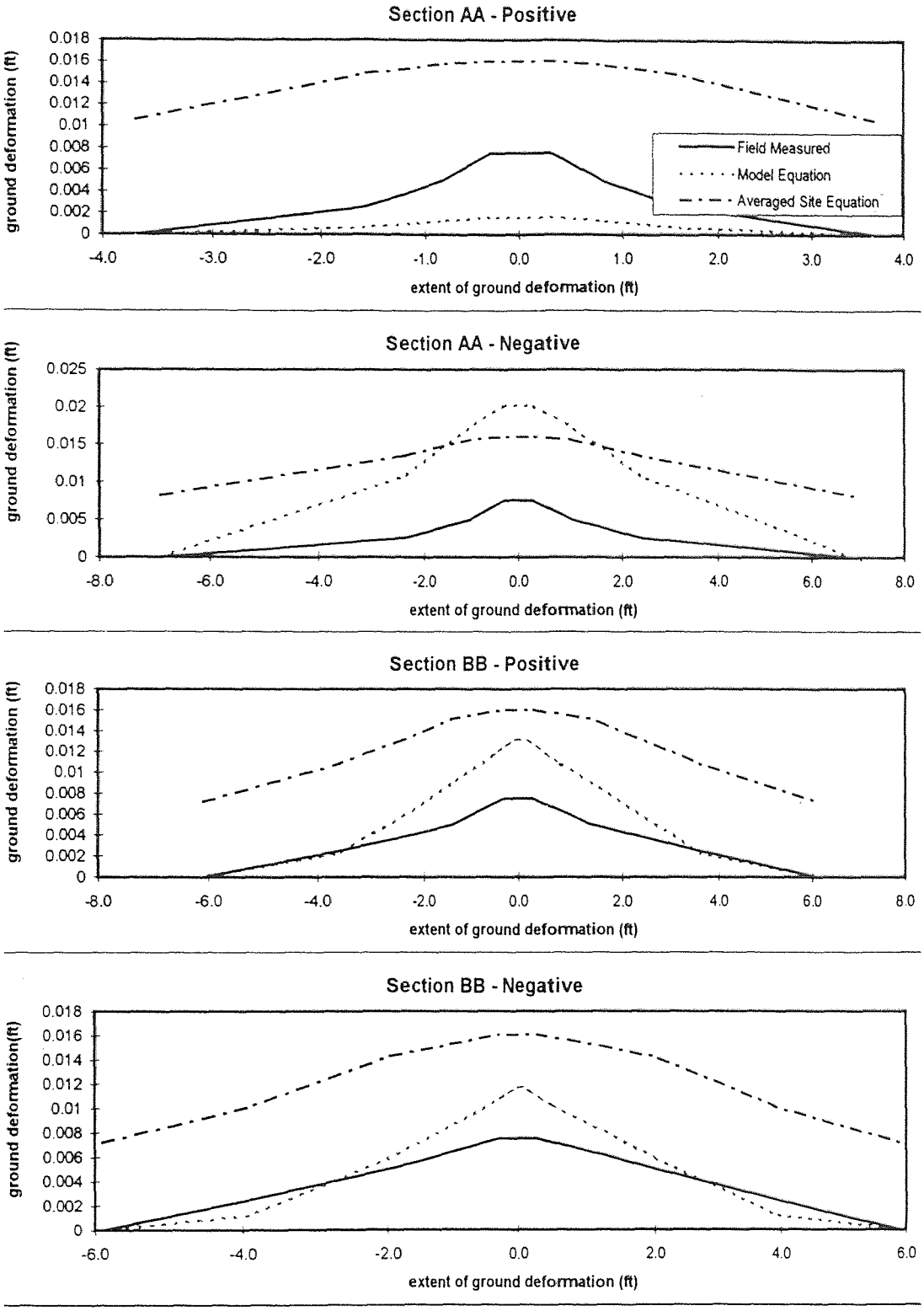

Figure A.18 Comparative Plot - Frelinghuysen, NJ Site, (Fig.A13).

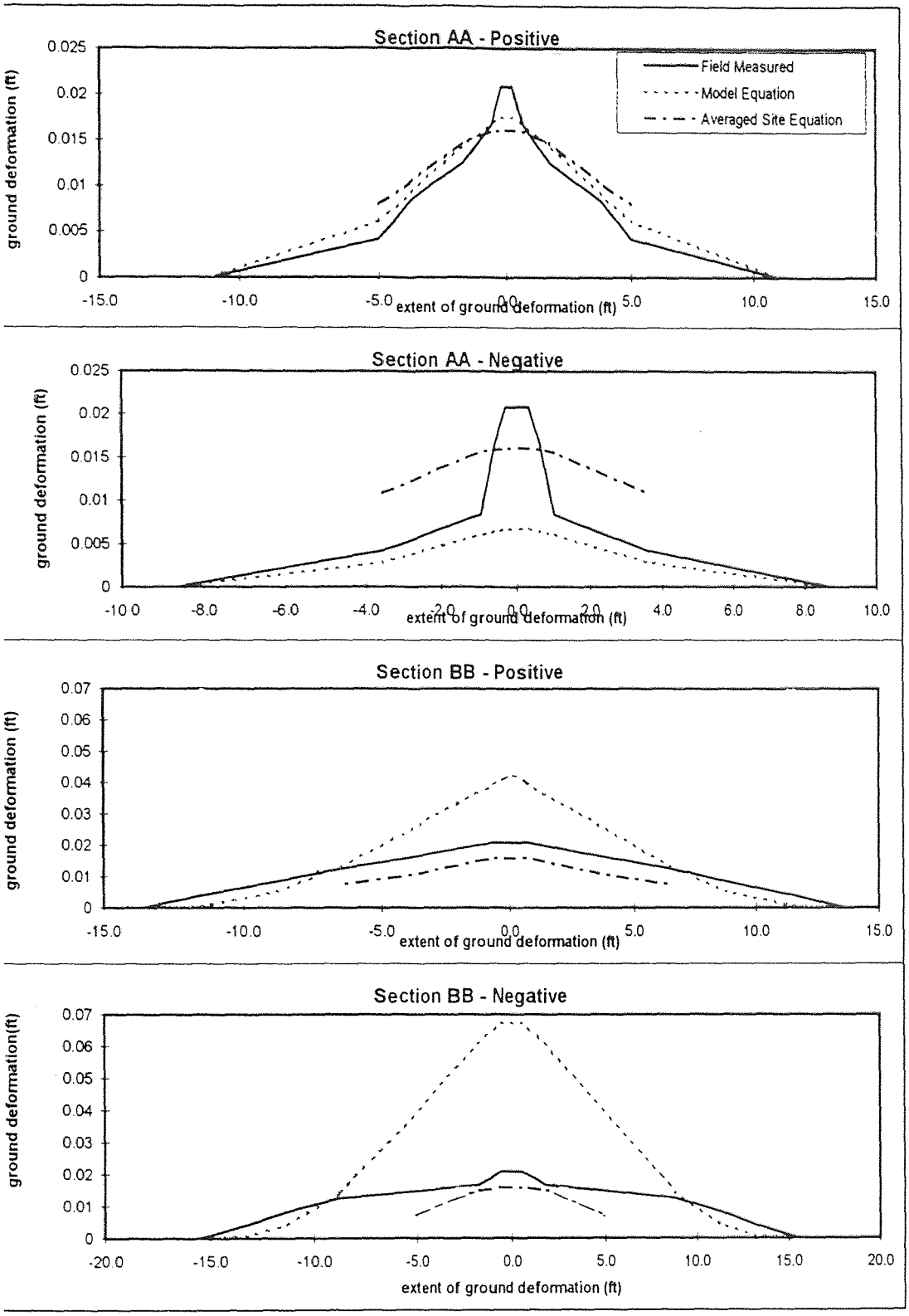

Figure A.19 Comparative Plot - Frelinghuysen, NJ Site, (Fig.A14).

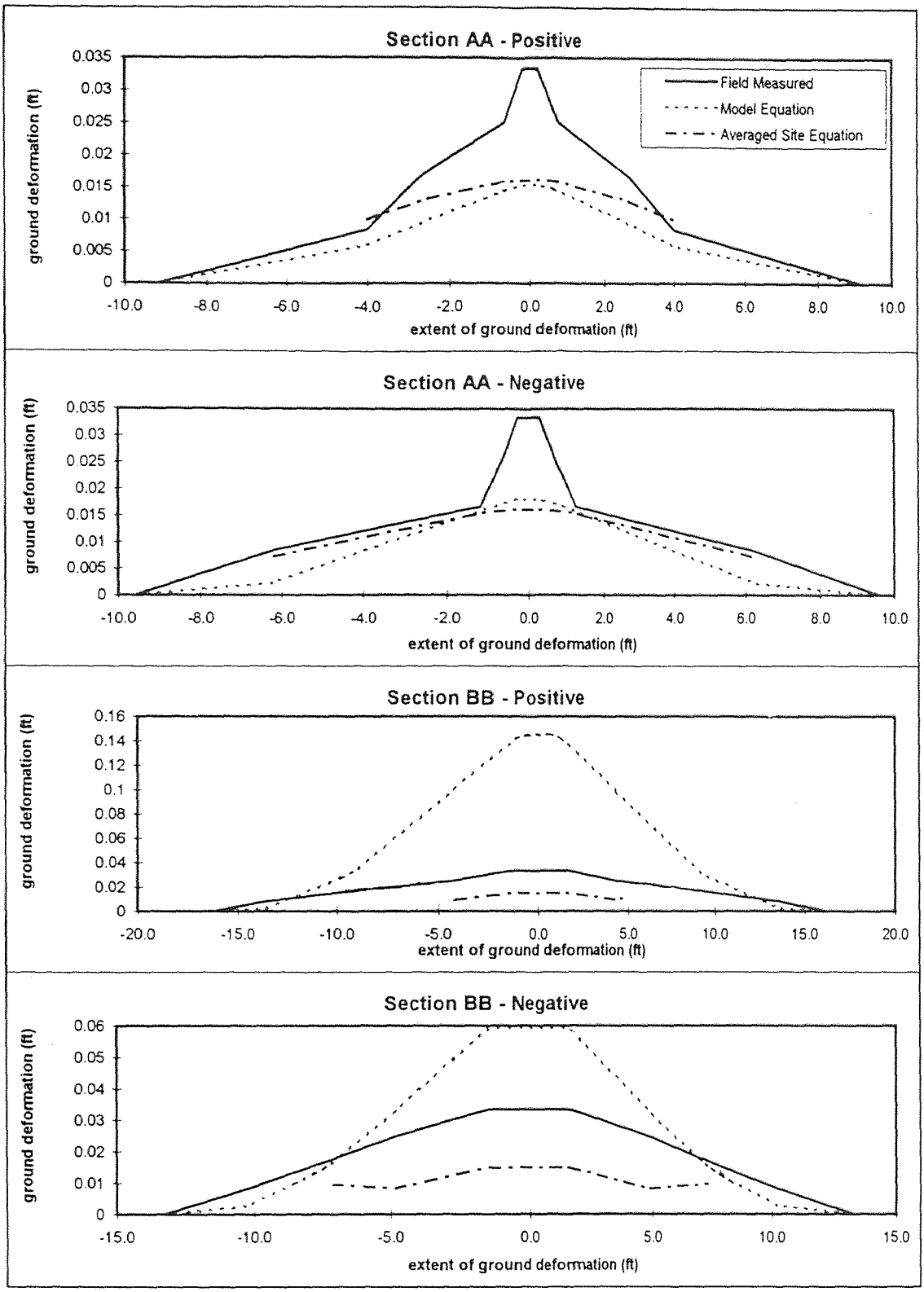

Figure A.20 Comparative Plot - Frelinghuysen, NJ Site, (Fig.A17).

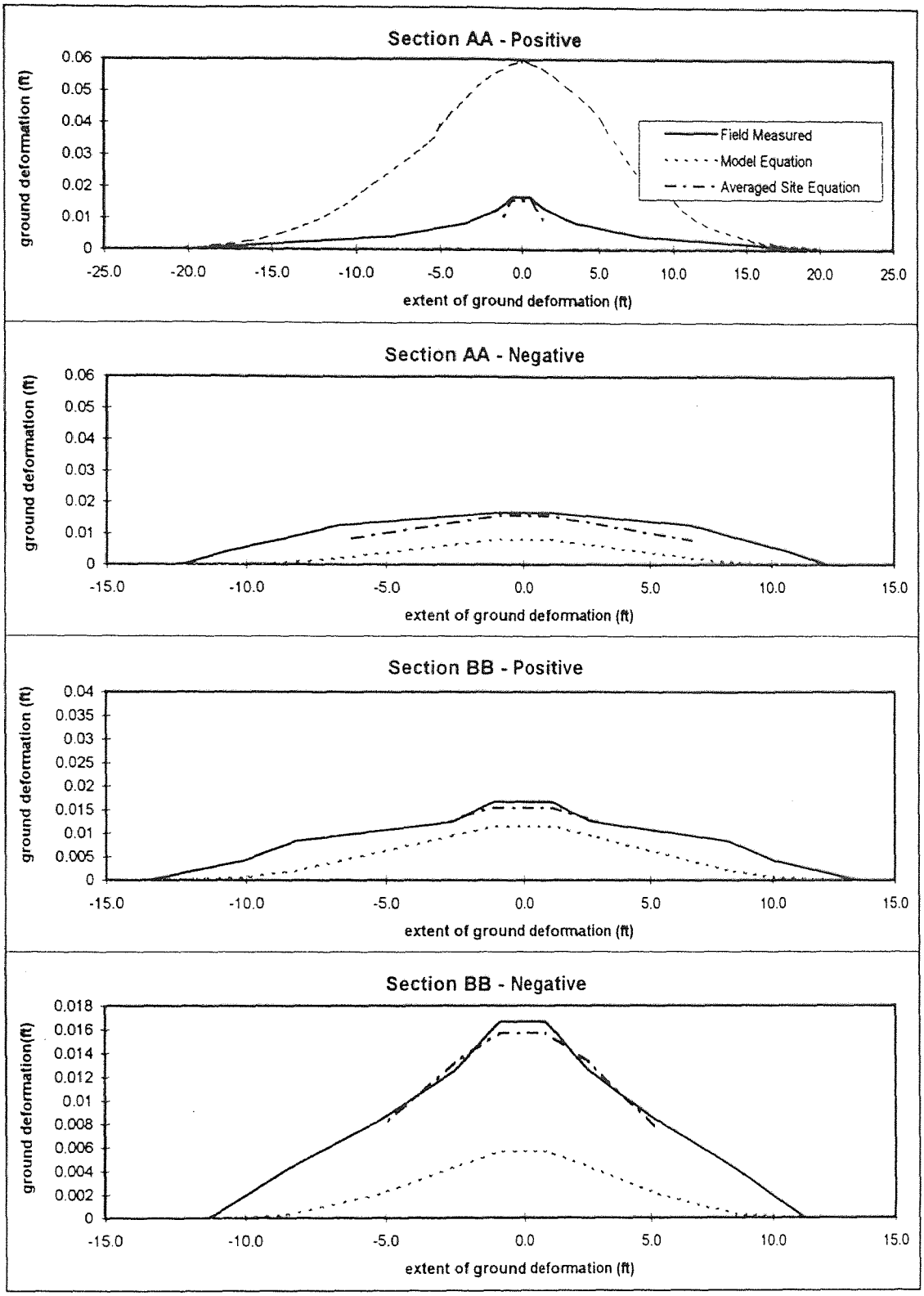

Figure A.21 Comparative Plot - Frelinghuysen, NJ Site, (Fig.A21).

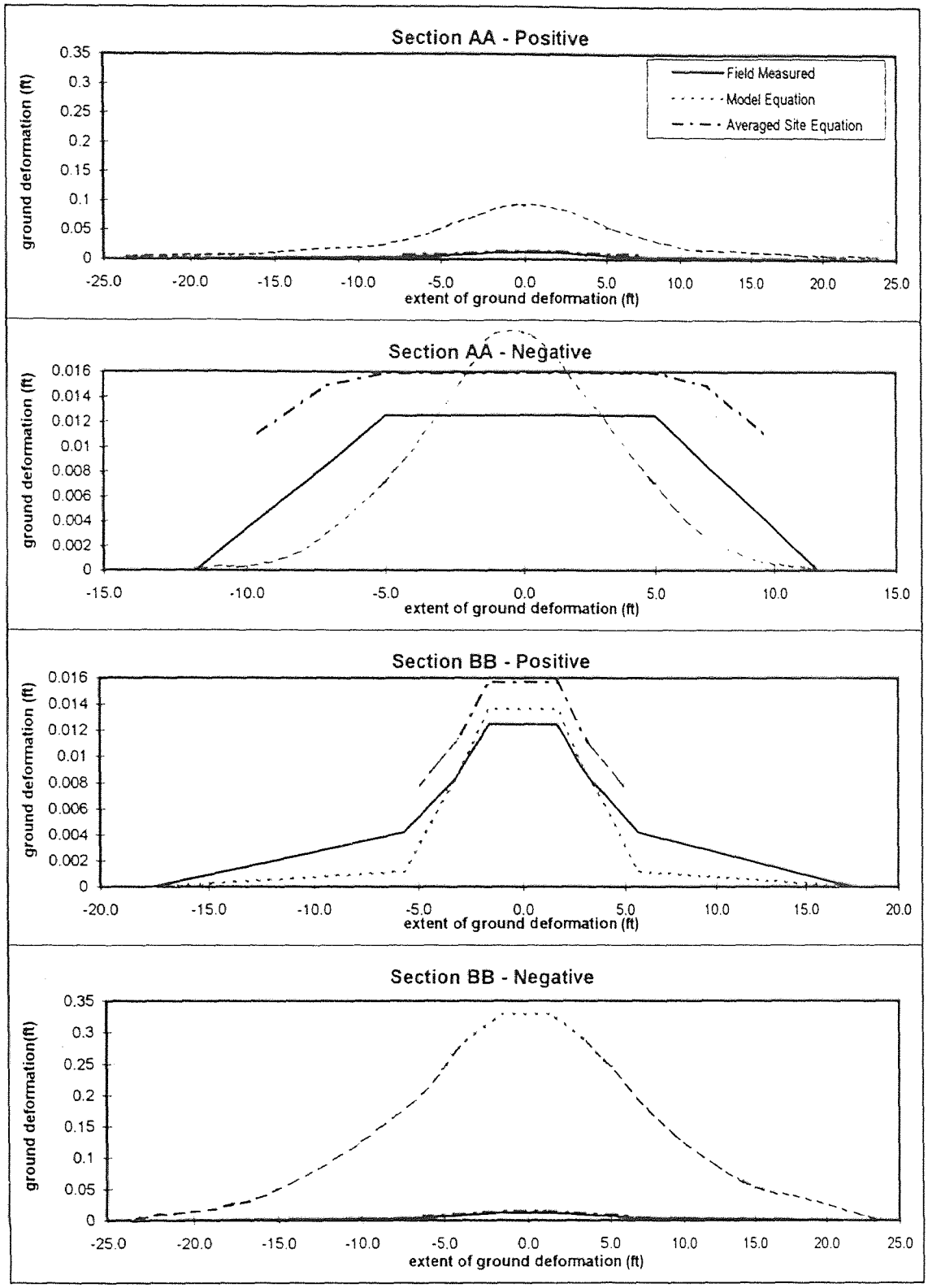

Figure A.22 Comparative Plot - Frelinghuysen, NJ Site, (Fig.A22).

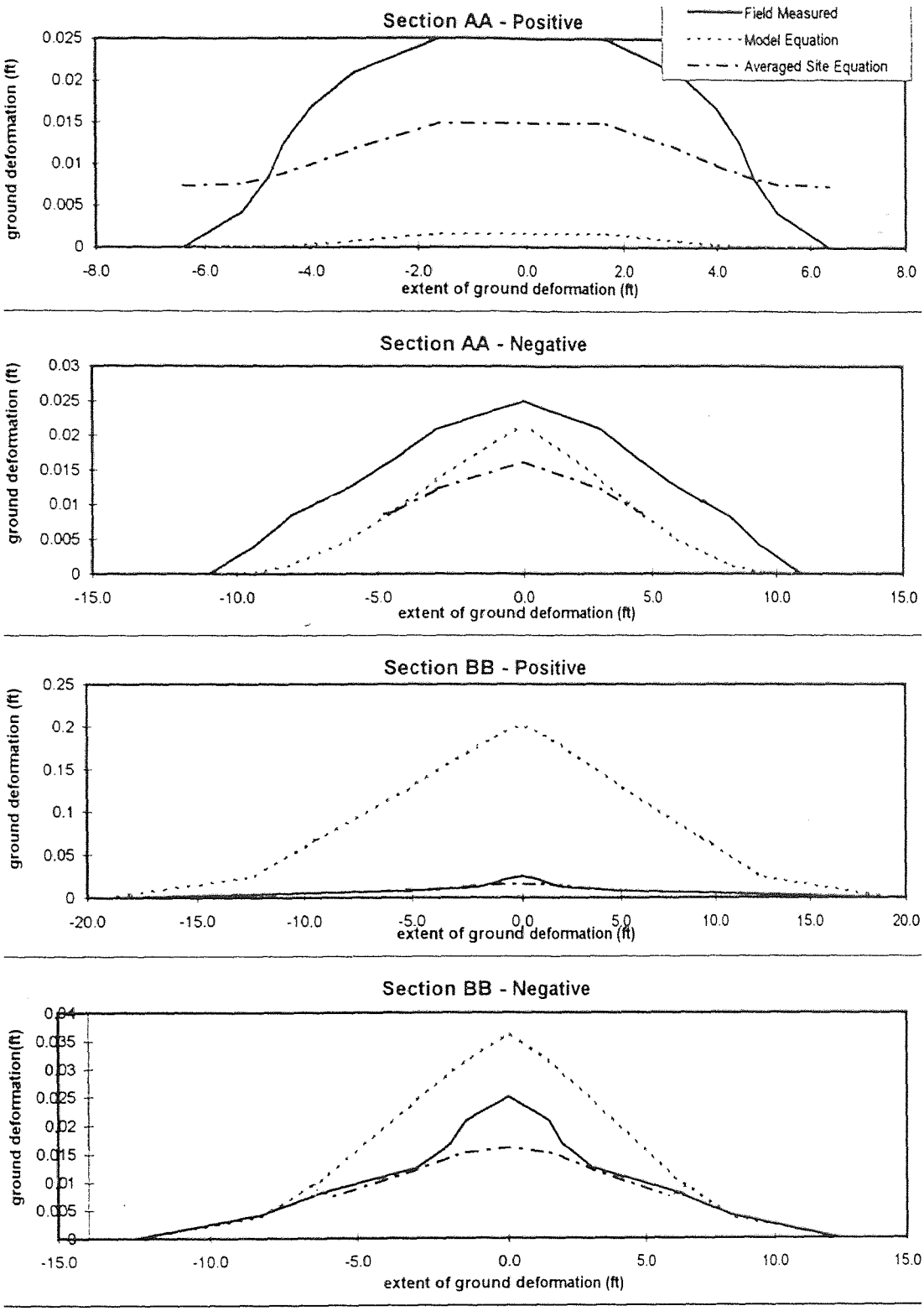

Figure A.23 Comparative Plot - Frelinghuysen, NJ Site, (Fig.A23).

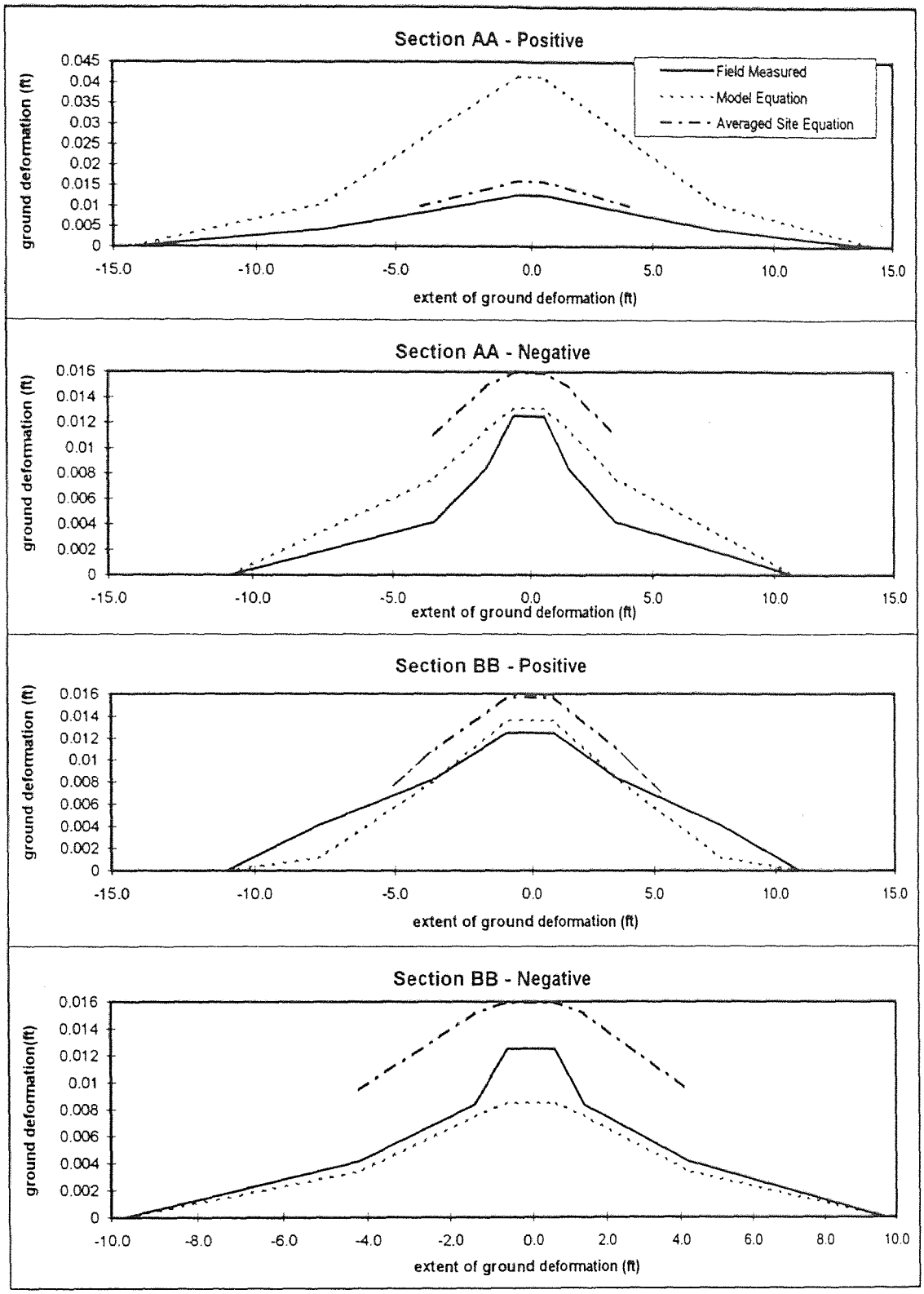

Figure A.24 Comparative Plot - Frelinghuysen, NJ Site, (Fig.A24).

APPENDIX B

INSTRUMENTATION USED FOR FIELD TESTS

The most reliable way to evaluate the effect of pneumatic fracturing on overlying structures is to monitor their movements during actual injections. This permits direct study of structural effects by pneumatic fracturing, and allows comparison of measured response with that predicted by the current design model.

A variety of electronic, optical, and mechanical instruments are available for measurement of deformation and stress. The five types of instrumentation systems used for pneumatic injection monitoring are:

- electronic bonded metallic foil grid resistance **strain gages**,
- biaxial **tiltmeters** with electrolytic level transducers,
- electronic linear variable displacement transducers **(LVDTs)**, and
- optical **engineering levels** with graduated heave rods.
- custom fabricated aluminum **reference beam** system (measures displacement)

Each instrumentation system has its advantages, as well as its limitations, but collectively provide a reliable depiction of building movement. The following five sections discuss the concept and function of each instrument, as well as the information each provides.

B.1 Electronic Bonded Metallic Foil Grid Resistance Strain Gages

Electronic strain gages are used to provide a dynamic time-history of the stresses in

structural steel columns and beams both during and after the fracturing event. Since stress cannot be measured directly, it must be computed from strain measurements. Assuming that deformations are within the elastic range, stress can be computed directly using the modulus of elasticity, E, as seen by the following expression:

$$\sigma = E \cdot \varepsilon \qquad \text{(B.1)}$$

where E is the modulus of elasticity which is assumed to be 29,000,000 psi for steel; and ε represents strain which is equal to $\Delta L_l/L_l$, with L designating member length.

Strain measurement is made possible since the metallic foil in a strain gage changes electrical resistance as it deforms (i.e., it is *piezoresistive*). Strain is then calculated as follows:

$$\varepsilon = (\Delta R_E/R_E) \cdot (1/GF) \qquad \text{(B.2)}$$

where ΔR_E represents the change in electronic resistance of the gage, R_E is the initial unstrained gage resistance, and GF is the gage factor. The gage factor depends on the foil type and thickness, and will vary slightly for each manufactured production lot.

Proper installation of bonded strain gages is essential if good results are to be obtained. The five general steps of installation are: (1) surface preparation, (2) bonding, (3) connection, (4) waterproofing, and (5) physical protection (Dunnicliff, 1988). Steps (1) to (3) are required, but steps (4) and (5) may be omitted based on the gage application as recommended by the gage manufacturer. To insure proper installation, gages should be checked electrically for proper response using a circuit tester.

For most projects, single grid, 120 ohm bonded foil resistance gages are installed on structural steel members adjacent to the injection well. These gages generally have a gage factor of approximately 2.085, an accuracy on the order of ±5 microstrain, and are self-temperature compensated for steel (based on the specific thermal expansion coefficient of steel) .

The measurement method used with these gages is a Wheatstone bridge network system, which has outstanding sensitivity for measuring very small resistance changes. The total strain is represented by the difference between the output voltage, V_O, from the input voltage, V_I. In theory, the strain gage resistance, R_g, is the only resistor in the circuit that varies due to strain changes, but in actuality, the lead wire resistances, R_w, also need to be considered. To avoid lead wire error due to temperature variations, a three-wire, 1/4 bridge network is employed as shown in Figure B.1. Other lead wire errors are minimized by keeping the wires the same length and physically close together.

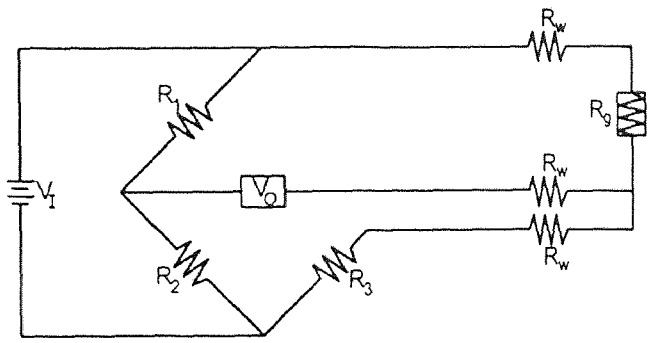

Figure B.1 Three-wire 1/4 Bridge Connection.

The measured voltages are converted to strain using the gage factor. Strain is then simply calculated using the following equation:

$$\varepsilon = (-4 \cdot V_r)/[GF \cdot (1 + 2 \cdot V_r)] \qquad (B.3)$$

where V_r is the difference of the V_O/V_I ratios from the unstrained to strained states as calculated from $V_r = [(V_O/V_I)_{strained} - (V_O/V_I)_{unstrained}]$. The output voltages in the unstrained and strained states are the only unknowns in Equation B.3. A typical plot of the measured microstrain, $\mu\varepsilon$, versus time for an actual pneumatic fracturing event is illustrated in Figure B.2.

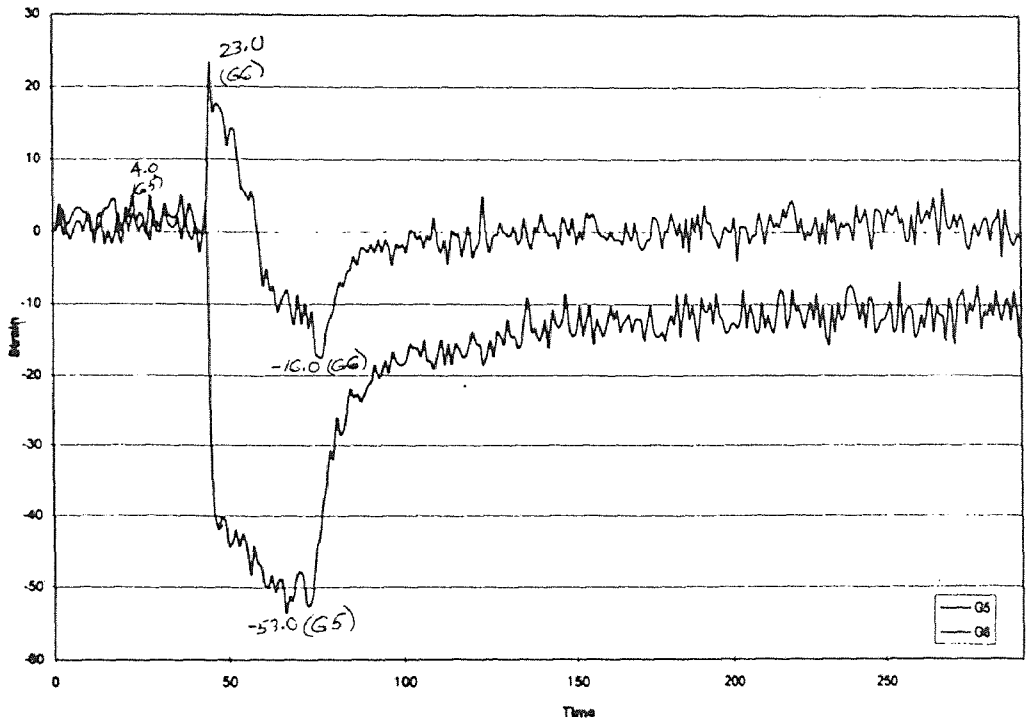

Figure B.2 Plot of a Strain vs. Time Record for Fracture No. 1, Highland Park, NJ, August 3, 1995 (Strain Gages G5 and G6 mounted on Column C8).

After installation of the strain gages, the monitored data is recorded using an Elexor XL-1900 data logger controlled by a Toshiba laptop personal computer. This data logging system allows for rapid compilation of strain gage data, compensation for nonlinearities in electrical output, and data storage for multiple gages. The sampling rate for most field applications is usually 2 times per second which provides an excellent record

of the measured time history. Strain measurements are usually made for a total of three to five minutes which allowed capture of the fracturing event (approximately 15 seconds) and also several minutes of residual movement.

B.2 Biaxial Tiltmeters

Electronic tiltmeters were chosen to provide a dynamic time-history of ground surface deformation which occurs around the fracturing well during injection. Tiltmeters function by sensing a change in tilt angle on the surface on which they are installed using an electrolytic level transducer, in a manner similar to a carpenter's level. Biaxial tiltmeters provide tilt along two axes which can then be used to develop contour maps of ground surface heave at any sampling time during the fracturing event. Since tiltmeters only measure tilt and not actual displacement, they must be "zeroed" with either LVDTs or engineering levels and graduated heave rods. A sample contour map of surface heave is presented in Figure B.3.

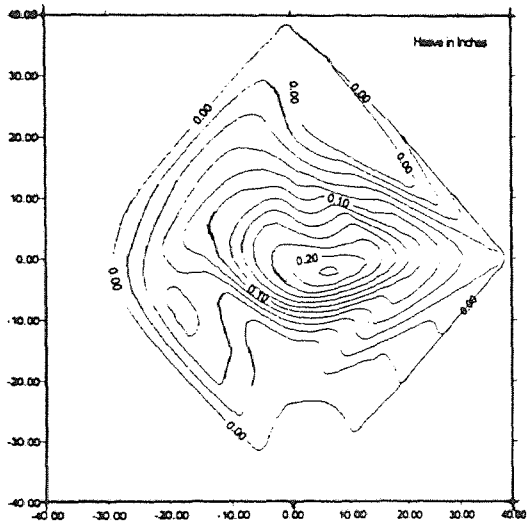

Figure B.3 Surface Heave Contour Map for Fracture Injection No. 1, Highland Park, NJ (at 4.5 seconds into the injection).

Tiltmeters are usually placed on the ground surface in a radiating pattern around the fracture well in four orthogonal directions. The tiltmeters used by the pneumatic fracturing research team are Model No. 701-2 Platform Tiltmeters manufactured by Applied Geomechanics, Inc. (AGI) of Santa Cruz, California. The instruments have a sensitivity range of 0.6 arc seconds to 3 degrees at high gain, and a noise level of approximately 2 arc seconds (King, 1993). Each biaxial tiltmeter contains two electrolytic sensors which measure the tilt angle in the X- and Y- axes, respectively, as depicted in Figure B.4.

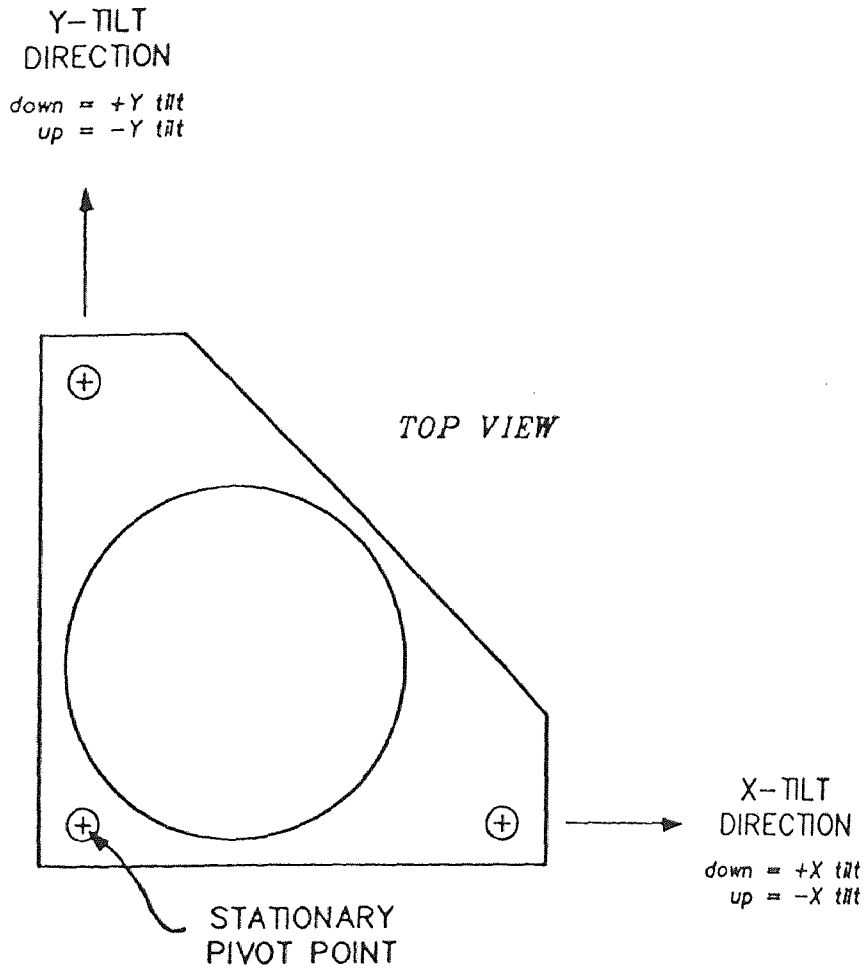

Figure B.4 Sign Convention for Measurement of Platform and Floor Mount Tiltmeter Movements (after Applied Geomechanics, 1991).

The tiltmeters are leveled roughly using a spirit level, followed by final leveling with a digital voltage readout unit (AGI Model 771) to obtain values of approximately zero volts for each electrolytic level. Platform tiltmeters must be placed on a hard clean surface, so when one is not available, square plywood or masonry platforms are used to provide an adequate base. The electrolytic level sensors are electrical metal-film type resistors that produce changes in resistance in response to sensor rotation. The actual output from the tiltmeter is in millivolts which is converted into tilt angle as the following equation illustrates:

$$\theta = V_m \cdot SF \qquad (B.4)$$

where θ is the tilt angle in degrees, V_m is the measured output voltage in millivolts, and SF is a scale factor which differs for each tiltmeter and has the units of microradians per millivolts (μradians/mV).

Tiltmeter data were collected using an Elexor XL-1900 data logger controlled by a Toshiba laptop computer. The sampling rate used for the tiltmeters is generally 2 times per second, depending on test objectives and available memory. To establish baseline behavior of the tiltmeters and check for sensor stability, a three to five minute sampling period is generally used which starts before and continues after each fracture. The tilt measurements recorded throughout the fracturing event are later plotted graphically using Microsoft Excel to identify maximum and residual heave at each tiltmeter location. Appropriate event times are then chosen to develop contour maps of ground surface heave to show the progression of the fracture. These maps are developed using proprietary software from AGI and the Surfer program by Golden Software, Inc.

B.3 LVDTs (Linear Variable Displacement Transducers)

LVDTs were chosen to provide a dynamic time-history of changing ground displacement at various points adjacent to the fracture injection well. LVDT data are used to calibrate the tiltmeters and to provide measurement of the heave magnitude at selected points. LVDTs are typically suspended from an aircraft cable which is anchored at two locations outside of the area affected by fracturing. The spring loaded plungers of the LVDTs are then extended to contact the ground surface.

The LVDTs used on projects by the pneumatic fracturing research team are Models DCT1000A, DCT2000A, and DCT4000A, manufactured by RDP-Electrosense, Inc. of Pottstown, PA. The usable displacement range for these models is ±1.0 in., ±2.0 in., and ±4.0 in., respectively. The LVDTs have an accuracy for linear displacement of ±0.5% and the spring rate of the measuring plunger is 4 ounces/inch. Like the tiltmeters, the LVDTs are generally placed in a radiating pattern around the fracture well.

Each LVDT contains an axially positioned plunger inside of three transformer coils symmetrically spaced. At zero displacement, two of these coils have equal induced voltages, but when the plunger is displaced, the voltage in one coil will decrease and the other will increase. The difference between these two voltages, V_d, is directly proportional to the displacement of the plunger and is determined using the relationship:

$$V_d = STF \cdot M_s \qquad (B.5)$$

where STF is the step factor which is unique for each LVDT in volts/step, and M_s is the measured voltage increase in steps. The displacement, w, is then calculated as follows:

$$w = V_d \cdot CF \tag{B.6}$$

where CF is a calibrated conversion factor which changes volts into inches.

For data collection, the LVDTs are connected to an Elexor XL-1900 data logger controlled by a Toshiba laptop computer. The sampling rate for the LVDTs is usually 2 times per second during the fracturing event to be consistent with the other electronic monitoring equipment. Data are later reduced by graphing a displacement time-history plot with Microsoft Excel. A typical plot of heave versus time for a fracture injection is shown in Figure B.5.

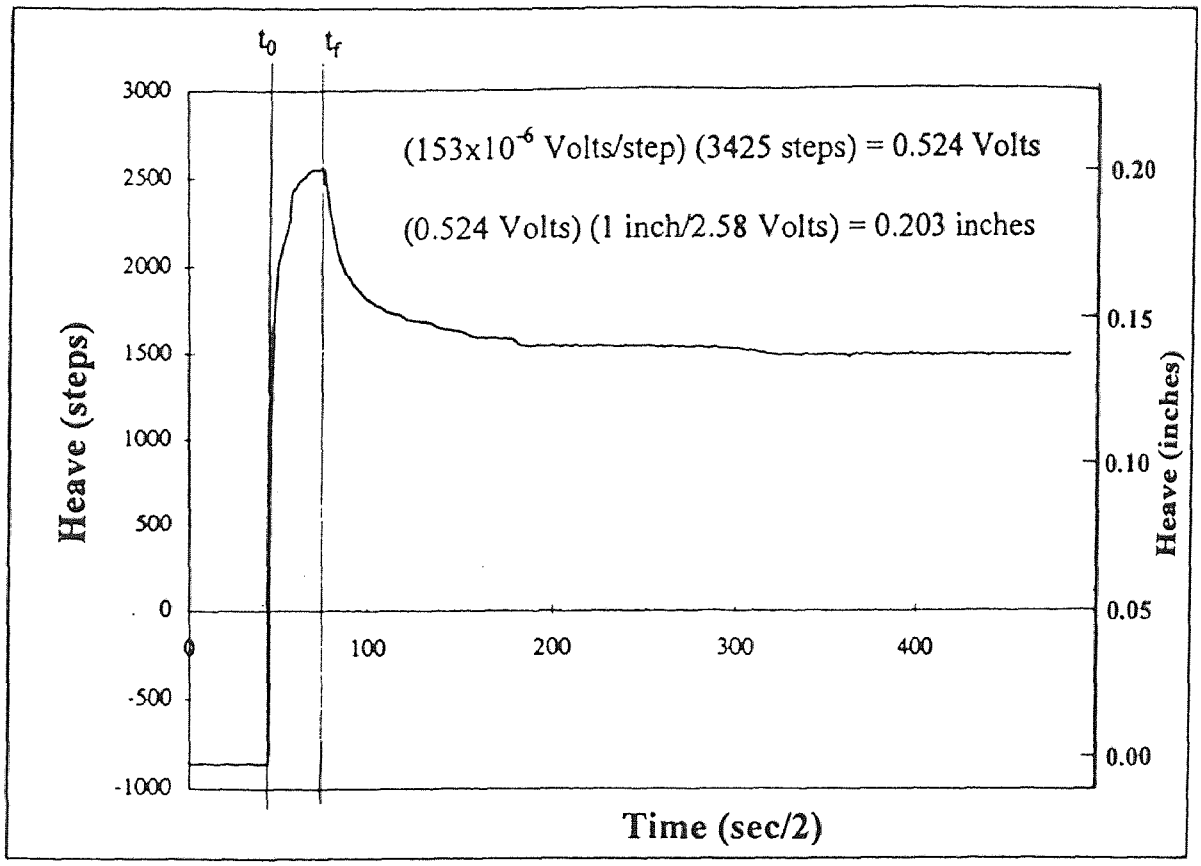

Figure B.5 LVDT Plot of Heave vs. Time for Fracture No. 1, Highland Park, NJ.

B.4 Optical Engineering Levels with Graduated Heave Rods

Engineering levels are used to measure the vertical displacement at the base of structural steel columns, masonry walls, and other selected locations adjacent to the fracture injection well. The levels are sighted on graduated heave rods which can be either attached to column base plates, bolted directly to a structural member, or placed on the ground surface. The main disadvantage of this measuring system is that only maximum heave can be recorded by the level operator.

B.5 Aluminum Reference Beam

Before electronic tiltmeters were utilized for monitoring heave, the pneumatic fracturing surface deformations were monitored using a custom fabricated reference beam system. The reference beam provided a comprehensive mechanical method for monitoring surface heave deformation at multiple locations around the injection well. Figure B.6 illustrates an elevation, plan, and section of the components of the custom reference beam system. As the figure illustrates, heave measurements are made at 1-foot intervals throughout the length of the beam by sliding heave rods with rubber indicators. In addition, the ends of the reference beams were monitored separately using engineering levels and the heave rod measurements were then adjusted based on the tilt angle between the beam ends. The geologic mediums are elastic, so they will tend to absorb some of the heave as elastic strain. Therefore, the measured ground deformation presumably represents the lower limit of the fracture aperture and radius (King, 1993). An obvious limitation to this system is its inability to record surface deformations throughout the time history of the fracturing event. Residual heave is also left unmeasured, because the system only allows for measurement of the maximum surface heave values.

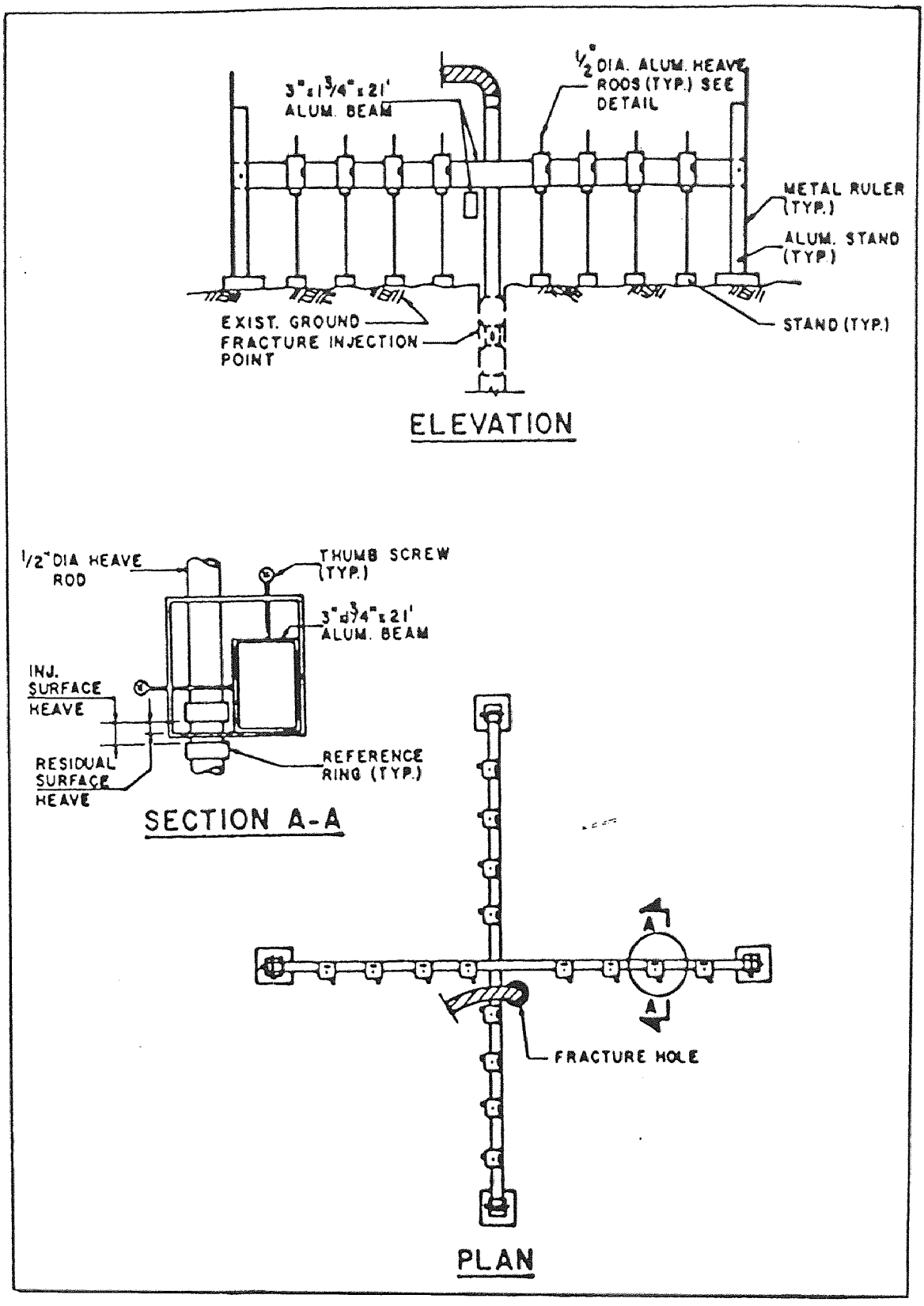

Figure B.6 Custom Aluminum Reference Beam System (after King, 1993).

APPENDIX C

STRESS-STRAIN ANALYSIS LOAD CALCULATIONS

C.1 Field Test Strain Measurements

Maximum Strain/Stress Determination:

G17 and G18

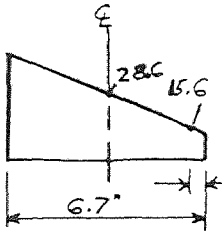

$\varepsilon_{max} = 42.4\ \mu$
$\varepsilon_{min} = 14.8\ \mu$
$\sigma_{max} = 1229.6$ lbs/in.^{2}
$\sigma_{min} = 429.2$ lbs/in.^{2}

G11 and G12

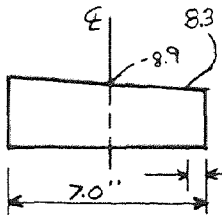

$\varepsilon_{max} = -9.5\ \mu$
$\varepsilon_{min} = -8.3\ \mu$
$\sigma_{max} = -275.5$ lbs/in.^{2}
$\sigma_{min} = -240.7$ lbs/in.^{2}

G9 and G10

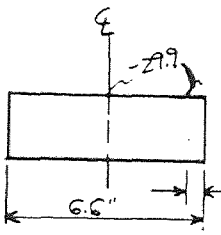

$\varepsilon_{max} = -29.9\ \mu$
$\varepsilon_{min} = -29.9\ \mu$
$\sigma_{max} = -867.1$ lbs/in.^{2}
$\sigma_{min} = -867.1$ lbs/in.^{2}

G5 and G6

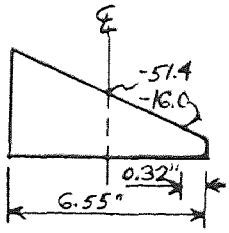

$\varepsilon_{max} = -90.6\ \mu$
$\varepsilon_{min} = -12.2\ \mu$
$\sigma_{max} = -2627.4$ lbs/in.^{2}
$\sigma_{min} = -353.8$ lbs/in.^{2}

Residual Strain/Stress Determination

G17 and G18

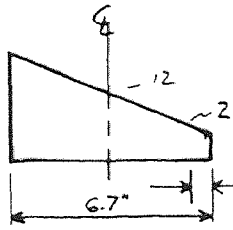

$\varepsilon_{max} = 22.6\ \mu$
$\varepsilon_{min} = 1.4\ \mu$
$\sigma_{max} = 655.4$ lbs/in.^{2}
$\sigma_{min} = 40.6$ lbs/in.^{2}

G11 and G12

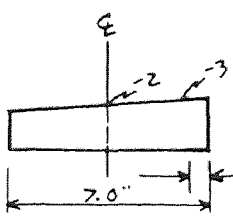

$\varepsilon_{max} = -3.1\ \mu$
$\varepsilon_{min} = -0.9\ \mu$
$\sigma_{max} = -89.9$ lbs/in.^{2}
$\sigma_{min} = -26.1$ lbs/in.^{2}

G9 and G10

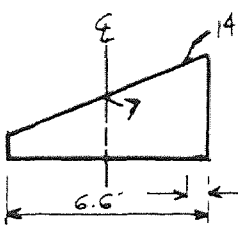

$\varepsilon_{max} = 14.5\ \mu$
$\varepsilon_{min} = -0.5\ \mu$
$\sigma_{max} = 420.5$ lbs/in.^{2}
$\sigma_{min} = -14.5$ lbs/in.^{2}

G5 and G6

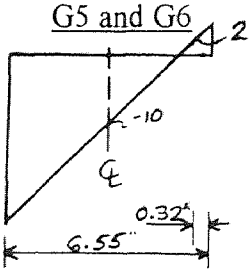

$\varepsilon_{max} = -23.3\ \mu$
$\varepsilon_{min} = 3.3\ \mu$
$\sigma_{max} = -675.7$ bs/in.^{2}
$\sigma_{min} = 95.7$ lbs/in.^{2}

C.2 Calculations of Dead Loads and Live Loads for Section A-A

Calculation of Dead Load for Beams B7 and B8:

Built-up roofing = 6.5 lb/ft^2

2"-thick wood planking (assume Southern Pine = 36 lb/ft^2) =
= (2 in./12 in./ft)·36 lb/ft^2 = 6 lb/ft^2

Wood Purlins (supporting roof decking). Assume these are Southern Pine,
3 in. by 12 in. at 6-foot center-to-center spacing, so
(3 in./12 in./ft)·(12 in./12 in./ft)·(36 lb/ft^2/6 ft) = 1.5 lb/ft^2

Dead Load contribution from the roofing materials =
= 6.5 lb/ft^2 + 6.0 lb/ft^2 + 1.5 lb/ft^2 = **14 lb/ft^2**

Dead Load on Beam 7 (W16x36) using concentrated loads from each pair of purlins)
- purlins are spaced 5.625 ft apart.
(14 lb/ft^2)·(20 ft)·(5.625 ft) = 1575 lb (excluding the beam self-weight)
$D.L._{Beam\ 7}$ = 1575 lb

Dead Load on Beam 8 (W15x35) using concentrated loads from each pair of purlins)
- purlins are spaced 5.74 ft apart at an 18° sloped angle from horizontal.
(14 lb/ft^2)·(20 ft))·(5.74 ft) = 1607.2 lb (excluding the beam self-weight)
$D.L._{Beam\ 8}$ = 1607.2 lb

Calculation of Live Load for Beams B7 and B8, using the Snow Load :

For **$L.L._{Beam\ 7}$**: (30 lb/ft^2)·(20 ft)·(5.625 ft) = **3375 lb**

For **$L.L._{Beam\ 8}$**: (30 lb/ft^2)·(20 ft)·(5.74 ft)·(cos18°) = **3275.4 lb**

Calculation of Dead Load + Live Load for Beams B7 and B8:

Vertical Direction: Beam 7 = 1575 lb + 3375 lb = **4950 lb = Beam $7_{(D.L.+L.L.)}$**

Vertical Direction: Beam 8 = 1607.2 lb + 3275.4 lb = 4882.6 lb = Beam $8_{(D.L.+L.L.)}$

Perpendicular to the Beam: **Beam $8_{(D.L.+L.L.)}$ = (4882.6 lb)·(cos18°) = 4643.7 lb**

Calculation of Loads (D.L.+L.L.) for Columns C7 and C8:

Column C7: Contributory Area = (20 ft)·(22.5 ft/2 + 27.36 ft/2) = 498.6 ft^2

Contribution From:
Beams B17 and B18 = (4950 lb/2) + (4882.6 lb/2) + (10 ft)·(12.25 lb·2) + 201.2 $lb_{for\ B17}$
= 5,362.5 lb

Beam 7 = (36 lb/ft) + (3/2)·(4950 lb) = 7,830.0 lb

Beam 8 = (35 lb/ft) + (2)·(4882.6 lb) = 10,267.4 lb

P_{total} = 23,460 lb (for Column C7)

Column C8: Contributory Area = (20 ft)·(27.36 ft/2) + (20 ft)·(6.5 ft) = 403.6 ft^2

Contribution From:
L.L. and D.L. on diagonal framing side = (20 ft)·(6.5 ft)·(44 lb/ft^2) = 5720 lb

Beam 8 = (35 lb/ft) + (2)·(4882.6 lb) = 10,267.4 lb

Contribution of steel out of plane:
B5 = (10 ft)·(21 lb/ft) = 210 lb
B15 = (1/4)·(16 ft)·(21 lb/ft) = 84 lb
B10 = (10 ft)·(21 lb/ft) = 210 lb
504 lb

Estimated weight of window with frame and parapet above:
(assume glass is 54 inches high, 1/4-in. thick, and 156 lb/ft^3) and
(assume the parapet/corrugated wall 4-ft high and 5 lb/ft^2)

- load due to the glass = (54 in./12 in./ft)·(0.25 in./12 in./ft)·(156 lb/ft^3) = 14.6 lb/ft
- load due to corrugated wall = (5 lb/ft^2)·(4 ft) = 20 lb/ft .....= 20.0 lb/ft
≈ 35 lb/ft
- The total contribution of the upper windows and wall = (35 lb/ft)·(20 ft) = 700 lb

Therefore, the total load for column C8 = 5720 lb + 10,267.4 lb + 504 lb + 700 lb =

P_{total} = 17,191.4 lb (for Column C8)

C.3 Calculations of Estimated Original Design Loads for Section A-A

Calculation of Original Design Stresses for Beam B7:

At the beam center:

$M_{max}= (P\cdot l)/4 + (P\cdot l)/4 + (w\cdot l^2)/8 =$ (based on face-to-face beam length)

$= (4950\ \text{lb}\cdot 262\ \text{in.})/4 + (4950\ \text{lb}\cdot 262\ \text{in.})/4 + (36\ \text{lb/ft}\cdot(262\ \text{in.})^2)/8 = 674{,}191.5\ \text{lb-in.}$

$\sigma_{max} = M\cdot c/I = (674{,}191.5\ \text{lb-in.})\cdot(7.925\ \text{in.})/(446.3\ \text{in.}^4) = \mathbf{11{,}972\ lb/in.^2} = \sigma_{max}$

(this equals 66.5% of the allowable 18,000 lb/in.^{2} used in 1930 for steel design)

At the strain gage locations, G17 and G18:

$M = (3/2\cdot P\cdot x) + (w\cdot l\cdot x)/2 + (w\cdot x^2)/2$ (gages were installed at a distance x = 38.95 in.)

$M = (3/2\cdot 4950\ \text{lb}\cdot 38.95\ \text{in.})+(36/12\ \text{lb/in.}^2\cdot 262\ \text{in.}\cdot 38.95\ \text{in.})/2+(36/12\ \text{lb/in.}^2\cdot 38.95\ \text{in.}^2)/2$

$M = 302{,}235\ \text{lb-in.}$

$\sigma = M\cdot c/I = (302{,}235\ \text{lb-in.})\cdot(7.925\ \text{in.})/(446.3\ \text{in.}^4) = \mathbf{5{,}367\ lb/in.^2} = \sigma_{(at\ G17\ and\ G18)}$

(this equals 29.8% of the allowable 18,000 lb/in.^{2} used in 1930 for steel design)

Calculation of Original Design Stresses for Beam B8:

At the beam center:

w = (35 lb/ft) in the vertical direction,

but w = (35 lb/ft)·(cos18°) = 33.3 lb/ft perpendicular to the beam, so

$M_{max}= (P\cdot l)\cdot(1/5 + 2/5) + (w\cdot l^2)/8 =$ (based on face-to-face beam length)

$= (4643.7\ \text{lb}\cdot 336.75\ \text{in.}\cdot 3/5) + (33.3/12\ \text{lb/in.}\cdot(336.75\ \text{in.})^2)/8 = 977{,}596.6\ \text{lb-in.}$

$\sigma_{max} = M\cdot c/I = (977{,}596.6\ \text{lb-in.})\cdot(7.44\ \text{in.})/(396.7\ \text{in.}^4) = \mathbf{18{,}334.6\ lb/in.^2} = \sigma_{max}$

(this equals 101.8% of the allowable 18,000 lb/in.^{2} used in 1930 for steel design)

At the strain gage locations, G11 and G12:

$M = (2 \cdot P \cdot x) + (w \cdot l \cdot x)/2 + (w \cdot x^2)/2$ (gages were installed at a distance x = 7.2 in.)

$M = (2 \cdot 4643.7 \text{ lb} \cdot 7.2 \text{ in.}) + (33.3/12 \text{ lb/in.} \cdot 336.75 \text{ in.} \cdot 7.2 \text{ in.})/2 + (2 \cdot 33.3/12 \text{ lb/in.} \cdot 7.2 \text{ in.}^2)/2$

$M = 70{,}161.5$ lb-in.

$\sigma = M \cdot c/I = (70{,}161.5 \text{ lb-in.}) \cdot (7.44 \text{ in.})/(396.7 \text{ in.}^4) = \mathbf{1{,}315.9 \text{ lb/in.}^2} = \sigma_{(\text{at G11 and G12})}$

(this equals 7.3% of the allowable 18,000 lb/in.^{2} used in 1930 for steel design)

Calculation of Original Design Stresses for Column C7:

Stress due to the axial load, σ_a:

W8x24: A = 7.06 in.^{2}, so $\sigma_a = P_{total}/A = (23{,}460 \text{ lb})/(7.06 \text{ in.}^2) = \mathbf{3{,}322.9 \text{ lb/in.}^2} = \sigma_a$

Stress due to bending, σ_b:

$\sigma_b = M \cdot c^2/I = (P_{(\text{from B8 - B7})}) \cdot c/I = (10{,}267.4 \text{ lb} - 7830 \text{ lb}) \cdot (3.965 \text{ in.})^2/82.5 \text{ in.}^4 =$

$\sigma_b = \mathbf{464.5 \text{ lb/in.}^2}$

Therefore the total stress on Column C7 is $(\sigma_a + \sigma_b) = \mathbf{3{,}787.4 \text{ lb/in.}^2}$

Calculation of Original Design Stresses for Column C8:

Stress due to the axial load, σ_a:

W8x24: A = 7.06 in.^{2}, so $\sigma_a = P_{total}/A = (17{,}191.4 \text{ lb})/(7.06 \text{ in.}^2) = \mathbf{2{,}435 \text{ lb/in.}^2} = \sigma_a$

Stress due to bending, σ_b:

$\sigma_b = M \cdot c/I = (204{,}554 \text{ lb-in.}) \cdot (3.965 \text{ in.})/82.5 \text{ in.}^4 = \mathbf{9{,}831 \text{ lb/in.}^2} = \sigma_b$

NOTE: The maximum bending moment will be due to the wind load exerted on the windows above column C8, so this moment needs to be determined as follows:

Calculation of Maximum Bending Moment on Column C8:

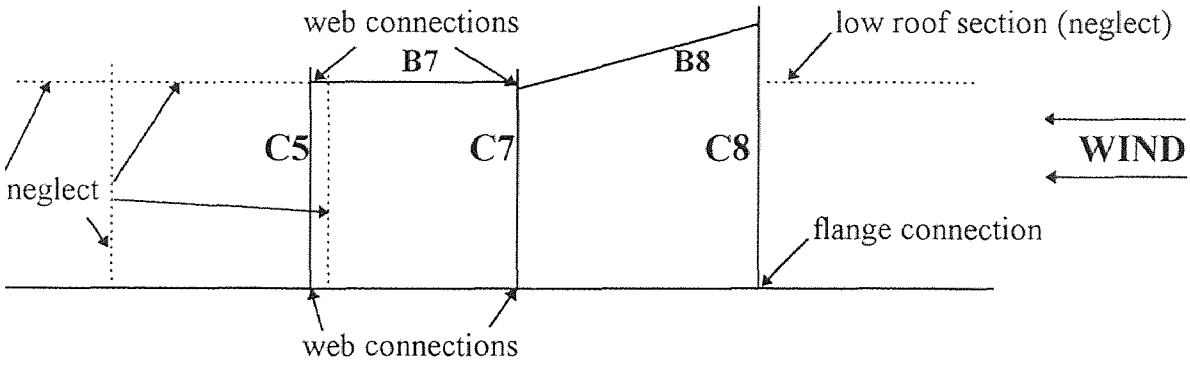

Figure C.1 Schematic of Section A-A for Determination of Maximum Moment on Column C8 Due to Wind Loading.

Since all pin (web) connections exist except for at the base of column C8, assume that C8 was designed to take the wind load as a cantilever for the moment determination.

ANALYSIS:

- Assume the wind load = 20lb/ft^2

- Height of the vertical face exposed to the wind ≈ 8.5 ft of the actual 10-ft exposure.

- Column C8 carries the wind load for a 20-ft horizontal section of the exposed wall.

Therefore, the total load due to the wind on column C8 is claculated as follows:

$$(8.5 \text{ ft})\cdot(20 \text{ ft})\cdot(20 \text{ lb/ft}) = 3400 \text{ lb}$$

From the assumptions stated, the wind load can be illustrated as shown at the right with two resultant forces, R_B and R_T.

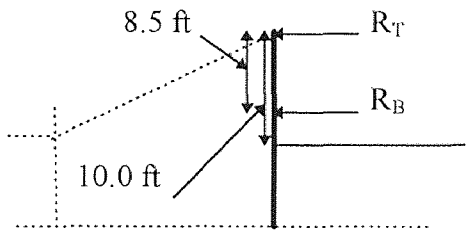

Figure C.2 Resultant Wind Forces.

Referring to Figure C.2, the following determination of the resultant forces are made by taking the moments about R_T and then R_B, respectively:

$$R_B = (3400 \text{ lb})\cdot(4.25 \text{ ft})/(10 \text{ ft}) = 1445 \text{ lb} = R_B$$

$$R_T = (3400 \text{ lb})\cdot(5.75 \text{ ft})/(10 \text{ ft}) = 1955 \text{ lb} = R_T$$

Based on the overall height of approximately 24.55 feet (from the flange connection at the slab to the uppermost point at R_T, the maximum moment can be determined.

$$M_{max} = (1955 \text{ lb})\cdot(24.55 \text{ ft}) + (1445 \text{ lb})\cdot(14.55 \text{ ft}) = 69{,}020 \text{ lb-ft} = 828{,}240 \text{ lb-in.}$$

so for the W8x24 section, $I = 82.5 \text{ in.}^4$ and $c = (7.93 \text{ in.}/2) = 3.965 \text{ in.}$, so the bending stress can be determined as follows:

$$\sigma_b = (828{,}240 \text{ lb-in.})\cdot(3.965 \text{ in.})/(82.5 \text{ in.}^4) = 39{,}806 \text{ lb/in.}^2$$

NOTE: $\sigma_b = 39{,}806 \text{ lb/in.}^2 > 2\cdot(\sigma_{allowable})$, therefore assume that the original assumption that column C5 which was partially embedded in a masonry wall has a fixed end at its bottom and reanalyze the bending stress for column C8.

TRIAL #2 - Fixed Ends at Columns C8 and C5:

Assume the distance y is taken as the vertical length from the slab level (at the slab y=0) to a point at which a resisting force in the horizontal direction, H, is acting against the wind. Therefore:

$$M(y) = (1955 \text{ lb})\cdot(24.55 \text{ ft} - y) + (1445 \text{ lb})\cdot(14.55 \text{ ft} - y) - (H)\cdot(22.90 \text{ ft} - y)$$

$$\theta(y) = (1/E\cdot I)\cdot\{[1955 \text{ lb}\cdot((24.55 \text{ ft})\cdot y - (y^2/2))] + [1445 \text{ lb}\cdot((14.55 \text{ ft})\cdot y - (y^2/2))] - [H\cdot((22.90 \text{ ft})\cdot y - (y^2/2))]\}$$

$$\delta(y) = (1/E\cdot I)\cdot\{[1955 \text{ lb}\cdot((24.55 \text{ ft})\cdot(y^2/2) - (y^3/6))] + [1445 \text{ lb}\cdot((14.55 \text{ ft})\cdot(y^2/2) - (y^3/6))] - [H\cdot((22.90 \text{ ft})\cdot(y^2/2 - (y^3/6))]\}$$

$E \cdot I \cdot \theta(14.55\ ft) = (1445\ lb) \cdot (14.55\ ft)^2/2 = 152{,}955\ lb\text{-}ft^2$ (due to R_B)

$E \cdot I \cdot \delta(14.55\ ft) = (1445\ lb) \cdot (14.55\ ft)^3/3 = 1{,}483{,}664\ lb\text{-}ft^3$ (due to R_B)

$E \cdot I \cdot \delta(22.90\ ft) = (1{,}483{,}664\ lb\text{-}ft^3) + (152{,}955\ lb\text{-}ft^2) \cdot (22.90\ ft - 14.55\ ft) =$

$= 2{,}760{,}838\ lb\text{-}ft^3$ (due to R_B)

$E \cdot I \cdot \delta(22.90\ ft) = (1955\ lb) \cdot [(24.55\ ft) \cdot (22.90\ ft)^2/2 - (22.90\ ft)^3/6] =$

$= 8{,}671{,}666\ lb\text{-}ft^3$ (due to R_T)

$E \cdot I \cdot \delta(22.90\ ft) = (-H) \cdot (22.90\ ft)^3/3 = (-4003 \cdot H)$ (due to H)

Totaling up these terms due to R_B, R_T, and H, the following expression is obtained:

$E \cdot I \cdot \delta(22.90\ ft) = (2{,}760{,}838\ lb\text{-}ft^3) + (8{,}671{,}666\ lb\text{-}ft^3) + (-4003 \cdot H) =$

$= (11{,}432{,}504\ lb\text{-}ft^3) - (4003 \cdot H)$ (TOTAL)

For Beam B8 (Refer to Figure A-3.3):

$\delta x'$ at left end = δx at top
(neglecting axial shortening)

Also, H' = H

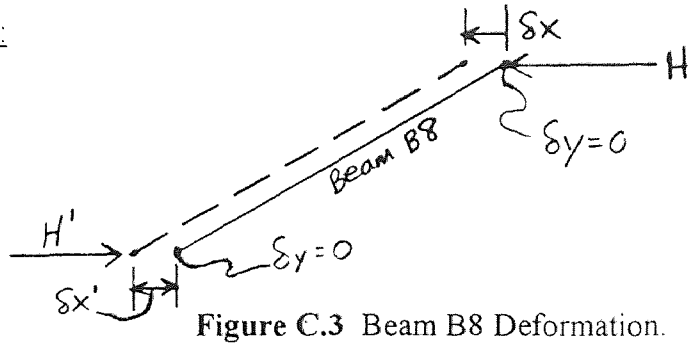

Figure C.3 Beam B8 Deformation.

For Column C7 (Refer to Figure C.4):

Moment Equilibrium: H'' = (14.24 ft)·H/(15.30 ft) Rigid Rotation

$(\delta x'')/(15.30\ ft) = (\delta x')/(14.24\ ft)$, so $\delta x'' =$

$= (15.30\ ft) \cdot (\delta x)/(14.24\ ft)$

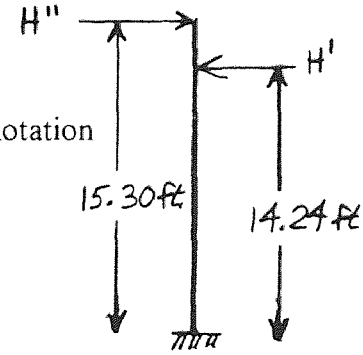

Figure C.4 Column C7.

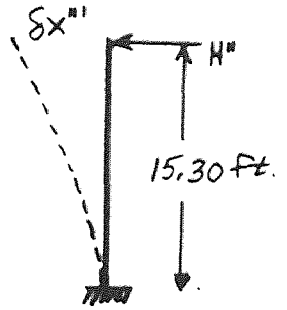

Figure C.5 Column C5.

For Column C5 (Refer to Figure C.5):

$(\delta x''') = (H'')\cdot(15.30\text{ ft})^3/(3\cdot E\cdot I) =$

$(\delta x''') = [(14.24\text{ ft})\cdot(H)/(15.30\text{ ft})]\cdot[(15.30\text{ ft})^3/(3\cdot E\cdot I)]$

but, $\delta x'''= \delta x''$, so

$(14.24\text{ ft})\cdot(H)\cdot(15.30\text{ ft})^2/3 = (15.30\text{ ft})/(14.24\text{ ft})\cdot[(11{,}432{,}504\text{ lb-ft}^3) - (4003\cdot H)]$

solving for H: $H = 2269.6$ lb

Substituting back into earlier equations:

$E\cdot I\cdot\delta_{total}(22.90\text{ ft}) = (2{,}347{,}295\text{ lb-ft}^3)$

$H'' = (14.24\text{ ft})\cdot H/(15.30\text{ ft}) = 2112.36$ lb

$E\cdot I\cdot\delta x'''= 2{,}521{,}859.7\text{ lb-ft}^3$

$M_{max} = (1955\text{ lb})\cdot(24.55\text{ ft}) + (1445\text{ lb})\cdot(14.55\text{ ft}) - (2269.6\text{ lb})\cdot(22.90\text{ ft}) = 17{,}046$ lb-ft

$M_{max} = (17{,}046\text{ lb-ft})\cdot(12\text{ in./ft}) = \mathbf{204{,}554\text{ lb-in.} = M_{max}}$

Use this moment to calculate σ_b:

$$\sigma_b = (M_{max})\cdot(c)/I = (204{,}554\text{ lb-in.})\cdot(3.965\text{ in.})/(82.5\text{ in.}^4) = 9{,}831\text{ lb/in.}^2$$

Therefore the total stress on Column C8 is $(\sigma_a + \sigma_b) = (2{,}435\text{ lb/in.}^2) + (9{,}831\text{ lb/in.}^2)$

$$\sigma_{total} = 12{,}266\text{ lb/in.}^2$$

APPENDIX D

DESIGN EXAMPLE
ESTIMATION OF GROUND SURFACE DEFORMATION DUE TO PNEUMATIC FRACTURE INJECTIONS

The following design example is intended to illustrate the application of the ground deformation model equation to prospective pneumatic fracturing sites. The example also provides the basis for the depth limits selected for the various design cases described in Chapter 6 (i.e., Cases 1, 2, and 3). The ground deformation model equation as developed in Chapter 4 is as follows:

$$w = P_x \cdot (1-\nu^2) \cdot (x^4 - 2 \cdot R^2 \cdot x^2 + R^4)/(16 \cdot E \cdot z^3) \qquad (D.1)$$

In applying the ground deformation model to a site undergoing pneumatic fracturing, it is necessary to establish which parameters are known, which parameters must be estimated, and finally those parameters which are unknown. The depth, z, will of course be a known quantity since it corresponds to the desired depth of fracturing at the site. The quantities of the modulus of elasticity, E, and Poisson's ratio, ν, are also site dependent. On occasion, these parameters may be determined by special geotechnical testing at the site using a pressuremeter or other device. In most cases, however, the values of E and ν will have to be determined by using one of two approaches. The first and most reliable method is to perform a pilot fracture injection test at the site in an "open" area located away from any existing structures or utilities. By carefully measuring the ground deformation, w, and fracture radius, R, with known injection pressures, it will then be

possible to back-calculate the values of E and ν using model Equation 4.13 for the particular geologic formation in question. Once these formation parameters are established, they can then be used to predict ground deformations underneath the structure using the same model equation.

Although a field pilot injection test is definitely the best way to predict ground surface movements due to pneumatic fracturing, such tests are not always possible within budget and time constraints of a project. In these instances, and also when it is desired to just develop a preliminary design calculation, the values of E and ν can be estimated using empirical correlations with the geologic materials present at the site. Values for E and ν are available from a variety of published sources (e.g. AASHTO, 1996 and U.S. Navy, 1982). It is noted that reported values for ν do not vary significantly for geologic materials. Furthermore, the selected value of ν has a relatively minor mathematical influence on the final magnitude of the ground deformation. Therefore, it is recommended that 0.30 and 0.25 be used as nominal values of ν for soil and rock, respectively, for design purposes.

The published range of modulus of elasticity values is considerably wider. In addition, the model equation is more mathematically sensitive to this parameter. A listing of recommended E values for use in the surface deformation equation are presented in Table D.1. These are based on a regression of actual data from pneumatic fracture injections, as well as a consideration of the published data.

The driving pressure (fracture maintenance pressure) for the fracture, P_x, may be estimated using the following expressions modified from King (1993):

$$P_x = 1.5 \cdot z + 5 \quad \text{(for soil)} \qquad \text{(D.2)}$$

$$P_x = 2.5 \cdot z + 15 \quad \text{(for rock)} \qquad \text{(D.3)}$$

where z is the depth of the fracture in feet, and P_x is expressed in lbs/in.^{2}.

Table D.1 Recommended Modulus of Elasticity Values for Use in Pneumatic Fracturing Projects (Tentative).

Geologic Material	E (lbs/in.^{2}) for the following Depth Ranges		
	4 ft to 10 ft	10 ft to 20 ft	20 ft to 40 ft
medium silty clay, clay	1000	2000	2500
stiff silty clay, clay	3500	4500	6000
medium to dense sand	5000	5000	8000
dense decomposed sedimentary rock (residual soil)	5000	10,000	20,000
moderately fractured mudstone	20,000	35,000	60,000

There are three remaining variables: x, R, and *w*. The variable x is merely a range variable which is varied over the radius to develop the curve. This then leaves the variables R, the maximum fracture radius, and *w*, the surface deformation. In order to use the model, it is necessary to assume one and then compute the other. In most design applications where an estimate of ground deformation is desired, it is recommended that R be assumed and *w* be calculated. Table D.2 presents suggested values of maximum fracture radius based on experience at more than 20 field sites.

Table D.2 Suggested Values of Maximum Radius for Pneumatic Fracturing Projects (Tentative).

Geologic Material	Radius (ft) for the following Depth Ranges		
	4 ft to 10 ft	10 ft to 20 ft	20 ft to 40 ft
medium clay or silt	12	18	---
stiff clay or silt	16	22	32
medium fine sands	5	8	10
sedimentary rock	20	30	40

Design Example:

Site Conditions:

Medium to stiff silty clay: Use $\nu = 0.30$ $E = 3200$ lbs/in.^{2} (from Table D.1)

Fracture Depth: Use $z = 15$ ft (from contaminant location)

From Table D.2: Use $R = 20$ ft

Estimate the maintenance pressure: $p_d = (1.5 \cdot z) + 5$ $p_d = 27.5$ lbs/in.^{2}

$x = -20, -19..20$

$P_x(x) = p_d \cdot 144 \text{ in.}^2/\text{ft}^2 \cdot (1 - |x|/R)$

Computing ground deformation as a function of x:

$$w(x) = [(P_x(x)) \cdot (1-\nu^2) \cdot (x^4 - 2 \cdot R^2 \cdot x^2 + R^4)/(16 \cdot E \cdot (144\text{in.}^2/\text{ft}^2) \cdot z^3)] \cdot (12 \text{ in./ft})$$

Now plotting the results:

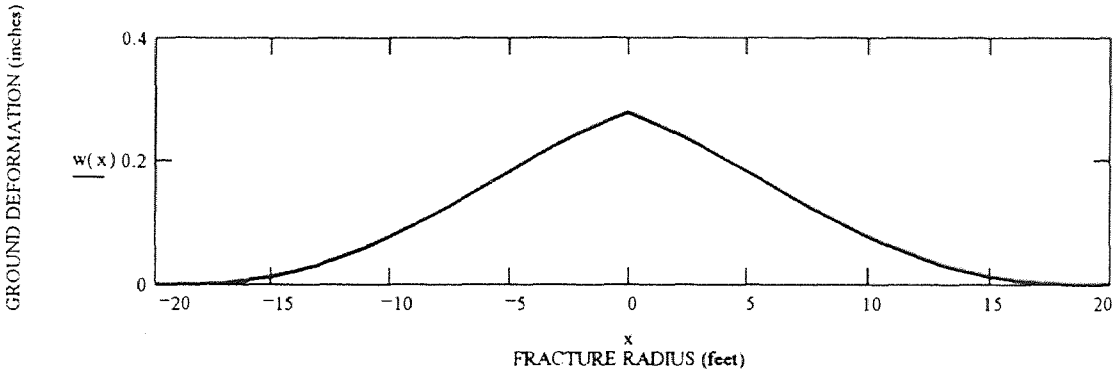

Figure D.1 Design Example Surface Deformation Plot.

Also, maximum deformation at the center can be determined directly using Equation 4.14:

Setting $x = 0$:

$$w_{max} = [(P_x(x)) \cdot (1-\nu^2) \cdot R^4/(16 \cdot E \cdot (144\text{in.}^2/\text{ft}^2) \cdot z^3)] \cdot (12 \text{ in./ft})$$

$$w_{max}(x) = 0.278 \text{ inches}$$

REFERENCES

AASHTO, 1996. *Standard Specifications for Highway Bridges,* Sixteenth Edition, Section 4, American Association of State Highway and Transportation Officials, Washington, DC.

American Concrete Pipe Association, 1980. *Concrete Pipe Handbook,* American Concrete Pipe Association, Vienna, VA.

American Institute of Steel Construction, 1984. *Manual of Steel Construction*, Eighth Edition, Section 2. American Institute of Steel Construction, Chicago, IL, p. 119.

American Society of Civil Engineers and the Water Pollution Control Federation, 1976. *Design and Construction of Sanitary and Storm Sewers, ASCE-Manuals and Reports on Engineering Practice-No. 37 (WPCF Manual of Practice No. 9),* ASCE Printing, New York, NY, p. 212.

Applied Geomechanics, 1991. "User's Manual: 700-Series Platform and Surface Mount Tiltmeters, Model No. 701-2," Applied Geomechanics Inc., Santa Cruz, CA.

Bjerrum, L., 1963. Allowable Settlement of Structures, *Proceedings of the 3rd European Conference on Soil Mechanics and Foundation Engineering*, Wiesbaden, 2, Brighton, England, pp. 135-137.

Burland, J.B. and Wroth, C.P. (1974), Settlement of Buildings and Associated Damage, *Proceedings of the Conference on Settlement of Structures - Session V*, Cambridge, England, pp. 611-654.

Coduto, D.P., 1994. *Foundation Design - Principles and Practices.* Prentice-Hall, Inc., Englewood Cliffs, NJ.

D'Appolonia, D.J., 1971. Effects of Foundation Construction on Nearby Structures, *Proceedings of the 4th Panamerican Conference on Soil Mechanics*, Puerto Rico, Vol. 1, pp. 189-236.

Davis, W.M., 1925. "Laccoliths and Sills," Washington Academic Science Journal, Vol. 15, Issue No. 18, pp. 414-415.

Ding, Y., 1995. "A Theoretical Analysis of Volatile Contaminant Removal by the Pneumatic Fracturing Process," Ph.D. Dissertation, Department of Civil and Environmental Engineering, New Jersey Institute of Technology, Newark, NJ.

Dunnicliff, J., 1988. *Geotechnical Instrumentation for Monitoring Field Performance,* Wiley, New York, NY.

REFERENCES
(Continued)

Feld, J., 1965. Tolerance of Structures to Settlement, *ASCE Journal of the Soil Mechanics and Foundation Division*, Vol. 91, SM3, May 1965, pp. 63-77.

Fernandez, H.J., In progress. "A Coupled Ultrasonic-Pneumatic Process for *In Situ* Remediation of Contaminated Soils," M.S. Thesis, Department of Chemical Engineering, Chemistry, and Environmental Science, New Jersey Institute of Technology, Newark, NJ.

Fitzgerald, C.D., 1993. "Integration of Pneumatic Fracturing to Enhance *In Situ* Bioremediation," M.S. Thesis, Department of Civil and Environmental Engineering, New Jersey Institute of Technology, Newark, NJ.

Gilbert, G.K., 1877. *Report on the Geology of the Henry Mountains*, United States Geographical and Geological Survey of the Rocky Mountains Region, United States Government Printing Office, Washington, DC.

Grant, R., Christian, J., and Vanmarcke, E., 1974. Differential Settlement of Buildings, *ASCE Journal of the Geotechnical Engineering Division*, Vol. 100, GT9, pp. 973-991.

Hall, H.A., 1995. "Investigation Into Fracture Behavior and Longevity of Pneumatically Fractured Fine-Grained Formations," M.S. Thesis, Department of Chemical Engineering, Chemistry, and Environmental Science, New Jersey Institute of Technology, Newark, NJ.

Hall, H.A., In progress. "Investigation Into Fracture Behavior and Longevity of Pneumatically Fractured Fine-Grained Formations," Ph.D. Dissertation, Department of Chemical Engineering, Chemistry, and Environmental Science, New Jersey Institute of Technology, Newark, NJ.

Holtz, R.D., 1991. Stress Distribution and Settlement of Shallow Foundations, *Foundation Engineering Handbook*, H.Y. Fang, editor., Chapter 5, Van Nostrand Reinhold, New York, NY, pp.166-222.

Hunt, C.B., 1953. "Geology and Geography of the Henry Mountains Region," Utah. United States Geological Survey, Professional Paper No.228.

Imholte, T.J., 1995. "Potential Effects of Pneumatic Fracturing on Existing Structures and Utilities," Masters Project Report, Department of Civil and Environmental Engineering, New Jersey Institute of Technology, Newark, NJ.

REFERENCES
(Continued)

Johnson, A.M., 1970. *Physical Processes in Geology*. Freeman-Cooper, San Francisco, CA.

King, T.C., 1993. "Mechanism of Pneumatic Fracturing," M.S. Thesis, Department of Civil and Environmental Engineering, New Jersey Institute of Technology, Newark, NJ.

Love, A.E.H. , 1944. *A Treatsie on the Mathematical Theory of Elasticity*, 4th edition. Dover Publications, New York, NY.

McGonigal, S.T., 1995. "Integration of Pneumatic Fracturing and *In Situ* Vitrification," M.S. Thesis, Department of Civil and Environmental Engineering, New Jersey Institute of Technology, Newark, NJ.

Meyerhof, G.G. and Fellenius, B.H. (editors), 1985. *Canadian Foundation Engineering Manual*, 2nd ed., Canadian Geotechnical Society.

Myslivec, A. and Kysela, E., 1978. *Bearing Capacity of Building Foundations*, Elsevier, N.Y., p.154.

Nautiyal, D., 1994. "Fluid Flow Modeling for Pneumatically Fractured Formations," M.S. Thesis, Department of Civil and Environmental Engineering, New Jersey Institute of Technology, Newark, NJ.

Newey, C. and Weaver, G., 1990. *Materials Principle and Practice*, Materials Department, Open University, Milton Keynes, England. Publisher - Butterworths, Boston, MA.

Newmark, N.M., 1942. "Influence Charts for Computation of Stresses in Elastic Foundations," Engineering Experiment Station Bulletin 338, University of Illinois, Urbana.

Ng, N., 1991. "Enhancement of Air Flow and Contaminant Removal in Fractured Soil," M.S. Project, Department of Civil and Environmental Engineering, New Jersey Institute of Technology, Newark, NJ.

New Jersey Institute of Technology (NJIT) and Accutech Remedial Systems (ARS), 1994. "Integration of Pneumatic Fracturing with *In Situ* Vitrification-DOE Hanford Facility," for Battelle Pacific Northwest Laboratories, Richland, WA.

REFERENCES
(Continued)

Papanicolaou, P., 1989. "Laboratory Model Studies of Pneumatic Fracturing of Soils to Remove Volatile Organic Compounds," M.S. Thesis, Department of Civil and Environmental Engineering, New Jersey Institute of Technology, Newark, NJ.

Perloff, W.H., 1975. Pressure Distribution and Settlement, *Foundation Engineering Handbook*, H.F. Winterkorn & H.Y. Fang, eds., Chapter 4, Van Nostrand Reinhold, New York, N.Y., pp.148-196.

Perloff, W.H. and Baron, W., 1976. *Soil Mechanics, Principles and Applications*, Ronald Press, New York, NY.

Pollard, D.D., 1968. "*Deformation of Host Rocks During Sill and Laccolith Formation*," Ph. D. Dissertation, Department of Geology, Stanford University, CA.

Pollard, D.D. and Johnson, A.M., 1973. "Mechanics of Growth of Some Laccolithic Intrusions in the Henry Mountains, Utah, II - Bending and Failure of Overburden Layers and Sill Formation," Tectonophysics, Vol. 18, pp. 311-354.

Polshin, D.E. and Tokar, R.A., 1957. Maximum Allowable Nonuniform Settlement of Structures, *Proceedings of the 4th International Conference on Soil Mechanics and Foundation Engineering*, London, **I**, pp.402-6

Price, N.J., 1975. "Rates of Deformation," Journal of the Geological Society of London, Volume 131, pp. 553-575.

Puppala, S., In progress. "Fracture Propagation and Particulate Transport in Pneumatically Fractured Formations," Ph.D. Dissertation, Department of Civil and Environmental Engineering, New Jersey Institute of Technology, Newark, NJ.

Rahman, A.M., 1994. "Integration of Surfactants and Time Release Nutrients with the Pneumatic Fracturing Process," M.S. Thesis, Department of Civil and Environmental Engineering, New Jersey Institute of Technology, Newark, NJ.

Schmertmann, J.H., Hartman, J.P., and Brown, P.R., 1978. "Improved Strain Influence Factor Diagram," ASCE Journal of Geotechnical Engineering Division, Vol. 104, GT8, pp. 1131-1135.

Schuring, J.R., 1994. "Pneumatic Fracturing to Remove Soil Contaminants," NJIT Research - Environmental Engineering and Science, Volume 2, Spring 1994.

REFERENCES
(Continued)

Schuring, J.R. and P. Chan., 1992. "Removal of Contaminants from the Vadose Zone by Pneumatic Fracturing," U.S. Geological Survey, Department of the Interior, U.S.G.S. Award 14-08-0001-G1739.

Schuring, J., Jurka, V., and Chan, P., 1991. "Pneumatic Fracturing of a Clay Formation to Enhance Removal of VOCs," *Proceedings of the Fourteenth Annual Madison Waste Conference*, University of Wisconsin, Madison, WI.

Schuring, J.R., Raghu, D., and Dauenheimer, E.G., 1988. "Foundation Problems and Their Effect on the Serviceability of Buildings," *Proceedings of the Symposium/ Workshop on Serviceability of Buildings (Movements, Deformations, Vibrations)*, Volume I, pp. 360-377. University of Ottawa, Ottawa, Ontario, Canada.

Schuring, J.R., Canino, M.C., Boland, T.M., and Nelson, I., 1996. "Final Report, Site-45D, Investigation of the Effects of Pneumatic Fracturing on Structures and Utilities," prepared for the Hazardous Substance Management Research Center, New Jersey Institute of Technology, Newark, NJ. A National Science Foundation Industry/University Cooperative Research Center.

Széchy, K., 1973. *The Art of Tunnelling,* Second Edition, Tankonyvkiado (publisher), Budapest, Hungary.

Shah, N.P., 1991. " Study of Pneumatic Fracturing to Enhance Vapor Extraction of the Vadose Zone," M.S. Thesis, Department of Civil and Environmental Engineering, New Jersey Institute of Technology, Newark, NJ.

Sielski, B.M., In progress. "Comprehensive Computer Model for Pneumatic Fracturing," Ph.D. Dissertation, Department of Civil and Environmental Engineering, New Jersey Institute of Technology, Newark, NJ.

Skempton, A.W. and MacDonald, D.H., 1956. Allowable Settlement of Buildings, *Proceedings of the Institution of Civil Engineers*, **5**, Part III, pp. 727-768.

Sowers, G.F., 1962. *Shallow Foundations, Foundation Engineering,* ed. G.A. Leonards, McGraw-Hill Book Co., New York, NY, pp. 525-632.

The American Geological Institute, 1984. *Dictionary of Geological Terms*, Third Edition. Bates, R.L. and Jackson, J.A., Editors. Published by Doubleday, New York, NY, p. 284.

Timoshenko, S., 1953. *History of the Strength of Materials,* Van Nostrand, Princeton, NJ.

REFERENCES
(Continued)

Timoshenko, S. and Goodier, J.N., 1951. *Theory of Elasticity,* McGraw-Hill Book Company, New York, NY.

Timoshenko, S. and Woinowsky-Krieger, S., 1959. *Theory of Plates and Shells,* McGraw-Hill Book Company, New York, NY.

Tschebotarioff, G.P., 1973. Foundations, Retaining and Earth Structures, 2nd Edition, McGraw-Hill, New York, p. 159.

Turcotte, D.L. and Schubert, G. 1982. *Geodynamics - Applications of Continuum Physics to Geological Problems.* John Wiley & Sons, New York, NY, Chapter 3.

United States Army Corps of Engineers, 1994. *Technical Engineering and Design Guide No. 9,* Settlement Analysis, ASCE Press, New York, N.Y.

United States Navy, 1982. *Soil Mechanics, Design Manual 7.1,* Department of the Navy, Navy Facilities Engineering Command (NAVFAC), Arlington, VA.

United States Patent No. 5,032,042, 1991. *Method and Apparatus for Eliminating Non-Naturally Occurring Subsurface Liquid Toxic Contaminants from the Soil.*

Wahls, H.E., 1981. "Tolerable Settlement of Buildings," *Journal of Geotechnical Engineering Division,* ASCE, 107, No. GT11, pp. 1489-1504.